STRUCTURAL AND BIOPHYSICAL CHARACTERIZATION OF THE MYOCILIN OLFACTOMEDIN DOMAIN

A Dissertation
Presented to
The Academic Faculty

by

Rebecca K. Donegan

In Partial Fulfillment
of the Requirements for the Degree
Doctor of Philosophy in the
School of Chemistry and Biochemistry at Georgia Institute of Technology

Georgia Institute of Technology
August 2015

STRUCTURAL AND BIOPHYSICAL CHARACTERIZATION OF THE MYOCILIN OLFACTOMEDIN DOMAIN

Approved by:

Dr. Raquel L. Lieberman, Ph.D., Advisor
School of Chemistry and Biochemistry
Georgia Institute of Technology

Dr. Adegboyega Oyelere, Ph.D.
School of Chemistry and Biochemistry
Georgia Institute of Technology

Dr. Ingeborg Schmidt-Krey, Ph.D.
School of Biology and
School of Chemistry and Biochemistry
Georgia Institute of Technology

Dr. Loren Williams, Ph.D.
School of Chemistry and Biochemistry
Georgia Institute of Technology

Dr. Cheng Zhu, Ph.D.
School of Biomedical Engineering
Georgia Institute of Technology

Date Approved: April 30, 2015

ACKNOWLEDGEMENTS

First, I would like to thank my husband Brad for always supporting and encouraging me. I also wish to thank my mom and dad for encouraging me to work towards this goal since I first started college. I want to thank my siblings, grandparents, and in-laws for their constant encouragement. All of you have offered help and reassurance along the way, and I would not have reached this goal without you. I would also like to thank my lab mates, current and former, for all of their advice, instruction and help throughout the years. I would especially like to thank Dana Freeman for all of her help during her time as an undergraduate researcher. Finally, I would like to thank Dr. Raquel Lieberman, my advisor, for the opportunity to work in her lab and pursue this research. Her mentorship and guidance has helped shape me as a scientist and researcher.

TABLE OF CONTENTS

Page

LIST OF TABLES

Page

LIST OF FIGURES

Page

LIST OF SYMBOLS AND ABBREVIATIONS

2D	Two Dimensional
AD	Alzheimer's Disease
AFM	Atomic Force Microscopy
AH	Aqueous Humor
BME	β-mercaptoethanol
CAG	Closed Angle Glaucoma
CD	Circular Dichroism
DSC	Differential Scanning Calorimetry
DSF	Differential Scanning Fluorescence
ECM	Extracellular Matrix
EDTA	Ethylenediaminetetraacetic Acid
EGTA	Ethylene Glycol Tetraacetic Acid
ER	Endoplasmic Reticulum
ERAD	Endoplasmic Reticulum Associated Degradation
ERK1/2	Extracellular Signal Related Kinases 1/2
GM/CA-CAT	National Institute of General Medical Sciences and National Cancer Institute Collaborative Access Team
GRP	Glucose Regulated Protein
ICP-OES	Inductively Coupled Plasma Optical Emission Spectroscopy
Iodo-Phe	Iodophenylalanine
IOP	Intraocular Pressure
IPTG	Isopropyl β-D-Thiogalactopyranoside
K_d	Dissociation Constant
MAD	Multi-wavelength Anomalous Dispersion

MBP	Maltose Binding Protein
MBP-OLF	Maltose Binding Protein - Myocilin Olfactomedin Domain Fusion Protein
MIR	Multiple Isomorphous Replacement
mM	millimolar
myoc-OLF	Myocilin Olfactomedin Domain
NTG	Normal Tension Glaucoma
OAG	Open Angle Glaucoma
OLF	Olfactomedin domain
PCAG	Primary Closed Angle Glaucoma
PCG	Primary Congenital Glaucoma
PEG	Polyethylene Glycol
PEX	Pseudoexfoliation Syndrome
POAG	Primary Open Angle Glaucoma
RGC	Retinal Ganglion Cell
SAD	Single Wavelength Anomalous Diffraction
SC	Schlemm's Canal
SeMet	Seleomethionine
SER-CAT	Southeast Regional Collaborative Access Team
SNP	Single Nucleotide Polymorphism
SOAG	Secondary Open Angle Glaucoma
SS	Secondary Structure
ThT	Thioflavin T
TM	Trabecular Meshwork
T_m	Melting Temperature
WT	Wild Type

SUMMARY

Primary open angle glaucoma (POAG) is the most common form of the prevalent neurodegenerative ocular disorder, and mutations in the protein myocilin are closely linked to inherited forms of POAG. Instead of secretion from trabecular meshwork (TM) cells to the extracellular matrix (ECM) of the TM that regulates fluid flow in the eye, mutant myocilin builds up in the endoplasmic reticulum of TM cells. This leads to TM cell death, the misregulation of fluid flow, ocular hypertension, and the early onset of the retina degeneration associated with glaucoma. Nearly all of the documented disease-causing mutations occur in the C-terminal olfactomedin (OLF) domain of myocilin (myoc-OLF). While many OLF domain-containing proteins are implicated in disease, the biological function(s) of OLF domains are elusive, and, until this work, molecular details of OLF domains were also largely unknown.

Previous data from the lab had indicated that myoc-OLF, like other ECM proteins, is stabilized by the addition of Ca^{2+}; however, the myoc-OLF sequence had no predicted Ca^{2+} binding sites. The thermal stabilities of variants representing sites of potential Ca^{2+} ligands were monitored via differential scanning fluorimetry (DSF), and selected variants were further characterized by CD, metal analysis, and chelator binding. A total of 24 variants of myoc-OLF were analyzed, 18 of which were glaucoma-causing mutations, but just three potential Ca^{2+} ligands emerged. The Ca^{2+} binding residue, Asp 380, was identified. The disease-associated myoc-OLF D380A variant is able to fold, with a melting temperature somewhat less than that of wild-type, but was not thermally stabilized by the addition of Ca^{2+}. Metal analysis of wild-type myoc-OLF revealed that Ca^{2+} is present at a nearly 1:1 ratio compared to 0.1:1 for the D380A variant, and fluorescence by the Ca^{2+} sensor Quin-2 showed release of Ca^{2+} from wild-type myoc-OLF only upon chemical

unfolding. Taken together, these experiments pointed to a novel high affinity Ca^{2+} binding site largely buried within myoc-OLF, which was verified by the myoc-OLF crystal structure.

The myoc-OLF domain was previously shown in the lab to grow amyloid-like fibrils. Analysis of the myoc-OLF sequence with amyloid prediction programs revealed three potential amyloidogenic regions. Two of these peptide stretches grew amyloid-like fibrils with similar morphologies to those grown by full-length myoc-OLF. The myoc-OLF crystal structure revealed that the two peptides that grew fibrils occupied the two inner beta strands of opposing blades, whereas the peptide that did not occupied a different region of the blade.

The structure of myoc-OLF was solved by anomalous phasing via selenomethionine-incorporated single wavelength anomalous diffraction (SeMet-SAD). SeMet substituted myoc-OLF(E396D), a single nucleotide polymorphism (SNP) variant that grew superior quality crystals to those of wild-type myoc-OLF, was used for initial phasing. Structures of myoc-OLF(E396D) without SeMet and wild-type myoc-OLF, whose data set was collected by former PhD student Susan Orwig, were solved via molecular replacement. The highest resolution structure, 1.9 Å, was obtained from crystals of myoc-OLF(E396D). The topology is a new 5-bladed β-propeller covalently tethered by a disulfide bond, as predicted biochemically, between two N- and C-terminal cysteine residues present in the myoc-OLF domain. The Ca^{2+} binding site, involves residues residing on three interior beta stands in three separate blades and may stabilize myoc-OLF. A previously unknown binding site adjacent to the Ca^{2+} site is modelled as a Na^{+} ion. Our three solved myoc-OLF domain structures also reveal surface loop conformations that have different surface features and accessibility to the Ca^{2+} site.

While propellers are known for having the ability to interact with multiple proteins, and many are enzymes, analysis of the structure does not point to obvious function for the

OLF domain. However structures revealed potential binding regions uncovered by both computational solvent mapping and small molecule binding. Of particular interest is an interior binding site predicted in all three myoc-OLF structures, and occupied by a glycerol molecule in two of the structures. This site has been shown computationally to be able to accommodate small molecules similar to glycerol that are in the aqueous humor such as lactate and glutamate, which thermally stabilize myoc-OLF similarly to glycerol. On the surface, the aforementioned observed loop conformational changes are due to changes in the position of a Trp/Tyr pair, revealing different binding regions, and have different small molecules bound in two of the structures. This result shows the potential for the movement of the Trp/Tyr pair to select for ligand binding or protein-protein interactions. The conservation of residues of 1000 OLF domains mapped onto the myoc-OLF structure, reveals a stark difference in the surfaces of OLF proteins, despite a highly conserved interior cavity. This reveals the possibility that OLF domains have a conserved function particularly in the Ca^{2+}-binding region, such as Ca^{2+} sensing, but varying interacting partners.

Finally, the structure of myoc-OLF has also been utilized to provide insight on the relation between disease mutations and misfolding of myoc-OLF. 90% of disease causing mutations found in the human population within myoc-OLF fall into three misfolding “hot-spots”: the hydrophobic region between blades, the Ca^{2+} environ, and the residues found within or stabilizing a long loop that potentially caps solvent access to the interior hydrophilic cavity. This long loop harbors several disease causing mutations and a highly conserved, previously unknown, cation-π interaction. Mutations predicted to interfere with this cation-π interaction have been shown to be very destabilizing. This new knowledge will aid in the assignment of new mutations as disease causing or neutral.

CHAPTER 1

INTRODUCTION

1.1 Glaucoma

Glaucoma is a group of neurodegenerative diseases of the optic nerve, with varying etiologies, that is a leading cause of irreversible blindness[1, 2] affecting more than 60 million people worldwide.[3] Vision loss is attributable to the death of retinal ganglion cells (RGCs), which carry visual signals from the eye to the brain. Damage to the nerve fiber layer surrounding the RGCs leads to nerve cupping and eventual vision loss due to RGC death.[4] Cupping differentiates glaucoma from other optic neuropathies involving RGC death.[5] Since glaucoma is often asymptomatic before vision loss occurs, individuals with risk factors for glaucoma can be monitored for optic nerve cupping to diagnose glaucoma before the death of RGCs and subsequent loss of visual field.[1] In the past, elevated intraocular pressure (IOP) was included in the definition of glaucoma, however the optic neuropathy associated with glaucoma can exist in individuals considered to have normal IOP, less than 21 mm Hg, termed normal tension glaucoma (NTG).[2] For treatment of both NTG and high IOP glaucoma patients, lowering IOP was shown to be beneficial for slowing visual field loss.[6] This approach has proven useful at reducing the loss of visual field over time, but IOP reduction alone does not completely halt disease progression.[7]

1.1.1 Types of Glaucoma

There are many forms of glaucoma, and the heterogeneity of the disease increases the difficulty in developing treatments. Glaucoma can be divided based on the iridocorneal angle of the eye into closed-angle (CAG) and open-angle glaucoma (OAG),[8]

with OAG being both more common, accounting for approximately 75% of glaucoma cases in the population.[3] OAG and CAG can both be further divided into primary and secondary forms. Primary closed-angle glaucoma (PCAG) has obstructed outflow of aqueous humor (AH), and often corresponding increased IOP, due to pupillary block, where the iris is in contact with the trabecular meshwork (TM). While secondary closed-angle glaucoma (SCAG) has iridocorneal angle closure and obstructed AH outflow due to a secondary cause such as inflammation.[8] Primary open-angle glaucoma (POAG) is the most common form of glaucoma, and refers to disease that presents itself without being attributable to other disease, injury or closed iridocorneal angle.[8] Secondary open-angle glaucoma (SOAG) refers to glaucoma that is due to other causes such as Pseudoexfoliation (PEX) syndrome,[9] or prolonged use of steroids, which can lead to SOAG in about 30% of the population, a form of the disease termed steroid-induced glaucoma.[10] Finally glaucoma can be further divided based on age of onset into congenital, juvenile (for those with onset at less than 35 years of age) and adult onset.

1.1.2 Genetics of Glaucoma

Similar to the varying etiologies and pathogenesis of glaucoma, the genetics of glaucoma are not straightforward. The first, and to date most evidenced, gene associated with glaucoma is MYOC, and numerous mutations have been linked with juvenile OAG.[11, 12] Other genes associated with OAG include OPTN and WDR36, which are seen in both inherited and sporadic forms of adult onset POAG.[12, 13] OPTN is more specifically related to NTG with the E50K mutation.[14, 15] Inherited genetic susceptibility for glaucoma has been found in studies on POAG patient families, with relatives of POAG patients 20% more likely to develop glaucoma in their lifetime than controls.[16] MYOC, OPTN and WDR36 together, however, only account for about 10% of glaucoma.[11, 12] Common variant

rs4236601 near Cav1/Cav2 is associated with POAG.[17, 18] Over 20 other genes have been associated with glaucoma susceptibility including CYP1B1, which is associated with PCG (primary congenital glaucoma) and POAG,[13] TP53 (tumor protein 53), APOE (apolipoprotein), and IL1 α and β (Interleukin-1 α and β), validating the concern that glaucoma is due to a complicated mix of genetics and environ.[12]

1.1.3 Glaucoma and Other Diseases

Glaucoma susceptibility has also been linked to patients with Alzheimer's disease (AD) and diabetes. While studies have shown correlation between the diseases, there have been conflicting studies showing no increased risk for glaucoma in patients with either AD or diabetes.[19, 20] Currently since no correlation with AD can be ruled out, and since glaucoma has been shown to have similar cellular processes to AD,[21] AD may be viewed as a risk factor for glaucoma and vice versa.[22] While there are conflicting studies with diabetes as well, it is better accepted as a risk factor for glaucoma as diabetes patients have been repeatedly shown to be more likely to have higher IOP and develop glaucoma than non-diabetes patients.[20]

1.1.4 Aqueous Humor Production, Outflow, Intraocular Pressure and Glaucoma

AH is produced in the nonpigmented epithelial cells of the ciliary body in the eye, flows from the posterior to anterior segment of the eye, and out through either the conventional or uveoscleral pathway (Figure 1.1). AH supplies the nonvascular eye tissues, such as the lens and cornea, and maintains the shape of the eye necessary for vision. The conventional pathway involves outflow through the TM to the Schlemm's canal (SC) and episcleral vein. In the uveoscleral pathway, AH passes through the ciliary body and iris root, bypassing the TM and SC.[23] Proper IOP is dependent on the regulation of

inflow and outflow of AH. Elevated IOP increases outflow through the conventional pathway, but has little effect on outflow through the uveoscleral pathway.[24] Aging and disease affect AH outflow facility.[25] In the healthy eye, decreases in both inflow and uveoscleral outflow occur in older populations, but the conventional outflow and IOP is maintained.[26] Glaucoma risk increases with age and elevated IOP,[27] and outflow facility is impaired in disease, though the exact cause is unknown.[25]

Tissues within the eye change during glaucoma disease progression. Some of these changes, such as those of the lamina cribrosa and prelaminar tissues that are involved in optic nerve head cupping, can be monitored to track glaucoma progression.[28] Changes in other tissues such as the TM and SC are very similar to changes that occur within the eye due to aging, and may offer insight into the source of glaucoma pathogenesis, as the TM and SC are involved in regulating outflow of AH in the conventional pathway (Figure 1.1). Glaucomatous eyes have been shown to have increased extracellular matrix (ECM) stiffness in the TM,[29] increased cell stiffness of the SC and decreased SC epithelial cell pore formation,[30] similar to aging eyes.[31]

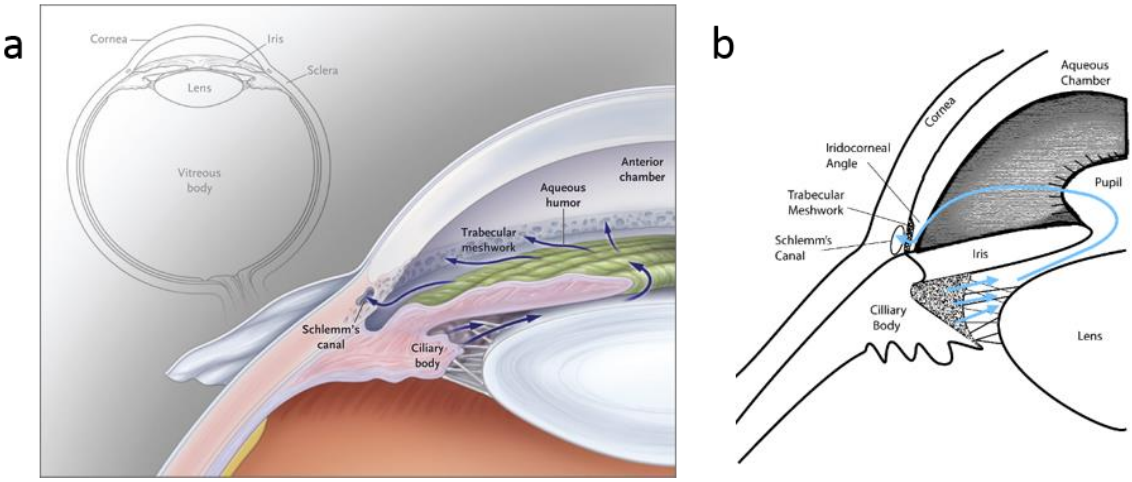

Figure 1.1 Aqueous humor pathway. Flow of AH within the anterior chamber of the eye. a. Inset shows overview of the eye. Reproduced with permission from[7]. Copyright Massachusetts Medical Society. b. Cross section of the anterior chamber of the eye with AH flow highlighted.

1.2 Myocilin Linked with Glaucoma

Myocilin, originally Trabecular Meshwork Inducible Glucocorticoid Response or TIGR, was initially linked with steroid induced glaucoma. Prolonged use of steroids was shown to increase IOP and cause secondary glaucoma in some patients. The discovery of increased myocilin or TIGR expression upon exposure of human TM cells to steroids, such as dexamethasone, led to the association of myocilin with steroid glaucoma.[32, 33]

The link between myocilin up-regulation by dexamethasone exposure and IOP increase is not understood, although myocilin expression is not directly regulated by dexamethasone as the increase is not immediate upon exposure to corticosteroids.[34] The

genetic link between myocilin and glaucoma was initially found in a large genetics study of a family with juvenile OAG, where the defect was assigned to a gene designated GLC1A mapped to chromosome 1q21-1q23.[35] Further familial studies verified the link between the GLC1A gene and inherited OAG,[36] and eventually the gene product was identified and named myocilin for its myosin-like domain and its localization to the ciliary rootlet and cilium of photoreceptor cells.[37]

1.2.1 Steroid Induced Glaucoma

Steroid use has been shown to cause elevated IOP in a subset of the population, and steroid treated mice and cells are used as a model system of glaucoma progression due to the changes in the TM with long exposure to steroids.[38] There are several genes upregulated in the TM upon extended exposure to steroids, but the overexpression of myocilin is implicated in the rise of IOP. While the exact link between myocilin expression levels and decreased outflow through the TM is not understood, myocilin has been shown to be overexpressed in TM cells exposed to glucocorticoids,[39] the delay in myocilin overexpression is similar to the delay in IOP increase upon exposure to steroids, and myocilin expression levels correlate with doses of glucocorticoids required for elevated IOP.[38] Additionally, myocilin perfused anterior segments showed an increase in IOP, whereas eyes treated with denatured myocilin or other proteins such as bovine serum albumin showed no IOP increase.[40, 41] However myocilin has been shown to be upregulated under extended high IOP[42] and with mechanical stretch[43] pointing to a possible role in stress response that may explain upregulation during extended steroid exposure.

1.2.2 Mutant Myocilin and Glaucoma

Over 100 mutations have been documented in myocilin with many implicated in an early onset of OAG.[44] 10-30% of juvenile OAG and 2-4% of all POAG cases are linked with myocilin mutations.[45] The underlying cause of mutant myocilin-associated glaucoma, like steroid induced glaucoma, is not well understood. Several models for mutant myocilin pathogenesis have been put forward. Similar to the overexpression of myocilin due to steroid exposure, mutations in myocilin might lead to overexpression of myocilin and accumulation in the TM obstructing outflow,[46] or mitochondrial membrane disruption.[23] The prevalent mechanism proposed for mutant myocilin pathogenesis is that of a toxic gain of function of mutant myocilin aggregates within the endoplasmic reticulum (ER) of TM cells that eventually leads to TM cell death and dysregulation of outflow through the TM and increased IOP (Figure 1.2).[47] Indeed myocilin mutants have lower thermal stability than wild type myocilin,[48] and have been shown to grow amyloid-like fibrils,[49] furthering this hypothesis. Myocilin localization to the sheath materials of the corneoscleral meshwork and juxtacanalicular tissue may play a role in glaucoma pathogenesis as increased sheath materials are seen in glaucomatous eyes.[50, 51] While the pathophysiology of myocilin glaucoma in both steroid induced and OAG forms is still not understood. The study of the role of myocilin in disease progression is also hindered by the limited knowledge of native myocilin structure and function.

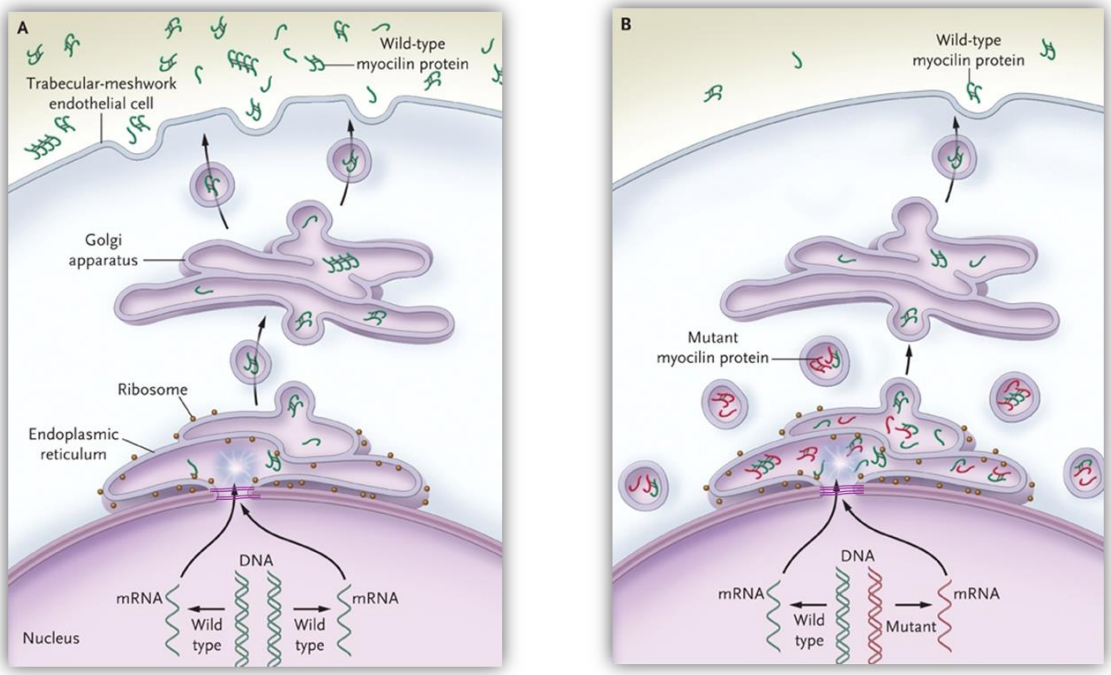

Figure 1.2 Myocilin secretion and accumulation. a. Wild type myocilin is secreted to the ECM. b. Mutant myocilin sequesters native myocilin and prevents secretion of both species. Reproduced with permission from[8]. Copyright Massachusetts Medical Society.

1.2.3 Myocilin as a Potential Therapeutic Target for Glaucoma

Once diagnosed, options to treat glaucoma fall into several classes all of which target lowering IOP as a method to slow disease progression.[52] IOP is modulated by decreasing AH production or increasing outflow though the uveoscleral pathway or the conventional pathway. Small molecules used now to treat glaucoma were all originally developed for other diseases. Even though drugs are generally applied topically to the eye, the five classes of current therapies are not selective to eye tissues.

Myocilin is one of the first identified modifiable drug targets to treat glaucoma. Early studies demonstrated that mutant myocilin secretion could be rescued by culturing TM cells at a lower temperature,[47, 53, 54] presumably because aggregation rates are slowed at temperatures below the unfolding temperature of mutant myocilin. Thus far, attempts to rescue secretion using small molecules have included both chemical and pharmacological chaperone approaches. For the former approach, a series of osmolytes were shown to increase thermal stability of mutants to better than wild-type levels in vitro,[48, 55] with simple compounds, like sucrose, exhibiting the most potent stability enhancement. The chemical chaperones TMAO[56] and 4-phenylbutyrate (4PBA)[57] also improved secretion of mutant myocilin; however, the high concentrations needed by chemical chaperones to enhance the stability of myocilin limit their usefulness as therapeutics. With no known function for myocilin, there is no biochemical assay for the discovery of pharmacological chaperones, and secondary assays such as cell secretion and inhibition of aggregation are low-throughput, making their use as a screening method laborious. One method for a high-throughput, target-independent stability assay was developed in which myoc-OLF was slightly destabilized and subsequent stabilization due to addition of ligand was monitored to determine potential scaffolds that bind to myoc-OLF. From this assay, two compounds were found that restored wild type thermal stability, inhibited amyloid formation and increased secretion.[58] Additionally, the recent crystal structure of myoc-OLF, should accelerate the discovery of new selective ligands for myocilin with similar properties through *in silico* drug design methods.[59]

1.3 Myocilin Localization, Function and Characterization

Myocilin is a 504 amino acid protein that is expressed in several tissues in the eye including the TM, retina, iris and ciliary epithelium,[60] but is also expressed in non-ocular tissues such as the sciatic nerve[61] and skeletal muscle.[37] Myocilin has been found to be localized primarily extracellularly, depending upon the tissue,[60] and has been shown to be proteolytically cleaved, in a calcium dependent manner, by calpain II into an N-terminal domain and a C-terminal olfactomedin (OLF) domain; both the C-terminal OLF domain and full length myocilin can be secreted.[62] The N-terminal domain contains a leucine zipper/coiled-coil region, predicted glycosylation sites[33] and is responsible for the multimerization of myocilin.[33, 63] The C-terminal OLF domain is predominantly β-sheet[64] and harbors ~90% of glaucoma casing mutations found in myocilin.[65] OLF domains are found in proteins expressed throughout the body, but have no known function, and until this work, were of unknown structure.

Myocilin has been shown to interact with various ECM structural proteins and likely has varied functions outside the cell. The interaction of myocilin and fibronectin has been implicated in modulating cell matrix interactions in the TM[66] and impairing formation of focal adhesions by blocking incorporation of paxillin.[67] Myocilin has also been implicated in modifying signaling pathways such as cytoskeletal restructuring through a non-canonical Wnt signaling pathway,[68] and inducing cell proliferation and survival of apoptosis by affecting the extracellular signal related kinases 1/2 (ERK 1/2) pathway.[69] Furthermore, as previously mentioned, myocilin may play a role in stress response, as mechanical stress[43] and elevated IOP[42] have been shown to increase myocilin expression in the TM. Although myocilin is widely accepted to be a secreted protein, it has also been shown to interact with mitochondria in TM cells, astrocytes,[70] and microtubules.[71] Recently, myocilin was further implicated in modulating the intrinsic apoptotic pathway

during retinal development,[72] specifically by modulating BCL2L1 expression levels and inducing retinal neuron cell death in mice overexpressing myocilin, or reducing retinal neuron cell death in myocilin knockout mice. Flotillin-1 is, to date, the only identified interacting partner of the OLF domain of myocilin;[73] most reported protein-protein interacting partners are localized to the N-terminal domain,[63, 68, 74, 75] but many of these interactions have not been confirmed by other laboratories or further studies. In sum, the biological function of myocilin is unclear and an active area of investigation.[45]

1.3.1 Potential Calcium Binding Site in Myocilin

Myocilin is predicted to be localized to various calcium rich cellular regions, initially during folding in the ER, as part of its purported role in the mitochondria, or as a secreted protein to the ECM where calcium binding is common,[76] including that of eye tissues where calcium levels are high.[77, 78] Most calcium binding motifs contain aspartate or glutamate residues to coordinate calcium, and OLF domains have many highly conserved aspartate residues. Prior work demonstrating stabilization of the negatively-charged myocilin and glycosaminoglycans pointed to a potential role for calcium, or other metal ion, to mediate binding.[64, 79] Taken together, with the calcium dependent cleavage of myocilin by calpain II,[62] we tested the hypothesis that myocilin harbors a calcium binding site, or multiple such sites, in the OLF domain (see Chapter 2).

1.3.2 Myocilin Amyloid Propensity

Glaucoma-associated mutant myocilin has been shown to form intracellular aggregates[47, 80] and wild type myocilin is also associated with aggregation when overexpressed.[38] Prior work from the lab demonstrated that the β-sheet rich OLF domain of myocilin, which harbors the majority of disease related mutations that thermally

destabilize myocilin OLF (myoc-OLF), are folded at room temperature and retain similar secondary structure to wild type.[48] At physiological temperatures, thermally destabilized myocilin mutants are expected to accumulate a population of unfolded protein that should be cleared by endoplasmic reticulum associated degradation (ERAD); surprisingly, this is not the case for myocilin mutants which instead induce the ER stress response, leading to cell death.[81, 82] Mutant myocilin can also cause a decrease in wild type myocilin secretion as has been shown with other amyloidogenic proteins.[83] Consistent with a toxic gain of pathogenic function hypothesis for mutant myocilin, the myocilin knockout mice,[84] and individuals with truncated myocilin,[85] do not get glaucoma.

1.4 Thesis Objectives

1.4.1 The Glaucoma-Associated Olfactomedin Domain of Myocilin is a Novel Calcium Binding Protein

Since calcium ions are important biological cofactors that play numerous roles in ECM proteins, the calcium binding properties of the myoc-OLF domain were examined. Our study reveals an unprecedented high affinity calcium-binding site within the myoc-OLF domain. The calcium ion bound to wild-type OLF remains largely intact throughout the purification process. A glaucoma-causing OLF variant, myoc-OLF(D380A), is calcium-depleted. Key differences in secondary and tertiary structure between myoc-OLF(D380A) and wild-type myoc-OLF, as well as limited access to chelators, indicate that the calcium binding site is largely buried in the interior of the protein. Analysis of six conserved aspartate or glutamate residues and an additional 18 disease-causing variants revealed just two other candidate residues that may be involved in calcium coordination. This

finding expands our knowledge of calcium binding in ECM proteins; provides new clues into domain structure, function, and pathogenesis for myocilin; and insights into highly conserved, biomedically-relevant OLF domains.

1.4.2 Determination of Amyloidogenic Peptide Stretches in the Myocilin Olfactomedin Domain

Prior work in the lab demonstrated that wild-type and mutated myoc-OLFs can form amyloidogenic fibrils *in vitro*.[49] The systematic investigation of experimental conditions leading to amyloid formation, including varying salt concentration, mechanical rocking, and pH for wild-type, or mutant myocilin yielded two distinct fibril morphologies. Assessment of the myoc-OLF sequence with online amyloid prediction servers yielded three distinct sequences with amyloid propensity. Two of the three predicted amyloidogenic peptide stretches grew fibrils, which matched morphologies seen for the OLF domain. These peptides may represent the portions of the myoc-OLF sequence responsible for fibril formation.

1.4.3 Structural Characterization of the Myocilin Olfactomedin Domain

In this chapter, we present the analysis of three crystal structures of the myoc-OLF domain. The structures reveal a new addition to the small family of five-bladed β-propellers. A calcium ion, sodium ion and glycerol molecule were identified within a central hydrophilic cavity that is accessible via movements of surface loop residues. Evolutionary analysis mapped onto the myoc-OLF structure reveals conserved and divergent regions

for possible overlapping and distinctive functional protein–protein or protein–ligand interactions across the broader OLF domain family.

1.4.4 Structural Implications for Glaucoma Pathogenesis

Myocilin glaucoma is a protein folding disorder similar to Alzheimer's, Parkinson's and Huntington's diseases.[86] While wild-type myoc-OLF is a well-folded monomer, single glaucomatous point mutations impair folding to the extent that only insoluble aggregates are isolated.[48] By mapping familial glaucoma-associated lesions onto the myoc-OLF structure, three regions sensitive to aggregation have been identified, with direct applicability to differentiating between neutral and disease causing non-synonymous mutations documented in the human population worldwide. The assignment of newly discovered mutations as disease causing can be aided by their location within one of the three identified regions.

1.4.5 Identification of Ligand Binding Sites in the Myocilin Olfactomedin Domain

The functions of myocilin and OLF domains in general remain elusive. The three crystal structures of the myoc-OLF domain offer the first opportunity for structural based prediction of ligand binding which may offer insight into the functions of myocilin and OLF domains. Additionally, the structures offer the first opportunity for *in silico* drug design to potentially treat myocilin glaucoma. The comparison of experimental and computational ligand binding of the three myoc-OLF structures is presented here.

CHAPTER 2

THE GLAUCOMA-ASSOCIATED OLFACTOMEDIN DOMAIN OF MYOCILIN IS A NOVEL CALCIUM BINDING PROTEIN

2.1 Introduction

Present at millimolar concentrations, calcium ions play versatile roles in the extracellular milieu.[87] Extracellular calcium ions are important in maintaining numerous cell-cell, cell-matrix, and matrix-matrix interactions, and accordingly, binding sites for calcium exist within associated ECM proteins.[88] Compared to our understanding of the roles of calcium in wound healing and blood coagulation, and in matrices like bone, our comprehension of the roles of calcium in tissues of the eye is largely limited. Despite the fact that ocular hypertension accompanying the highly prevalent ocular disorder glaucoma is treated with calcium channel blockers and adrenergic receptor agonists to affect salt concentrations,[89] and even though metal ions are recognized important regulatory factors in fluid outflow through the TM tissue involved in maintaining IOP,[90] details are largely missing.

Myocilin is a unique component of the TM linked to glaucoma pathogenesis. First, myocilin is linked to steroid-induced, secondary forms of glaucoma. Steroid treatment increases myocilin expression,[91] and high levels of myocilin have been linked to activation of the unfolded protein response in Drosophila eyes,[92] but the pathogenic mechanism has not yet been elucidated.[93] Second, mutations in myocilin comprise the strongest genetic linkage to POAG, the most prevalent disease subtype. Inherited in an autosomal-dominant fashion, non-synonymous mutations in myocilin, localized to its enigmatic OLF domain,

result in the accumulation of myocilin within human TM cells instead of secretion to the TM.[45] The scenario presents a toxic gain of function wherein TM cells expressing mutant myocilin die and, by an unknown mechanism, lead to an increase in IOP, which brings about the premature onset of glaucoma symptoms. Overall, myocilin-associated inherited glaucoma falls into a protein conformational disorder; mutant myocilin aggregation may be a function of the fact that disease-causing myoc-OLF variants are less stable than their wild-type counterpart.[48] and/or its ability to form amyloid fibrils.[94]

Paradoxically, in spite of its clear disease relevance, little is known about the structure or normal biological function of myocilin in the TM. In studies of full-length myocilin, ECM interacting partners such as actin, laminin, fibronectin, and heparan sulfate, as well as cell-matrix adhesion properties, have been localized to the N-terminal coiled-coil, not the OLF domain.[75, 79, 95-97] In addition, the explicit function of non-myoc-OLF homologs, distributed throughout the body and commonly found in neural tissues, is also unknown.[98] Other than myocilin, there has been limited functional and molecular characterization of other OLF-containing proteins, such as amassin-1, a sea urchin protein involved in cell-cell adhesion of coelomocytes,[99] gliomedin involved in nerve conduction within myelinating fibers,[100] and olfacomedin-4, which has recently emerged as a factor in a variety of human disorders, including some cancers [101-103] and irritable bowel syndrome.[104]

Based on the prevalence of calcium levels measured in ocular tissues [77, 78] like other ECM tissues,[76] we set out to investigate whether the OLF domain of myocilin harbors a calcium-binding site. The presence of numerous highly conserved aspartates among OLF domains and interaction of myocilin with negatively charged glycosaminoglycans[79] further suggest a need for such charge stabilization. Although sequence-gazing and bioinformatics approaches failed to identify any canonical calcium binding motifs, we

experimentally identified and characterized an unprecedented, single, high affinity, calcium binding site within the OLF domain of myocilin. This site is likely prevalent among most other OLF domains. Specific to myocilin, our results suggest new roles in the TM and its possible contribution to the pathogenesis of glaucoma.

2.2 Results

2.2.1 Initial identification of Calcium Stabilization in Myocilin Olfactomedin

Previous assays of the effects of metal ions on myoc-OLF excluded calcium ions due to experimental design.[64] Reassessment of myoc-OLF stability with calcium ions in a compatible buffer revealed a clear increase in thermal stability over Mg^{2+} and independent of anion, as measured by differential scanning fluorimetry (DSF) (Table 2.1, see Methods), a technique that reports ligand binding as an increase in thermal stability.[105] This phenomenon is observed even in the case of a fully-bound protein when the ligand only binds the folded state of the protein.[106]

Table 2.1 Analysis of stabilization of Myoc-OLF by divalent metal ions.

Sample	T_m (°C)	ΔT_m (°C)
Myoc-OLF	53.0 ± 0.5	--
Myoc-OLF + 10 mM $CaCl_2$	59.6 ± 0.2	6.6
Myoc-OLF + 10 mM $Ca(OAc)_2$	60.0 ± 0.1	7.0
Myoc-OLF + 10 mM $MgCl_2$	52.8 ± 0.2	-0.2
Myoc-OLF + 10 mM $Mg(OAc)_2$	53.6 ± 0.5	0.6
Myoc-OLF, pH 4.6	48.9 ± 0.1	--
Myoc-OLF, pH 4.6 + 10 mM $CaCl_2$	53.6 ± 0.1	4.7

2.2.2 Elemental Analysis by Inductively Coupled Plasma Optical Emission Spectroscopy

Given the fact that the typical purification procedure involves numerous hours of contact with buffers containing 1 mM ethylenediaminetetraacetic acid (EDTA) (K_d = 3.2 x 10^{-8} M for Ca^{2+} [107]), we expected the as-isolated maltose binding protein-myoc-OLF fusion protein (MBP-OLF) to lack Ca^{2+}. However, elemental analysis by ICP-OES (Table 2.2) revealed significant levels of Ca^{2+}. Omission of EDTA from the purification procedure yielded nearly stoichiometric values consistent with a single bound Ca^{2+} to the monomeric MBP-OLF; Ca^{2+} does not co-purify with maltose binding protein (MBP) (Table 2.2).

Table 2.2 Elemental analysis for Ca^{2+} by ICP-OES.

Sample	Ca: protein (per mole)
MBP-OLF as-isolated	0.81
EDTA-free MBP-OLF	0.96
MBP-OLF (D380A)	0.10
MBP	0.01

2.2.3 Release of Calcium upon Unfolding

When incubated with Quin-2, a fluorescent ethylene glycol tetraacetic acid (EGTA) analog with K_d= 2.9 x 10^{-9} M,[108] high fluorescence values indicative of Ca^{2+} release from myoc-OLF were only detected under denaturing conditions (Figure 2.1).

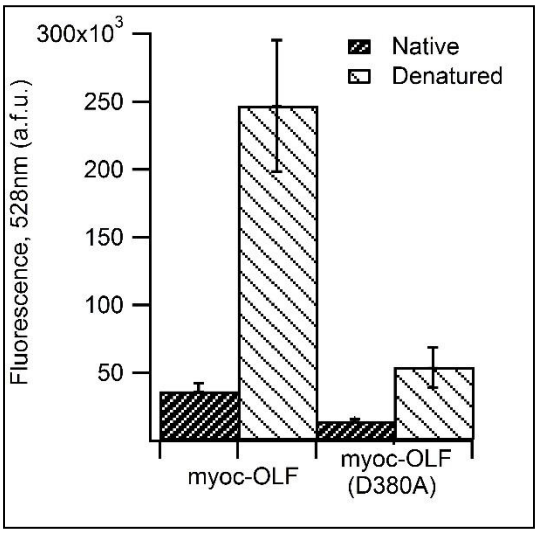

Figure 2.1 Ca^{2+} binding assay for myoc-OLF and myoc-OLF(D380A). Fluorescence of chelator Quin-2 due to Ca^{2+} binding measured under native and denaturing conditions.

2.2.4 Calcium Binding Monitored by Isothermal Titration Calorimetry

To date, we have not been able to prepare a native form of apo myoc-OLF or fully reload myoc-OLF; isothermal titration calorimetry using cleaved myoc-OLF reveals only non-specific binding; no additional binding sites are apparent (Figure 2.2).

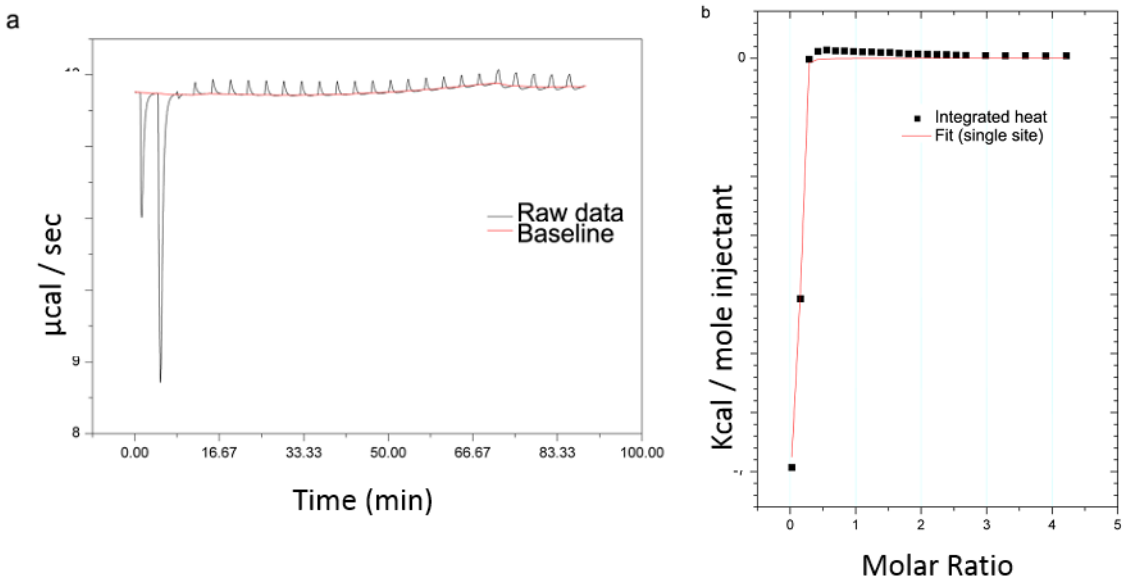

Figure 2.2 Calorimetric titration of myoc-OLF with Ca^{2+}. a. Raw data from titration of 270 µM myoc-OLF with 10 µl aliquots of 5 mM CaCl2 in 20 mM MOPS pH 7.2 at 25 °C. b. Plot of integrated heat versus Ca^{2+}/protein molar ratio. Fit to a single binding site indicates ratio of 0.1 Ca^{2+}/protein. Additional titrations with different concentrations of myoc-OLF and $CaCl_2$, as well as at higher temperature, did not alter this ratio, supporting the conclusion of non-specific binding to largely metal incorporated myoc-OLF (see Table 2.2).

2.2.5 Mutational Analysis of Carboxylic Acid-Containing Residues as Ligands for Calcium Reveals Glaucoma-Associated Aspartate 380

To deduce the metal binding residues in myoc-OLF, and in light of the fact that there is no enzymatic activity reported for myocilin we tested site-directed myoc-OLF mutants for stabilization by Ca^{2+}. A variant that loses its ability to be stabilized by calcium is lacking a candidate ligand. A total of six candidate conserved aspartates or glutamates, commonly found as ligands to calcium ions in proteins,[109] were identified by sequence analysis of the myoc-OLF domains from other organisms (Figure 2.3). Of these, Asp 273, Asp 378, Asp 384, and Glu 385 were replaced with alanine. Asp 380 was previously mutated to alanine, and is also a disease-causing variant.[55] The sixth, Asp 490, is removed when generating the core-OLF.[64] Myoc-OLF(D378A) could only be isolated in an aggregated state, and thus stability measurements on the folded monomer could not be conducted. The challenge encountered with myoc-OLF(D378A) is somewhat surprising given that the equivalent position in the non-myocilin OLF domain of the orthologue amassin contains an alanine (Figure 2.3, gi_28453877). Both myoc-OLF(D273A) and myoc-OLF(D380A) were isolated as monomers in sufficient quantities and their stabilities were found to be unaffected the presence of Ca^{2+}. Due to the low initial stability of the D273A variant (T_m = 22 °C), however, we only cautiously implicate Asp 273 as a ligand for Ca^{2+} in myoc-OLF. By contrast, the D380A variant, also a disease-causing residue (see below), is a moderately stable protein (T_m = 46 °C) and could be evaluated further. In addition to completely ablating stabilization by Ca^{2+}, myoc-OLF(D380A) does not co-purify with Ca^{2+}, as confirmed by Quin-2 binding (Figure 2.1) and metal analysis (Table 2.2). Based on these results, Asp 380 is a strong candidate as Ca^{2+} binding residue in myoc-OLF.

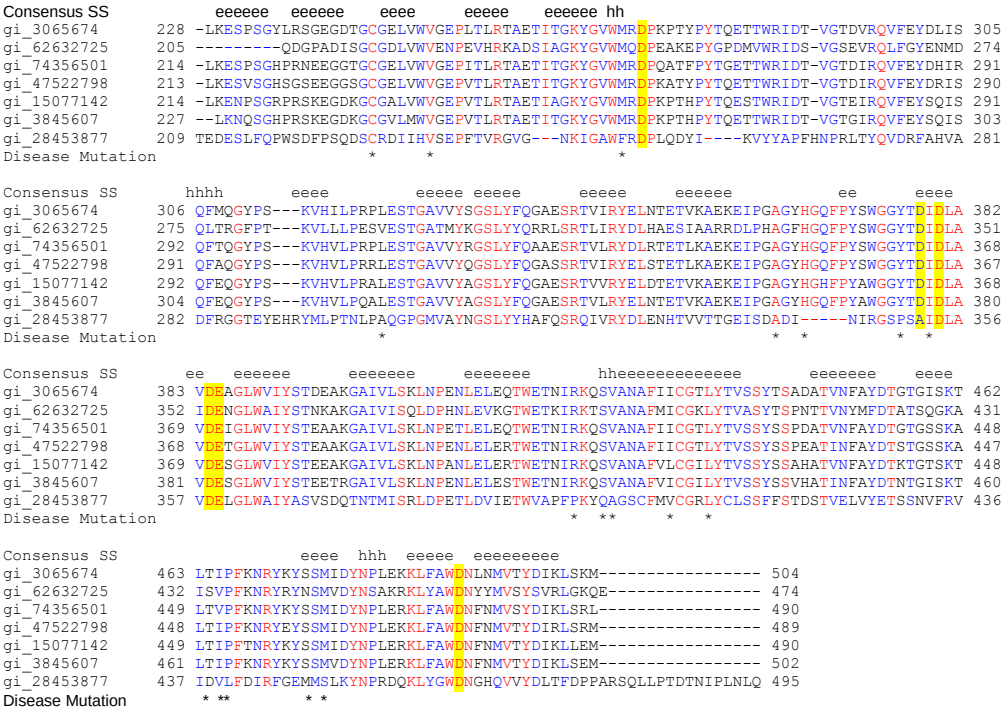

Figure 2.3 PROMALS [110] sequence alignment of the OLF domain of myocilins. From human (gi_3065674), zebrafish (gi_62632725), cow (gi_74356501), pig (gi_47522798), mouse (gi_15077142) and rat (gi_3845607), as well as (non-myocilin) amassin (gi_28453877) from sea urchin. Consensus secondary structure (SS) is depicted above the alignment. e = β strand, h = helix. Asterisk indicates location of glaucoma-causing mutation examined in this study. Red residues are identical, blue residues similar. Highlighted residues are conserved aspartate/glutamate positions subjected to site-directed mutagenesis in this study.

2.2.6 Structural Differences between Apo Myocilin Olfactomedin and Wild-Type Myocilin Olfactomedin

We next examined structural differences between apo and holo myoc-OLF by comparing circular dichroism (CD) spectra of wild-type at pH 7.2 and 4.6, and myoc-OLF(D380A) at pH 7.2 (CD spectra by Dr. Shannon Hill). Overall, the secondary structural features are rather similar, with features of β-sheets at ~215 nm and an unusual feature at 232 nm seen by us previously.[55, 64] However, myoc-OLF(D380A) has a more pronounced feature at 232 nm, similar to wild-type OLF at pH 4.6[64] (Figure 2.4 a). The 232 nm signal has been attributed to a change in β-turn secondary structure[111] as well as exposed tryptophan residues.[112] In support of the latter interpretation for myoc-OLF, the changes in tertiary structure observed in the aromatic region of myoc-OLF(D380A) nearly overlay with wild-type myoc-OLF at pH 4.6 (Figure 2.4 b). Notably, myoc-OLF at pH 4.6 is still stabilized by Ca^{2+} (Table 2.1). In sum, the structural changes in myoc-OLF(D380A) that lead to ablation of Ca^{2+} binding are due to the of the loss of coordination of Asp 380 to Ca^{2+}, and not an overall change in the structure of the Ca^{2+} binding pocket.

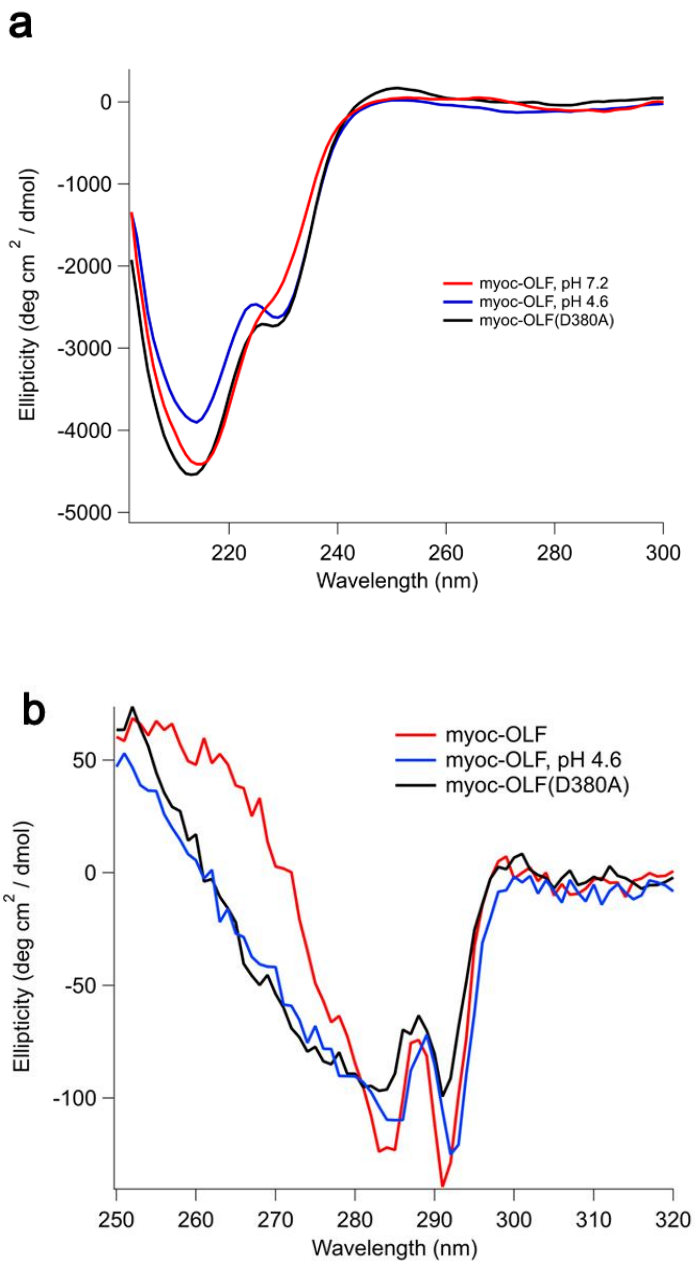

Figure 2.4 Structural comparison of myoc-OLF and myoc-OLF(D380A). Comparison of a. Secondary structure from far-UV spectra and b. tertiary structure from near UV spectra among wild-type myocilin -OLF at pH 7.2 (red), wild-type myoc-OLF at pH 4.6 (blue), and myoc-OLF(D380A) at pH 7.2 (black). Spectra acquired by Dr. Shannon Hill.

2.2.7 Investigation of Calcium Stabilization of 18 Other Disease-Causing Myocilin Olfactomedin Variants Reveals No Other Impaired Variants

Due to the documented participation of other polar residues or main chain-derived carbonyls in Ca^{2+} binding,[109] combined with the glaucoma-relevance of myoc-OLF, we looked at the extent of stabilization by Ca^{2+} by 18 disease-causing OLF mutants (Table 2.3). With the exception of D380A, all of the disease-causing variants were stabilized by +5.7-9.1 °C in the presence of 10 mM Ca^{2+}; wild-type myoc-OLF is stabilized by 6.5 °C. Although the extent of stabilization varies somewhat, we were unable to statistically correlate initial T_m or position in the amino acid sequence with extent of stabilization given a single Ca^{2+} concentration. Thus, the remaining cryptic Ca^{2+} coordination sphere likely involves some combination of other side chains not yet identified, main chain carbonyls, or water molecules.

Table 2.3 Analysis of stabilization of myoc-OLF variants by Ca^{2+}.

Variant	Rationale	Tm (˚C)	Tm (°C) + 10 mM $CaCl_2$	ΔTm (°C)
Myocilin OLF	wild-type	53.0 ± 0.5	59.6 ± 0.2	6.5
Myoc-OLF core	identified structural core[a]	49.7 ± 0.3	57.7 ± 0.1	8.1
MBP-OLF (G246R)	disease causing	42.7 ± 0.2	50.6 ± 0.0	8.1
MBP-OLF (G252R)	disease causing	43.0 ± 0.2	51.5 ± 0.2	8.5
MBP-OLF (R272G)	disease causing	41.0 ± 0.3	48.6 ± 0.1	7.6
MBP-OLF (D273A)	carboxylate side chain	21.7 ± 0.8	21.1 ± 0.7	-0.6
MBP-OLF (E323K)	disease causing	44.0 ± 0.5	50.3 ± 0.2	6.2
MBP-OLF (G364V)	disease causing	45.0 ± 0.4	51.9 ± 0.1	6.9
MBP-OLF (G367R)	disease causing	42.7 ± 0.1	50.9 ± 0.4	8.1
MBP-OLF (T377M)	disease causing	44.3 ± 0.3	50.6 ± 0.6	6.3
MBP-OLF (D378A)	carboxylate side chain	N/A	N/A	N/A[b]
MBP-OLF (D380A)	carboxylate side chain & disease causing	46.6 ± 0.3	45.1 ± 0.5	-1.5
MBP-OLF (D384A)	carboxylate side chain	42.5 ± 0.7	53.6 ± 0.5	11.1
MBP-OLF (E385A)	carboxylate side chain	39.7 ± 0.4	49.7 ± 0.3	10
MBP-OLF (K423E)	disease causing	34.2 ± 0.4	43.2 ± 0.1	9.0
MBP-OLF (V426F)	disease causing	41.5 ± 0.1	49.9 ± 0.1	8.4
MBP-OLF (A427T)	disease causing	48.3 ± 0.3	55.1 ± 0.4	6.9
MBP-OLF (C433R)	disease causing	40.4 ± 0.4	49.4 ± 0.5	9.0
MBP-OLF (Y437H)	disease causing	40.3 ± 0.4	48.6 ± 0.2	8.3
MBP-OLF (I477N)	disease causing	37.7 ± 0.8	46.8 ± 0.2	9.1
MBP-OLF (I477S)	disease causing	39.7 ± 0.2	48.2 ± 0.5	8.5
MBP-OLF (N480K)	disease causing	42.4 ± 0.2	48.1 ± 0.1	5.9
MBP-OLF (P481L)	disease causing	45.5 ± 0.4	51.2 ± 0.3	5.7
MBP-OLF (I499F)	disease causing	42.8 ± 0.1	50.4 ± 0.4	7.6
MBP-OLF (S502P)	disease causing	41.0 ± 0.3	49.9 ± 0.2	8.9

[a]from *64*

[b]variant could not be purified in sufficient quantities in folded state for measurement

2.2.8 Estimation of Calcium Dissociation Constant

Because a strictly apo wild-type myoc-OLF protein could not be prepared for direct calorimetric measurement of calcium binding, we estimated the dissociation constant from experimental T_m values obtained by differential scanning calorimetry (DSC) (see Methods, experiment completed by Katherine Turnage), which are corroborated by CD (Figure 2.5) and DSF (Table 2.3), as well as experimental values for the enthalpy of unfolding and change in heat capacity for myoc-OLF (D380A) as a proxy for apo myoc-OLF. These values lead to a calculated K_d ~ 1.3 x 10^{-6} M for Ca^{2+} in myoc-OLF (Calculations by Dr. Raquel Lieberman). Combined with results from CD and inaccessibility to chelators under native conditions, we infer that the myoc-OLF Ca^{2+} binding site has limited solvent accessibility.

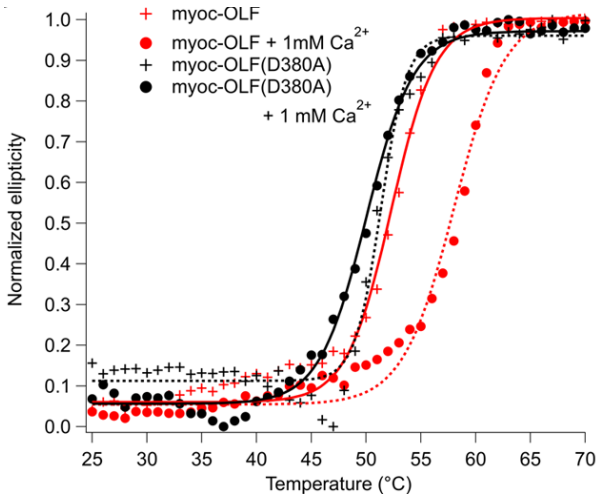

Figure 2.5 Stability comparison of myoc-OLF and myoc-OLF(D380A). CD thermal melts for myoc-OLF and myoc-OLF(D380A) in MES pH 6.0, monitored at 215 nm in the presence and absence of exogenous Ca^{2+}.

2.2.9 Prediction of Calcium Binding Motifs in Olfactomedin Domain Family

Finally, we broadened our scope beyond myocilin to include other OLF domain containing proteins, in order to gain insight into whether calcium binding may be an inherent characteristic of such domains. Among myocilin orthologues, D380 is located in a well-conserved region of the OLF domain peppered with acidic residues that were subjected to mutagenesis in our study (see above). Expansion of sequence analysis to include 45 OLF homologs available in ProSite,[113] combined with an evolutionary trace,[114] reveals that all but one distant branch harbors an aspartate or glutamate at the equivalent position of 380 in myocilin (Figure 2.6). Instead of aspartate, these distant relatives, the gliomedins, harbor asparagine, which is unlikely to be a ligand for calcium. Notably, Asp 273 is highly conserved among the expanded list of OLF domains, with the only outliers in the same branch lacking a Asp 380. Asp 378 is far less conserved, being replaced with tyrosine, leucine and phenylalanine. Thus, while many variants appear to have a well-positioned aspartate for calcium binding, additional characterization of other OLF domains will be required to assess further generality in the superfamily.

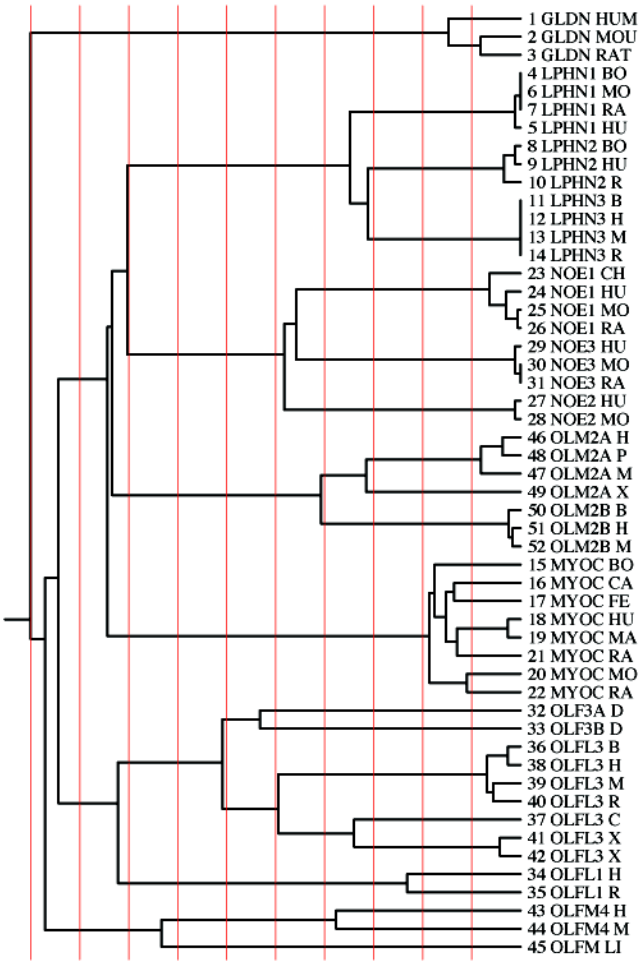

Figure 2.6 Evolutionary tree for 45 OLF domains. Human myocilin is listed as number 18. Family members that harbor Asn 380 are listed 1-3.

2.3 Discussion

A novel, high affinity Ca^{2+} site was identified within the OLF domain of myocilin. The myoc-OLF Ca^{2+} binding site contains an unprecedented motif that includes Asp 380, the site of a glaucoma-causing lesion. Of the 23 total myoc-OLF variants we investigated, including mutants of conserved aspartate/glutamate residues, as well as disease-causing mutants, only two additional candidate ligands emerged. However, neither position could be confirmed unambiguously due to the severely impaired biophysical properties of the resulting recombinant protein. The combination of low thermal stability of myoc-OLF(D273A) and high level of conservation of aspartate among orthologues at this position underscores the importance of this residue to the integrity of the OLF domain. This stability reduction is highly residue-specific, however; myoc-OLF(R272G), the adjacent disease variant, is a moderately stable protein that is stabilized by calcium. By comparison, while Asp 378 could form part of the prevalent D-X-D Ca^{2+} binding loop found in EF-hands and β-blades, the remaining motif is absent and Asp 378 is not well conserved among OLF domains. In addition, Asp 380 is predicted to be located within a β-strand. The varied nature of calcium binding sites in proteins, which include not only oxygen-containing amino acid side chains but also main chain carbonyls, hydroxyl moieties, and water molecules for a total coordination number of 6-8,[115] may render the remaining Ca^{2+} coordination environment in the myoc-OLF inaccessible by site-directed mutagenesis. Indeed, the remaining Ca^{2+} coordination environment in the myoc-OLF domain remained enigmatic until the structure was solved (see Chapter 4).

Two of the major proposed functions of Ca^{2+} binding sites in ECM proteins are the enhancement of thermal stability and protection against proteolysis.[76] In support of these roles, we previously observed resistance of myoc-OLF to protease treatment[64] and core-OLF is still stabilized by calcium. Unlike other known calcium-containing ECM proteins like

osteonectin, in which the binding of calcium induces a large conformational change,[116] wild-type and myoc-OLF(D380A) have highly similar structural features. Thus, although myoc-OLF is more stable than the D380A mutant to thermal denaturation, calcium is not absolutely required for OLF folding.

The estimated binding affinity of the myoc-OLF calcium site based on available thermodynamic parameters is also in line with Ca^{2+} equilibrium dissociation constants of other ECM proteins, which are usually in the micromolar range.[88] However, myocilin is atypical in that the site is largely inaccessible to the strong chelators EDTA and Quin-2. This indicates that metal binding likely occurs upon folding in the calcium-rich ER[117] and once trafficked to the TM, the myoc-OLF domain should be continually saturated with Ca^{2+}, based on experimental measurements of millimolar levels of calcium ions in AH.[77, 78]

In addition to conferring stability, Ca^{2+} sites in ECM proteins play regulatory or signaling roles, for example, in response to local calcium ion gradients.[88] The emerging picture appears true in proteins with a stabilizing, high affinity Ca^{2+} site, regardless of whether Ca^{2+} is bound within a single protein domain or at the interface between domains. Calcium ions may directly facilitate ligand interaction or membrane association, or stabilize a particular protein conformation so that it is primed for ligand binding or activated for catalysis.[87] Full-length myocilin is a modular protein like other ECM proteins, but myocilin is unusual in that it has a coiled-coil for oligomerization instead of a repeated domain structure within a single polypeptide chain. The OLF domain behaves as a monomer in vitro,[55, 64] and it has been suggested that the myocilin domain structure brings OLF domains in close proximity, albeit in an unknown configuration. Even though all but one[73] of the interacting partners for myocilin identified to date appear to not require the OLF domain, the interaction may be calcium-dependent, or require a transient calcium gradient.

For example, in the case of amassin, cell-cell interactions were found to be contingent upon the presence of calcium ions.[118]

Alternatively, or in addition, myocilin may be sensitive to shear stress and play a role in signaling a response to biomechanical stress. Indeed, the anterior chamber of the eye, including the sponge-like TM tissue, constantly experiences and responds to biomechanical changes as a result of normal fluctuations in fluid flow and activities such as blinking and eye rubbing.[119] For most individuals, the response is robust throughout one's life, indicative of a highly regulated signaling pathway, although one that is poorly understood. For others, prolonged fluid shear stress from AH flow, and/or compression and stretching of the TM, and/or aging-related morphological changes, leads to chronically elevated IOP, and glaucoma-associated vision loss at the optic nerve.

In support of this involvement, myocilin mRNA levels have been shown to be elevated in response to mechanical stress,[43] which includes rearrangements of actin filaments.[120] Myocilin is proposed to interact with actin via its coiled-coil[97] but such changes could propagate to strip myoc-OLF of its calcium ion, with two thought-provoking fates. First, TM remodeling could arise as a consequence of proteolytic susceptibility upon metal depletion or by introducing additional calcium to the TM milieu. Second, apo myocilin may be less compact and expose an amyloidogenic region leading to fibril formation, and in this way contribute to glaucoma pathogenesis. Steroid treatment may exacerbate one or both of these potential roles. Related, myocilin may play a part in the regulation of TM calcification. Genes associated with calcification are abundantly expressed in the TM. Although the details of calcification and/or prevention in the TM, and their physiological or pathological role(s), are still unknown,[121] myocilin mutants can alter the expression of calcification genes,[122] suggesting interplay is possible.

The new knowledge of a calcium site opens a completely new context in which to probe the biological and pathogenic roles of myocilin. Additional characterization of the OLF domain in the context of full-length myocilin, calcium fluxes and mechanical stress in the TM should yield new functional insights and contribute to our still poor comprehension of the role of Ca^{2+} in the anterior segment of the eye.

2.4 Methods

2.4.1 Protein Expression and Purification

Myoc-OLF and variants were expressed using a modified pMAL-c4x plasmid encoding an N-terminal MBP fusion (New England Biolabs) in Rosetta Gami 2 (DE3) pLysS (Novagen) cells, as described previously.[55] Cells were grown at 37 °C in Superior Broth (US Biological) to an optical density at 600 nm of 0.6-0.8, cooled to 18 °C, induced with 0.5 mM isopropyl β-D-thiogalactopyranoside (IPTG) and allowed to grow overnight (14-16 hours). Cells were flash frozen with liquid nitrogen, and stored at -80 °C. Cell pellets were lysed via French Press after suspension in amylose wash buffer (10 mM KH_2PO_4 , 10 mM Na_2HPO_4, 200 mM NaCl and 1 mM EDTA) containing Roche Complete EDTA-free Protease Inhibitor Cocktail. Cellular debris was removed via ultracentrifugation (162,000 x g for 45 minutes at 4 °C), and the supernatant loaded onto a 20 mL column containing high flow amylose resin (New England Biolabs), equilibrated with amylose wash buffer. The MBP-OLF fusion protein was eluted using amylose wash buffer supplemented with 10 mM maltose. Elution fractions were concentrated using Amicon Ultra-15 centrifugal filtration devices and loaded onto a Superdex 75 prep grade column (GE Healthcare) equilibrated with gel filtration buffer (10 mM KH_2PO_4, 10 mM Na_2HPO_4 and 200 mM NaCl, pH 6.8). Fractions of MBP-OLF monomer were identified by SDS-PAGE analysis, pooled

and concentrated for further use or for protease cleavage. Cleavage of MBP-OLF was accomplished using Factor Xa (New England Biolabs or Roche) incubated for 16-18 hours in 50 mM Tris pH 8, 100 mM NaCl, and 5 mM $CaCl_2$ at 37 °C (wild-type) or room temperature (variants). Cleaved protein was loaded onto the amylose resin column to remove MBP and uncleaved fusion protein. Flow-through fractions containing cleaved myoc-OLF and Factor Xa were concentrated and subjected to fractionation by Superdex 75 size exclusion column chromatography. Fractions containing cleaved, pure, myoc-OLF were identified by SDS-PAGE, pooled, and concentrated for further use.

2.4.2 Olfactomedin Variants

Site Directed Mutagenesis was accomplished using the QuickChange II® Site Directed Mutagenesis Kit (Stratagene). Primers were designed using PrimerX (bioinformatics.org) and synthesized by MWG Operon. Primers for sequences that were not published previously are in Table 2.4.[48, 55] All mutated plasmid sequences were confirmed by DNA sequencing (MWG Operon). Protein expression and purification proceeded as above. The structural core of myoc-OLF (core-OLF), which lacks Asp 490, was generated by limited proteolysis as previously described.[64]

Table 2.4 Primers used in this study.

Myoc-OLF (D273A)	5`-gtgtgtggatgcgagcgcccaagcccacctac
Myoc-OLF (D378A)	5`-cttggggtggctacacggcgattgacttggctgtggatg
Myoc-OLF (D384A)	5`-cattgacttggctgtggcggaagcaggcctctggg
Myoc-OLF (E385A)	5`-cattgacttggctgtggatgcggcaggcctctgggtcatta

2.4.3 Thermal Stability Assay

Changes in thermal stability were assessed by DSF[105] as modified by us previously for MBP-OLF.[55, 64] Briefly, 30 µL reactions containing final concentrations of 1-3 µM myoc-OLF or MBP-OLF variants were diluted into buffer containing 10 mM Hepes pH 7.5, 200 mM NaCl, and 5X Sypro Orange dye (Invitrogen). For MBP-OLF variants, 50 mM maltose was added to stabilize MBP well beyond the range of OLF.[55] Salts ($CaCl_2$, $Ca(OAc)_2$, $MgCl_2$, or $Mg(OAc)_2$) were added in the range of 0-25 mM. The mixtures were dispensed into 96-well optical plates and sealed with optical film (Applied Biosystems). Sypro Orange fluorescence was monitored as a function of temperature in an Applied Biosystems Step One Plus RT-PCR with fixed excitation at 480 nm and a ROX 610 nm emission filter. Thermal melts were conducted in triplicate on two independent samples from 25 to 95 °C (5-95 °C for myoc-OLF(D273A) and myoc-OLF(Y437H)) with 1 °C/min incremental increase. Fluorescence data were blank-subtracted, and Boltzmann Sigmoid analysis conducted using GraphPad Prism to determine the midway point of unfolding, i.e. the melting temperature (T_m).

2.4.4 Fluorescence Calcium Binding Assay

Purified proteins were concentrated and rediluted into 10 mM Hepes pH 7.5 three times, using aforementioned centrifugal filtration devices. The fluorescence of the nanomolar affinity Ca^{2+} chelator Quin-2[108] was then measured under native and denaturing[123] conditions. Reactions containing 8 µM myoc-OLF or myoc-OLF(D380A), 150 µM Quin-2 and either 0 or 1.4 M GndHCl in 10 mM Hepes pH 7.5 buffer were added to Grenier Bio-One Fluotrac 200 96 half-well plates. Fluorescence was measured on a Biotek Synergy 2 Plate Reader using filters for excitation at 360/40 nm and emission at

528/20 nm. At least two independent measurements were conducted. Reported fluorescence values are blank-subtracted.

2.4.5 Inductively Coupled Plasma Optical Emission Spectroscopy

As-isolated MBP-OLF was prepared for ICP-OES as described above, except using gel filtration buffer treated with Chelex resin (Sigma). Samples of EDTA-free MBP-OLF, MBP-OLF(D380A) and MBP were purified as reported except EDTA was omitted from amylose wash buffer and gel filtration buffer was chelated with Chelex resin. Duplicate independent samples of 74-95 μM protein and buffer blanks were analyzed for Ca^{2+} content at the University of Georgia Center for Applied Isotope Studies. Data were blank-subtracted, molar ratios calculated, and averages are reported. Protein concentrations for MBP-OLF and MBP-OLF(D380A) were based on the experimental molar extinction coefficient at 280 nm of 169,978 $M^{-1}cm^{-1}$ obtained from total amino acid analysis (UC Davis Molecular Structure Facility).

2.4.6 Circular Dichroism

Far-UV CD, near-UV CD spectra and CD thermal melts (all completed by Dr. Shannon Hill), were acquired on a Jasco J-810 spectropolarimeter equipped with Neslab RTE 111 circulating water bath and a Jasco PTC-4245/15 temperature control system. For far-UV spectra, samples included myoc-OLF and myoc-OLF(D380A) spectra in gel filtration buffer at pH 7.2. For myoc-OLF at pH 4.6, purified protein was subjected to 3x concentration and dilution into 10 mM sodium acetate, 200mM NaCl, pH 4.6 using an Amicon ultra 15 centrifugal device. For thermal melts, protein samples were first diluted into 10 mM MES pH 6.0 buffer and supplemented with 0 or 1 mM $CaCl_2$ to a final concentration of 10-12 μM. No differences in secondary structure were observed between

samples prepared in pH 6.0 or 7.2 (not shown). Far-UV spectra were acquired at 20 °C with 30 averaged scans from 300 to 200 nm at a 500 nm min^{-1} scan rate, using a 0.1 cm cuvette. Far-UV melts were performed in duplicate utilizing a 1 °C min^{-1} increase in temperature from 5 to 95 °C. Ten scans from 300 to 200 nm at a 500 nm min^{-1} scan rate were averaged for each temperature. Data were blank-subtracted and converted to mean residue ellipticity $\Theta = M_{res} \times \Theta_{obs} / 10 \times d \times c$, where M_{res}=112.9 is the mean residue mass calculated from the protein sequence; Θ_{obs} is the observed ellipticity (degrees) at wavelength λ; d is the pathlength (cm); and c is the protein concentration (g/ml). The T_m was determined using mean residue ellipticity values recorded at 215 nm via Boltzmann Sigmoid analysis using Igor Pro.

Near-UV CD experiments were conducted with myoc-OLF at pH 7.2, at pH 4.6, and myoc-OLF(D380A) at pH 7.2, as above (40 - 50 μM). Scans were measured from 250 nm to 320 nm at a rate of 50 nm/min and a data pitch of 1 nm using a 0.1 cm cuvette. Each measurement was an average of 10 scans, converted to mean residue ellipticity as above.

2.4.7 Estimate of Calcium Dissociation Constant

The K_d of Ca^{2+} for myoc-OLF was estimated with the binding constant macro in Origin 7 using data from DSC (completed by Katherine Turnage, MicroCal VP-Capillary DSC) conducted at 15.4 μM protein concentration in gel filtration buffer. The unfolding transitions for both myoc-OLF and myoc-OLF(D380A) are not reversible, but can be fit well to a non two-state model (not shown). Data from myoc-OLF(D380A) were used as an approximation for apo myoc-OLF (see Results). Relevant parameters: For myoc-OLF T_m = 56.3 °C, and for myoc-OLF(D380A), T_m = 51.5 °C, ΔH_{cal} = 8.22 x 10^4 kcal/mol, ΔC_p = 1450 cal/deg•mol (calculations completed by Dr. Raquel Lieberman).

CHAPTER 3

Determination of Amyloidogenic Peptide Stretches in the Myocilin Olfactomedin Domain

3.1 Introduction

Mutations in the protein myocilin are linked with POAG, and the vast majority of these mutations occur within the C-terminal OLF domain.[44] Myoc-OLF mutations are thermally destabilized compared to wild type,[48] and form cytotoxic aggregates that accumulate within the ER of TM cells.[47, 80] This aggregation eventually leads to cell death, reduced AH outflow and increased IOP, which is a major risk factor for glaucoma.[47] The pathogenesis of mutant myocilin is not well understood, as ERAD should clear the ER of misfolded proteins. Instead, mutant myocilin interacts aberrantly with resident ER chaperones preventing clearance by the proteasome.[124] The aggregation of myocilin, not the lack of secretion, appears to play a role in glaucoma pathogenesis, as myocilin knockout mice[84] and individuals with truncated myocilin[85] do not get glaucoma. This points to a toxic gain of function mechanism for pathogenesis associated with aggregation of myocilin mutants. Accordingly, similar to other amyloidogenic proteins, mutant myocilin can decrease wild type myocilin secretion.[83]

Systematic characterization of myoc-OLF fibrillization revealed that wild type myoc-OLF is well-folded and does not readily fibrilize unless partially unfolded either by temperature elevated above body temperature (42 °C) or lowered pH, and fully denaturing myocilin yields nonspecific aggregation.[125] Disease-associated mutants of myoc-OLF, however, have altered secondary and tertiary structures compared to wild type myoc-OLF,

and fibrilize readily at 36 °C (Figure 3.1).[125] Two distinct fibril morphologies, curvilinear and circular, are formed by wild type myoc-OLF at elevated temperature depending upon the presence of salt (Figure 3.2).[125] Of the three disease causing myoc-OLF mutations studied, A427T and I499F adopt the curvilinear fibrils and D380A forms circular fibrils.[125] Since myoc-OLF only grows fibrils when partially unfolded, we hypothesized that certain peptide stretches may exist within the myoc-OLF sequence that, upon exposure with partial unfolding, may contribute to the amyloidogenic properties of myocilin.

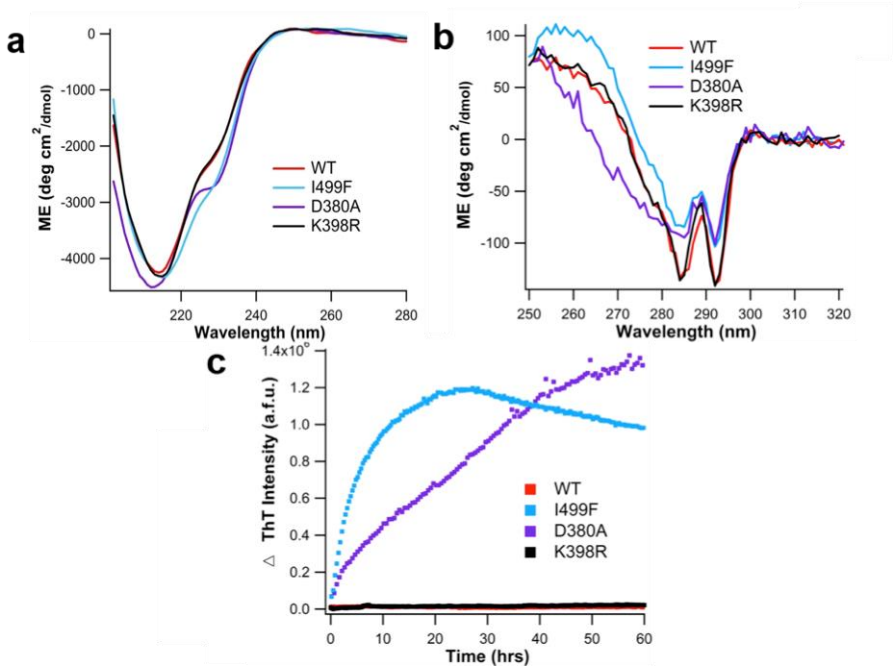

Figure 3.1 Structural properties and amyloid fibril growth of native and mutant myoc-OLF. a. CD spectra of variants, Wild type (WT) myoc-OLF, disease mutants A427T, I499F and D380A myoc-OLF and non-disease polymorphism K398R. b. Tertiary CD spectra variants. c.Thioflavin T (ThT) fluorescence of variants. (Spectra and fluorescence assay collected by Dr. Shannon Hill.[125])

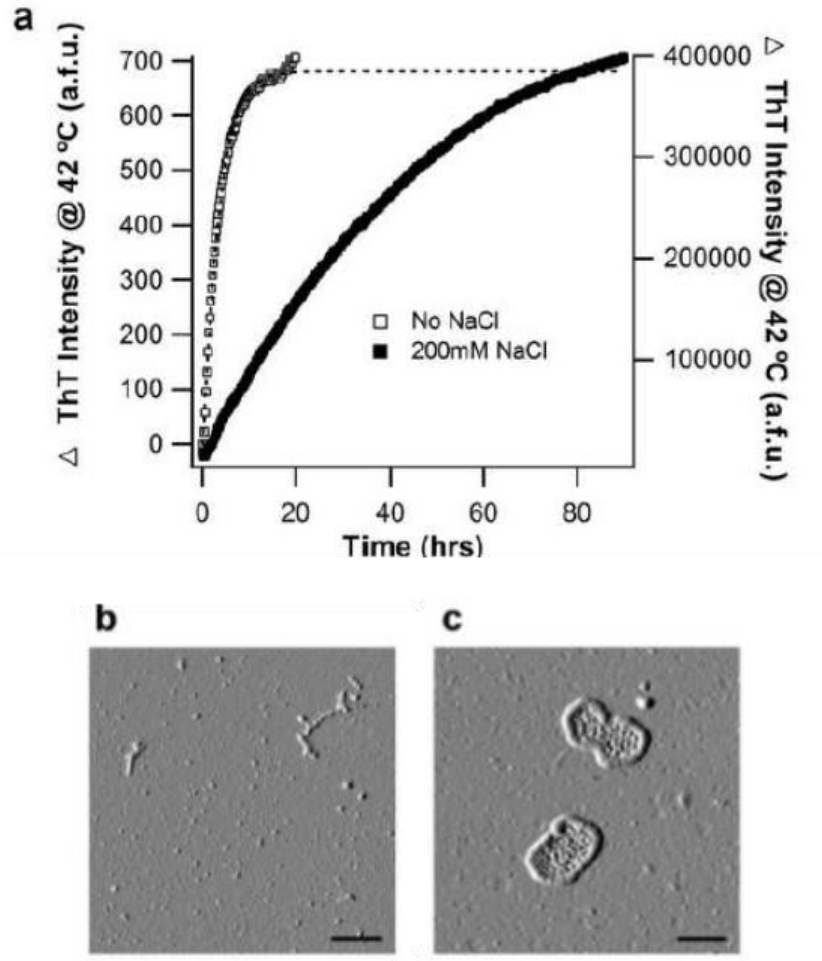

Figure 3.2 Myoc-OLF fibril growth with and without salt. a. Myoc-OLF fibril growth at 42 °C monitored by ThT fluorescence in the presence and absence of salt. Corresponding Atomic Force Microscopy (AFM) of fibrils formed in the absence (b) and presence (c) of salt. (Fluorescence assay and AFM images by Dr. Shannon Hill.[125])

3.2 Results

3.2.1 Initial Amyloid Prediction in the Olfactomedin Domain of Myocilin

To identify any stretches within myoc-OLF that have high amyloid propensity, full length myoc-OLF was submitted to four online amyloid prediction servers, Waltz[126], PASTA[127], Amyl_Pred[128] and TANGO[129]. These servers yielded 3 consensus peptide stretches of high amyloid propensity (Figure 3.3), G_{326}AVVYSGSLYFQ (P1), G_{387}LWVIYSTDEAKGAIVLSK (P2), and V_{426}ANAFIICGTLYTVSSY (P3). P3 was the highest predicted stretch followed by P1; P2 exhibited the lowest amyloid propensity (Figure 3.4).

LKESPSGYLRSGEGDTGCGELVWVGEPLTLRTAETITGKYGVWMRDPKPTYPYTQET
TWRIDTVGTDVRQVFEYDLISQFMQGYPSKVHILPRPLEST**GAVVYSGSLYFQ**GAESR
TVIRYELNTETVKAEKEIPGAGYHGQFPYSWGGYTDIDLAVDEA**GLWVIYSTDEAKGAI**
VLSKLNPENLELEQTWETNIRKQS**VANAFIICGTLYTVSSY**TSADATVNFAYDTGTGISK
TLTIPFKNRYKYSSMIDYNPLEKKLFAWDNLNMVTYDIKLSKM

Figure 3.3 Myoc-OLF sequence with predicted amyloidogenic stretches highlighted.

Peptide 1	G	A	V	V	Y	S	G	S	L	Y	F	Q
Waltz	+	+	+	+	+	+	+	+	+	+	+	+
PASTA	-	-	-	-	-	-	-	-	-	-	-	-
Amyl_Pred	-	-	-	-	-	+	+	+	+	+	+	+
TANGO	+	+	+	+	+	+	+	+	+	+	+	+
Predicted 2° Structure	-	β	β	β	β	-	-	β	β	β	β	β

Peptide 2	G	L	W	V	I	Y	S	T	D	E	A	K	G	A	I	V	L	S	K
Waltz	+	+	+	+	+	+	-	-	-	-	-	-	-	-	-	-	-	-	-
PASTA	-	-	-	-	-	-	-	-	-	-	-	-	-	-	-	-	-	-	-
Amyl_Pred	+	+	+	+	+	+	+	-	-	-	-	-	+	+	+	+	+	-	-
TANGO	+	+	+	+	+	+	+	-	-	-	-	-	-	-	-	-	-	-	-
Predicted 2° Structure	-	β	β	β	β	β	β	-	-	-	-	-	-	β	β	β	β	β	β

Peptide 3	V	A	N	A	F	I	I	C	G	T	L	Y	T	V	S	S	Y
Waltz	+	+	+	+	+	+	+	+	+	+	+	+	+	+	+	+	+
PASTA	+	+	+	+	+	+	+	+	+	+	+	+	+	+	+	+	+
Amyl_Pred	+	+	+	+	+	+	+	+	+	+	+	+	+	+	+	+	-
TANGO	+	+	+	+	+	+	+	+	+	+	+	+	+	+	+	+	+
Predicted 2° Structure	α	α	α	β	β	β	β	β	β	β	β	β	β	β	β	-	-

Figure 3.4 Amyloid propensity of selected peptides. Amyloid prediction by the listed program is labeled (+), secondary prediction is labeled α for alpha helix and β for β-strand.

3.2.2 Peptide Fibril Growth

Both P1 and P3 grew fibrils at 500 µM when incubated at 36 °C for 20 hours, as monitored by ThT fluorescence (Figure 3.5). P2, however, did not grow fibrils at 500 µM when incubated at 36 °C (Figure 3.5), even when incubated for over 72 hours (Figure 3.6). AFM performed by Dr. Shannon Hill, was used to visualize fibril formation. P1 grew curvilinear fibrils, and P3 grew circular fibrils (Figure 3.5b).

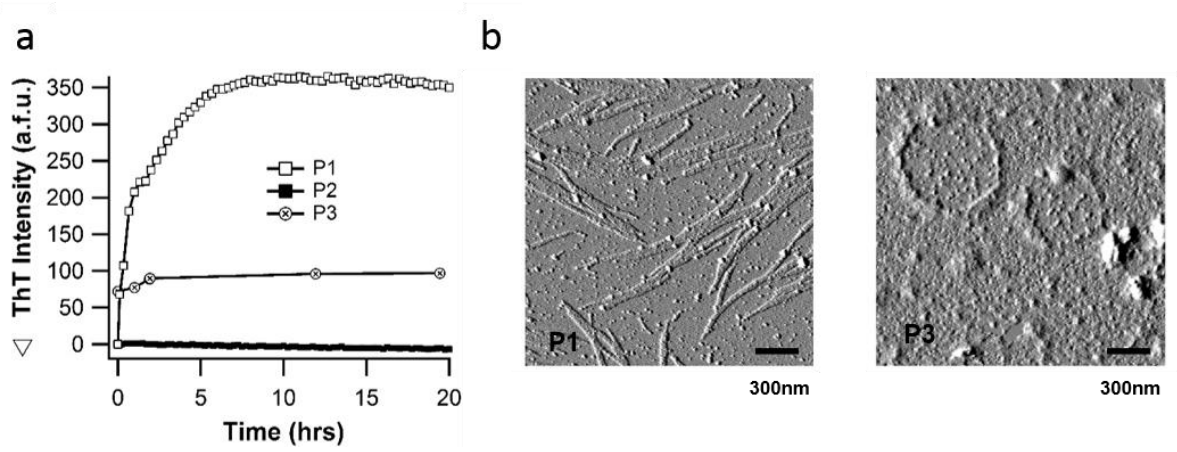

Figure 3.5 Peptide growth. a. Peptide growth monitored by ThT fluorescence. b. AFM of P1 and P3.

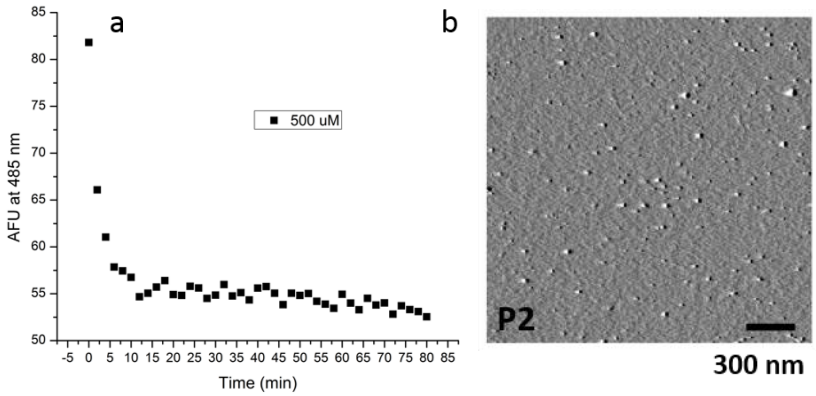

Figure 3.6 Peptide 2 growth. a. P2 growth at 36 °C monitored by ThT fluorescence. b. AFM image of P2. Performed by Dr. Shannon Hill.

3.2.3 Seeding of Full Length Myocilin Olfactomedin by Peptide Fibrils

The ability of pre-formed P1 and P3 fibrils to template fibril growth of full length myoc-OLF was examined next. Several conditions were tested for both P1 and P3. At 42 °C and pH 7.2 with salt, neither peptide was able to seed full length myoc-OLF when tested as both as-grown fibrils (data not shown) or sonicated fibrils (Figure 3.7 a and b). Conditions used previously to grow curvilinear fibrils of the OLF protein with two dimensional (2D) rocking at 37 °C and pH 7.2 with salt[125] were tested next. In this case, sonicated P1 fibrils were able to increase the rate of myoc-OLF aggregation (Figure 3.7c), but P3 fibrils had no effect (Figure 3.7d). When the temperature was increased to 40 °C, however, sonicated pre-formed fibrils of both P1 and P3 were able to increase myoc-OLF aggregation (Figure 3.7 e). Even though peptide fibrils were able to seed full length myoc-OLF aggregation under certain conditions and ThT fluorescence increased, AFM imaging revealed that the resultant fibrils did not replicate the curvilinear or circular morphology, but were more similar to disordered aggregates (Figure 3.7 f)

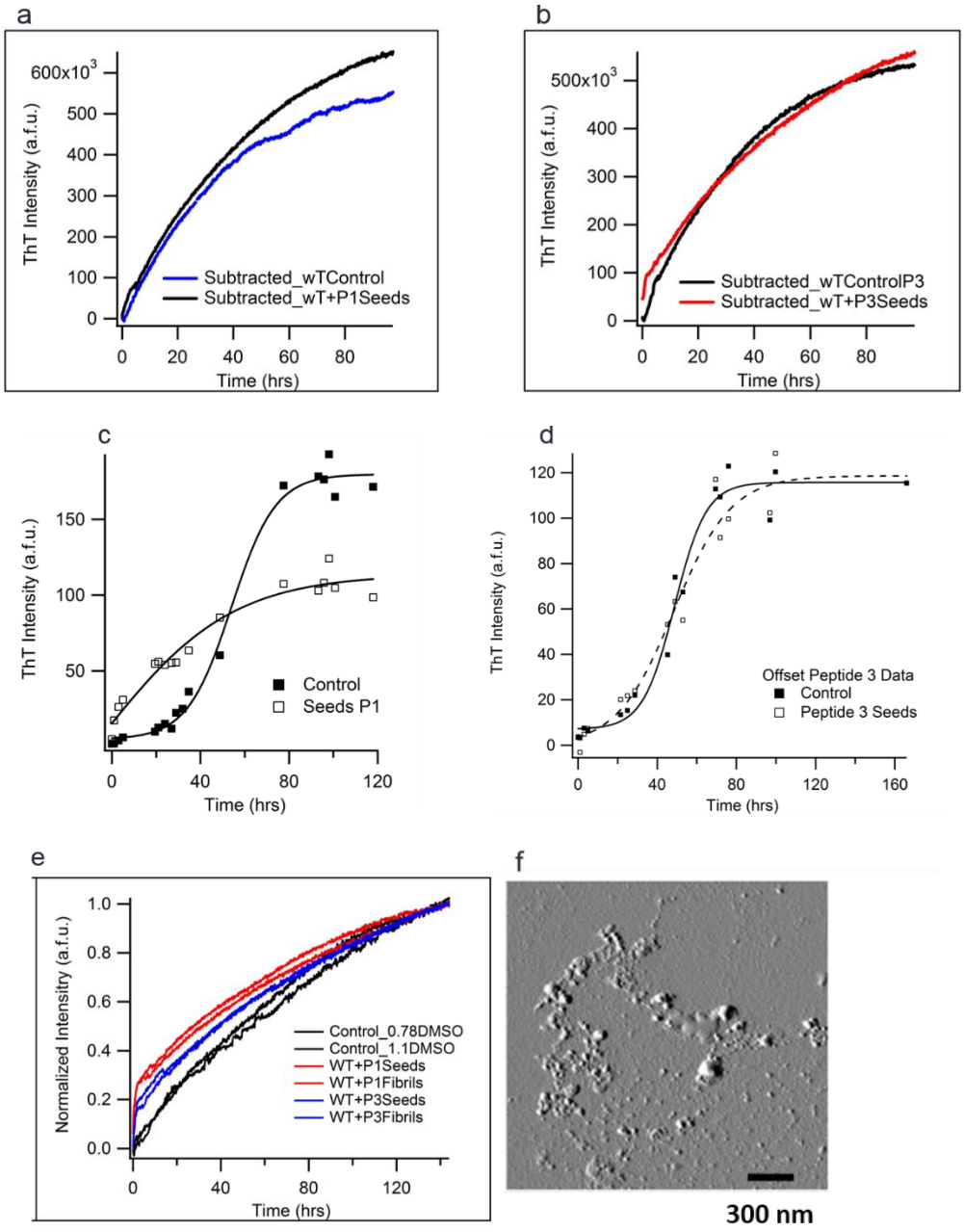

Figure 3.7 Seeding of myoc-OLF with peptide fibrils. Full length myoc-OLF seeded by P1 (a) or P3 (b) at 42 °C, pH 7.2. Full length myoc-OLF seeded by P1 (c) or P3 (d) at 37 °C, pH 7.2, with 2D rocking. e. Seeding of full length myoc-OLF by P1 (red) or P3 (blue) at 40 °C, pH 7.2. f. AFM of P3 fibrils from (e). AFM imaging by Dr. Shannon Hill.

3.3 Discussion

While the prediction servers were not in full agreement with the amyloidogenic stretches within myoc-OLF, composite scores of the program outputs allowed for the selection of three peptides with high prediction (Figure 3.4). Two of the three peptides grew ThT positive fibrils with differing morphologies. P1 grew curvilinear fibrils similar to that of myoc-OLF in the absence of salt and the disease causing mutants A427T and I499F.[125] Peptide 2 did not grow fibrils. Possibly the middle sequence of TDEAKG that has no secondary structure predicted and no amyloid propensity plays a role in preventing fibril formation for Peptide 2. P3 grew circular fibrils similar to myoc-OLF in the presence of salt and the disease causing mutant D380A.[125] The circular fibrils seen by P3 and myoc-OLF are different from the fibrils of hallmark amyloids such as Aβ. There are a few potential reasons for this odd morphology. Possibly the sequence of P3 yields a more flexible fibril core or has a kinked structure leading to the curving fibrils. The presence of an internal Cys in P3 may contribute to its unique morphology. This Cys is involved in a disulfide bond in myoc-OLF, which may alter the unfolding pathway exposing this region. P3 was also predicted to have antiparallel β-strands by the amyloid prediction sever PASTA, [127] whereas P1 was predicted to be parallel. This could possibly be responsible for the different morphologies. The similar morphologies formed by the two peptide stretches and full length myoc-OLF point to the possibility that these two sequences are responsible for amyloid formation, although other amyloidogenic peptides may exist in myocilin. Further studies to assess the potential role of these amyloid structures in myocilin glaucoma are needed.

3.4 Methods

3.4.1 Selection and Synthesis of Peptides

Peptides were selected based on output from four aggregation propensity prediciton servers. The full length sequence of myoc-OLF was submitted to Waltz[126], PASTA[127], Amyl_Pred[128] and TANGO.[129] The output from each program was normalized in order to allow for additive scoring, and the propensity for each amino acid was evaluated and stretches of 6 or more amino acids in length and predictions by two or more programs were chosen for study, yielding Peptides 1, 2, and 3. Peptides were synthesized by Celtek Peptides (Nashville, TN), with Peptides 1 and 2 at >95% purity and P3 desalted.

3.4.2 Peptide Fibrillization Assays

Peptides were diluted to 5 mg mL^{-1} stock solutions in DMSO, to remove any aggregation due to lyophilization, and stored at room temperature. Fibrils were diluted to 500 µM for fibrillization assays in 10 mM Na_2HPO_4/KH_2PO_4, 200 mM NaCl (pH 7.2), and 10 µM ThT. Peptide fibril growth at 36 °C was monitored on a Shimadzu RF-530/PC spectrofluorophotometer using a 200 µL low-head space cell (Starna 26.50LHS-Q-10/Z15). An excitation wavelength of 440 nm and an emission range of 450–600 nm (slit width 3 nm for both) was used. ThT fluorescence at 485 nm was background subtracted with buffer containing 10 µM ThT and plotted versus time for final curves.

3.4.3 Peptide Seeding Assays

Peptide seeds were formed by the same method as in the fibrillization assays. Myoc-OLF was expressed and purified as previously described (see Chapter 2 Methods). Seeding experiments, except for the 2D rocker experiments (Figure 3.7 c and d), were

conducted using a Biotek Synergy microplate reader. The 440-nm excitation filter and a 485-nm emission filter were used to monitor ThT fluorescence. 150 µL samples of 30 µM peptide seed and 30 µM myoc-OLF in 10 mM Na_2HPO_4/KH_2PO_4, 200 mM NaCl (pH 7.2), and 10 µM ThT were prepared in microcentrifuge tubes and transferred to a Grenier 96 well microplate. Plates were sealed with clear MicroAmp PCR film from Applied Biosystems. Measurements at 42 °C or 40 °C were recorded every 10 min, and ThT fluorescence at 485 nm was background subtracted with buffer containing 10 µM ThT and plotted versus time for final curves. For the 2D rocker assays, 2 mLs of 30 µM peptide seed and 30 µM myoc-OLF in 10 mM Na_2HPO_4/KH_2PO_4, and 200 mM NaCl (pH 7.2) were placed in a 5 mL centrifuge tube and rocked at 37 °C. 100 µL samples were taken at various time points over ~120 hours, 10 µM ThT was added, and their fluorescence monitored on a Shimadzu RF-530/PC spectrofluorophotometer as mentioned above.

CHAPTER 4

STRUCTURAL CHARACTERIZATION OF THE MYOCILIN OLFACTOMEDIN DOMAIN

4.1 Introduction

The OLF domain, first identified in its relation to a protein involved in olfactory chemoreception in bullfrogs more than 20 years ago,[130, 131] is recognized as a large domain family (PFAM: PF02191) comprising seven phylogenetic branches.[132] OLFs characterized to date are found largely as part of extracellular proteins[118, 131, 133-135] in multicellular organisms. They are implicated in an expansive and growing number of human disorders including a host of cancers,[98] inflammatory bowel disorder,[136] defense against infection,[137] attention deficit hyperactivity disorder[138] and childhood obesity,[139] among others.

Myocilin, the first to be associated with disease and the best studied OLF domain-containing protein, is one of the few veritable disease-modifying drug targets for glaucoma,[45] the second leading cause of blindness worldwide.[140] Nonsynonymous lesions localized almost exclusively to its OLF domain account for ~3–10% of POAG cases.[45] The leading proposed pathogenic mechanism involves a gain of toxic function, namely aggregation, in the ER of TM cells, causing eventual cell death and leading to reduced TM associated fluid outflow and accelerated onset of ocular hypertension. Although the ER chaperone machinery should be capable of efficient degradation of such mutant proteins, there appears to be an aberrant interaction between mutant myocilin and chaperones that subverts proper retrotranslocation for proteasomal degradation.[124]

Reported here are three crystal structures of myoc-OLF, revealing a new addition to the five-bladed β-propeller structural protein class. Evolutionary considerations indicate that OLF domains share a common scaffold but likely interact with distinct surface binding partners. This work offers new insight into and lays the groundwork for understanding pathogenesis and biology of this enigmatic yet important domain family.

4.2 Results

4.2.1 Crystallization of the Myocilin Olfactomedin Domain

Crystals of wild type myoc-OLF subjected to *in situ* proteolysis were grown by Katherine Turnage in a solution of 3% PEG 3000, 39% PEG 200, and 100 mM MES, pH 6.0. The crystals diffracted to 2.0 Å resolution and a complete data set at 2.3 Å resolution was collected in March of 2010 by Dr. Susan Orwig. Molecular replacement using a predicted structural homolog was unsuccessful, as were attempts with *de novo* phasing through traditional methods such as multiple isomorphous replacement (MIR) or anomalous scattering such as single wavelength anomalous diffraction (SAD) and multi-wavelength anomalous dispersion (MAD) (see Appendix). Attempts to improve crystallization included optimization of the wild type myoc-OLF crystals by variations in temperature, variations in pH of buffers and buffer composition, and variation of PEG size and concentration.

Heavy metal incorporation into wild type myoc-OLF was abandoned after higher quality crystals were grown with single nucleotide polymorphism variants (SNPs) E396D (rs61730975), K398R (rs56314834) and the double SNP E396D/K398R. Crystal conditions were optimized from the original wild type myoc-OLF condition and initial hits from the commercial screens, Emerald Biosystems Cryo I/II and the Hampton Index HT.

The K398R and E396D/K398R crystals were never improved beyond stacked plates, so further optimization focused on the E396D crystals, which were more singular, though still stacked plates. An optimized solution of 32% PEG 400, 5% PEG 3000 and 50 mM CAPSO, pH 9.5 provided reproducible singular crystals of the myoc-OLF(E396D) SNP, and a complete data set at 1.9 Å resolution was collected for myoc-OLF(E396D). Heavy metal soaks of the myoc-OLF E396D crystals were attempted in order to solve experimental phases via MIR or SAD/MAD (See Appendix A). Incorporation of Zn^{2+} and Hg^{2+} were initially promising for SAD, but was not successful due to pseudomerohedral twinning of the myoc-OLF E396D crystals, and the R_{free} value could not be improved below 0.39 at 2.7 Å resolution, even after several hundred rounds of refinement. After successful incorporation of selenomethionine (SeMet) in myoc-OLF(E396D) (see Methods) experimental phases were solved via SAD. A new crystal form without pathologies was identified using SeMet myoc-OLF(E396D), identified from the Hampton Index HT screen, and optimized crystals grew in a new condition of 19% PEG 3350, 0.1M Bis–Tris pH 6 and 0.1M magnesium formate. A complete data set at 2.09 Å resolution, with an average anomalous signal of 1.5, was used to solve experimental phases. Molecular replacement was then used to obtain the high resolution structure at 1.9 Å resolution of native myoc-OLF(E396D) (myoc-OLF(E396D)$_{I222}$) and the 2.1 Å resolution structure of wild-type myoc-OLF (Table 4.1)

Table 4.1 Crystallographic statistics.

	Myoc-OLF $(E396D)_{P21}$ (SeMet, PDB code 4WXU)	Myoc-OLF $(E396D)_{I222}$ (highest resolution, PDB code 4WXS)	Wild-type Myoc-OLF (PDB code 4WXQ)
Data collection			
Wavelength	0.979370	1.000000	1.033160
Space group	$P12_11$	I222	I222
Cell dimensions			
a, *b*, *c* (Å)	49.48, 50.56, 50.54	68.88, 86.65, 87.44	68.66, 85.82, 88.44
α,β,γ (°)	90, 97.27, 90	90, 90, 90	90, 90, 90
Resolution (Å)	19.6 - 2.09 (2.17 - 2.09)	19.79 - 1.9 (1.97 - 1.9)	19.78 - 2.15 (2.23 - 2.15)
R_{merge}	0.1174 (0.4071)	0.0884 (0.4386)	0.1025 (0.4144)
I/σI	25.23 (5.15)	15.52 (4.21)	15.54 (5.47)
Completeness (%)	97.22 (71.65)	99.98 (100.00)	99.93 (99.93)
Redundancy	13.9 (5.5)	6.2 (6.3)	7.3 (7.4)
Refinement			
Resolution (Å)	19.6 - 2.09	19.79 - 1.9	19.78 - 2.15
No. reflections	200752 (5952)	130265 (12954)	106349 (10383)
R_{work}/ R_{free}	0.1782/0.2014	0.1724 /0.2098	0.1906/0.2284
No. atoms			
Protein	2079	2072	2065
Ligand/ion	36	40	66
Water	244	304	135
B-factors			
Protein	11.10	21.10	22.90
Ligand/ion	20.10	37.10	32.50
Water	28.50	37.30	31.10
R.m.s deviations			
Bond lengths (Å)	0.005	0.005	0.005
Bond angles (°)	0.83	0.78	0.67
Ramachandran favored and additional allowed (%)	100	100	100

4.2.2 Overall Architecture of the Myocilin Olfactomedin Domain

The final models for each of the three myoc-OLF crystal structures include residues 244–502 (numbering scheme for full-length myocilin). The N-terminal 16 residues of myoc-OLF, which complete the C-terminal fragment of myocilin reported upon proteolytic cleavage in cell culture,[62] are not visible in the structures, likely because they are part of a linker between the OLF domain and N-terminal regions of full-length myocilin. The OLF domain is an ~40 Å diameter by ~30 Å high β-propeller with five blades, each composed of four antiparallel β-strands (Figure 4.1), arranged radially around a central water-filled cavity ~11 Å in diameter (Figure 4.2)

Compared with other known propellers of varying blade number,[141] the blades in OLF are notably asymmetric (see also comparison of five-bladed propellers below). Nearly half of the toroid-shaped molecule is occupied by Blades D and E. Discontinuous Strands D-18/D-18b and E-21/E-21b in the myoc-OLF(E396D) structures (Figure 4.1a) appear as single continuous strands in the wild-type myoc-OLF structure (not shown). The electron density in this region is well defined in all structures, but for clarity, in the subsequent descriptions, it is referred to the blades as labeled in Figure 4.1 for the highest resolution structure, that of myoc-OLF(E396D)$_{I222}$. Other structural features include several helical turns and a short α-helix. The α-helix resides between myoc-OLF Strands A-5 and A-6, and packs against the E–A blade interface (Figure 4.1a). Despite the lack of sequence similarity in this region (Figure 4.3) the α-helix is predicted by secondary structure prediction algorithms and is likely a general feature of the OLF domain.

Two features of OLF stabilize the propeller in a closed circular conformation. First, extensive interactions from the sequentially discontinuous two outer strands of Blade E, Strands E-1 to E-2 and E-21 (Figure 4.1c), form the propeller feature colloquially termed ‘Velcro’ or ‘molecular clasp’.[142] Second, a single disulfide bond is found at the bottom face

of the propeller (Figure 4.1b), between Cys 245 at the N-terminus of the visible structural domain prior to the start of E-1, and Cys 433, located within Loop D-15/D-16 between the internal two strands of Blade D. A similar disulfide bond is seen in four-bladed propellers.[142, 143] but not five-bladed propeller structures. The disulfide bond is likely present in most OLF domains, as the C-terminal Cys is highly conserved, and in sequence alignments (Figure 4.3) there is typically an N-terminal cysteine near the equivalent position of myoc-OLF Cys 245.

Nearly half of the residues are found within well-ordered loops above and below the propeller (Figures 4.1 and 4.4a), with minor differences among the solved structures (Figure 4.4 a). The longest loop is composed of residues 360–379 (Figure 4.1d), connects Strands B-10 and C-11, and caps the top entrance to the central cavity (Figure 4.2). Although no global changes are observed among our structures, Loop B-10/C-11 appears to serve as a gate for access to the central cavity via the positioning of the side chains of myoc-OLF Trp 373, which resides on Loop B-10/C-11, and Tyr 442, which resides on Loop D-16/D-17. In total, three states were captured that are not attributable to crystal contacts (Figure 4.4a and b). The side chain of myoc-OLF residue Trp 373 is visible in two conformations in the structures, one pointed into the central cavity and the other out towards the solvent. The ‘open’ conformation, seen in the wild-type myoc-OLF structure, has Trp 373 and Tyr 442 pointing outward towards the bulk solvent, with a polyethylene glycol (PEG) molecule bound just beneath the loop at the top of the cavity entrance. In the ‘semi open’ conformation, seen in myoc-OLF(E396D)$_{I222}$, Trp 373 is nestled inward, but Tyr 442 on the opposite loop still points toward the solvent. This shift enlarges a small surface cavity where a bound glycerol was identified in a position distinct from the aforementioned PEG. Such PEG and glycerol molecules found fortuitously in the structures reflect sites likely to promote ligand or protein–protein interactions.[144] Finally,

the ‘closed’ state is represented by myoc-OLF(E396D)$_{P21}$, whereby the position of the indole ring of Trp 373 is replaced with the phenol side chain of Tyr 442. This shifts the Tyr-containing loop into an inward conformation significantly different from that seen in the open conformations (Figure 4.4a and b).

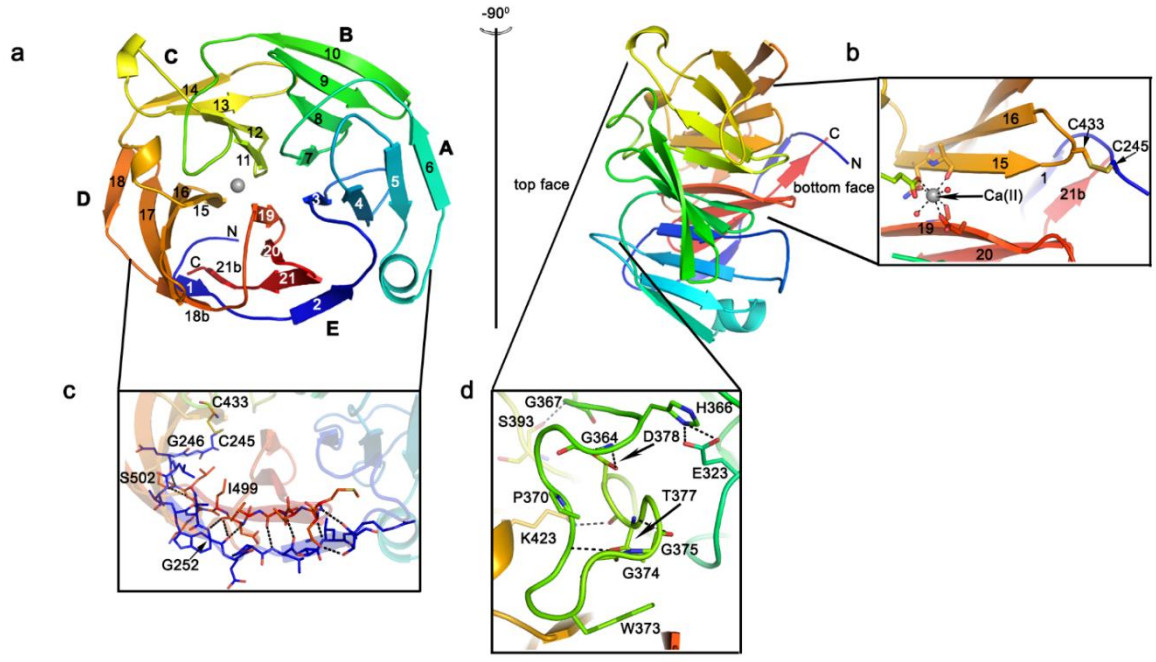

Figure 4.1 Structural features of the OLF domain. a. Top and side view of representative myoc-OLF propeller. Blades A–E with corresponding numbered strands, listed according to myoc-OLF(E396D)$_{I222}$ structure. b. Internal calcium-binding site and disulfide bond at bottom face. c. Molecular clasp region. d.Loop B-10/C-11, comprising residues 360–379. Dashed lines represent relevant stabilizing interactions. Coloring: N (blue) to C (red).

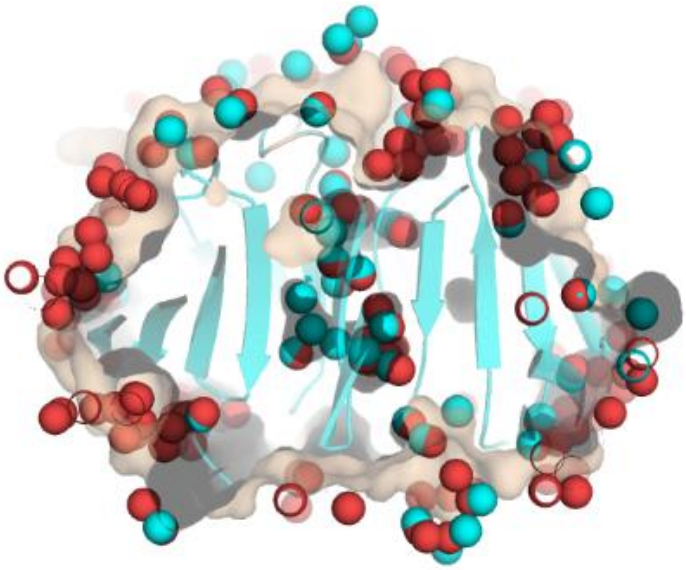

Figure 4.2 Hydrophilic cavity in myoc-OLF. Side view overlay of wild-type (cyan) and myocilin OLF(E396D) (red) structures showing overall sequestration of central cavity. Modeled water molecules are presented as balls. Central channel waters are sequestered from solvent.

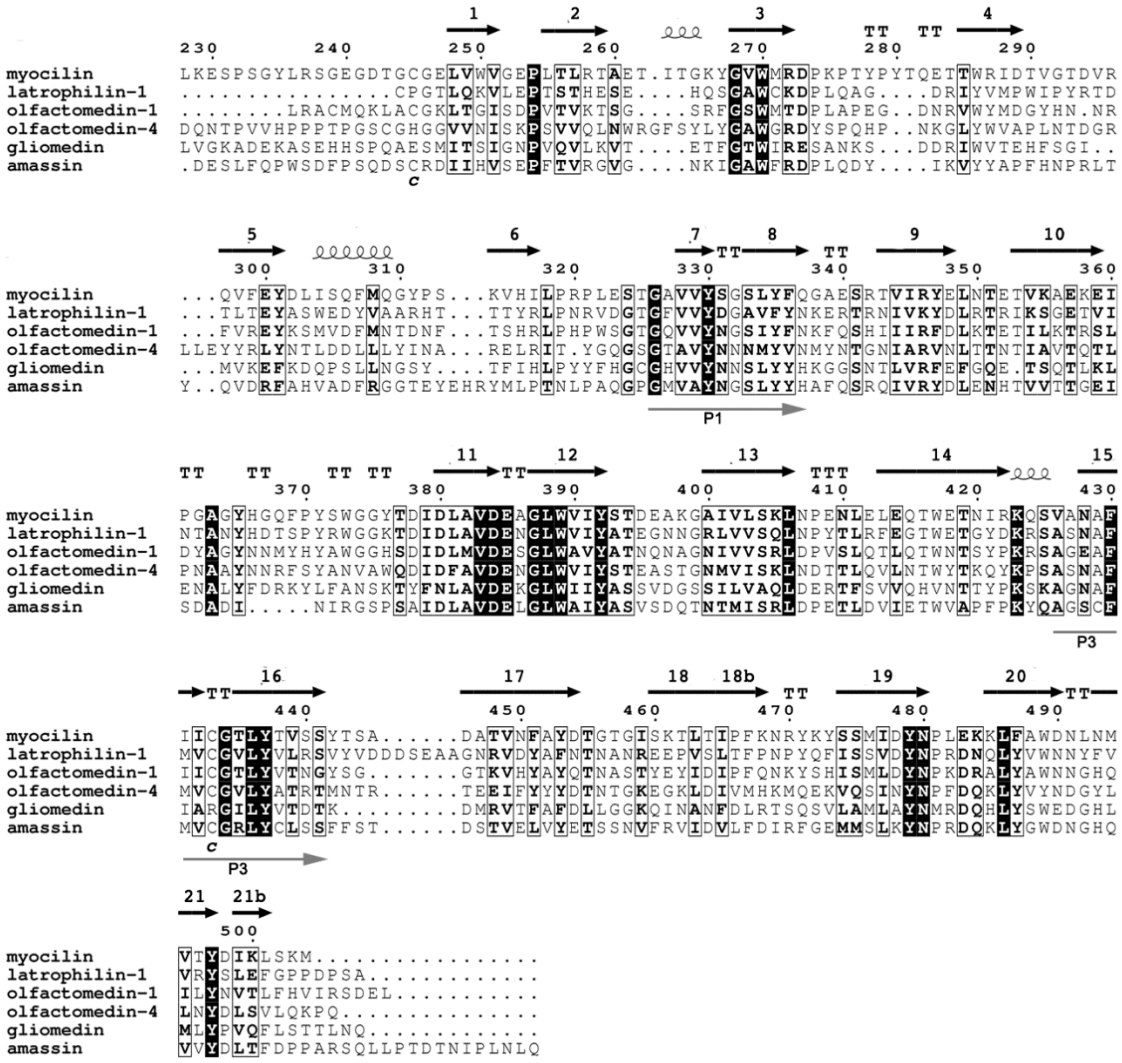

Figure 4.3 Multiple sequence alignment of representative divergent OLF superfamily members. Secondary structure and numbering scheme presented for myoc-OLF above the alignment. Annotation: arrows and helices represent β-strands and α-helices, respectively. Strands are numbered as in Figure 4.1 and in text. T: turn; boxed and bolded residues: similar; white residues with black background: identical; *c*: cysteine residues that form disulfide bond in myoc-OLF. Grey arrows indicate confirmed amyloidogenic regions.[25]

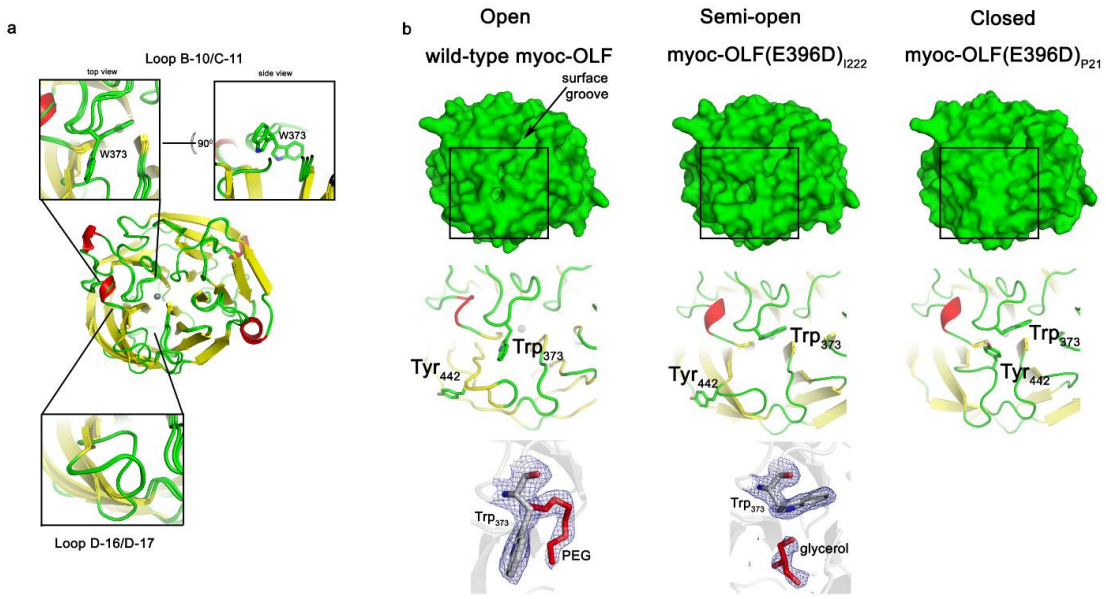

Figure 4.4 Myoc-OLF molecular surface. a. Superposition of wild-type myoc-OLF and two myoc-OLF(E396D) structures. Yellow, β-strand; red, α-helix or turn; green, loop. Zoomed regions highlight where loop structures differ b. Top face surface representation and open–closed Loop B-10/C-11 snapshots observed crystallographically. Cartoon representations of boxed region appear below each surface representation as well as observed ligands in the corresponding structure (PEG or glycerol, red) with final 2Fo − Fc electron density contoured at 1σ.

4.2.3 Central Cavity Metal Ion and Other Identified Ligand-Binding Sites

Within the central hydrophilic cavity of myoc-OLF, below the aforementioned gating loops, resides the calcium ion identified previously by metal analysis (see Chapter 2).[145] The ion was modeled into a 25σ peak in the Fo− Fc difference electron density map present after initial model building. The heptacoordinate Ca^{2+} is ligated by the side chains of Asp 380, Asn 428 and Asp 478, all in a monodentate fashion, as well as the carbonyl backbones of Ala 429 and Ile 477, and two water molecules (Figure 3a). The structure confirms Asp 380, the only previously identified Ca^{2+} ligand (see Chapter 2).[145] The ligand environment in myoc-OLF is typical for Ca^{2+},[146] but not in a documented Ca^{2+} binding motif. Consistent with the previous finding that the apo disease variant D380A is a moderately stable protein,[145] the internal position of the myoc-OLF Ca^{2+} ion appears as an ionic tether for Blades C, D and E (Figure 4.1a) to confer stability. Adjacent to the Ca^{2+} site, at a distance of ∼3.4 Å deeper into the cavity toward the bottom face, a second major Fo − Fc difference electron density peak was identified (Figure 4.5a). In our structures, based on final refined metal–ligand distances,[147] this density is modeled as a Na^{+} ion coordinated by Asp 380 and Asp 478, as well as the carbonyl backbone of Leu 381 and a water molecule (Figure 4.5a). Lastly, within the hydrophilic cavity in both closed and semi-open states of myoc-OLF(E396D), a glycerol molecule is bound, in the region between Strands A-3 and B-7 above the Ca^{2+} site (Figure 4.5b). Glycerol was not introduced during crystallization of wild-type myoc-OLF and is thus not observed in that structure.

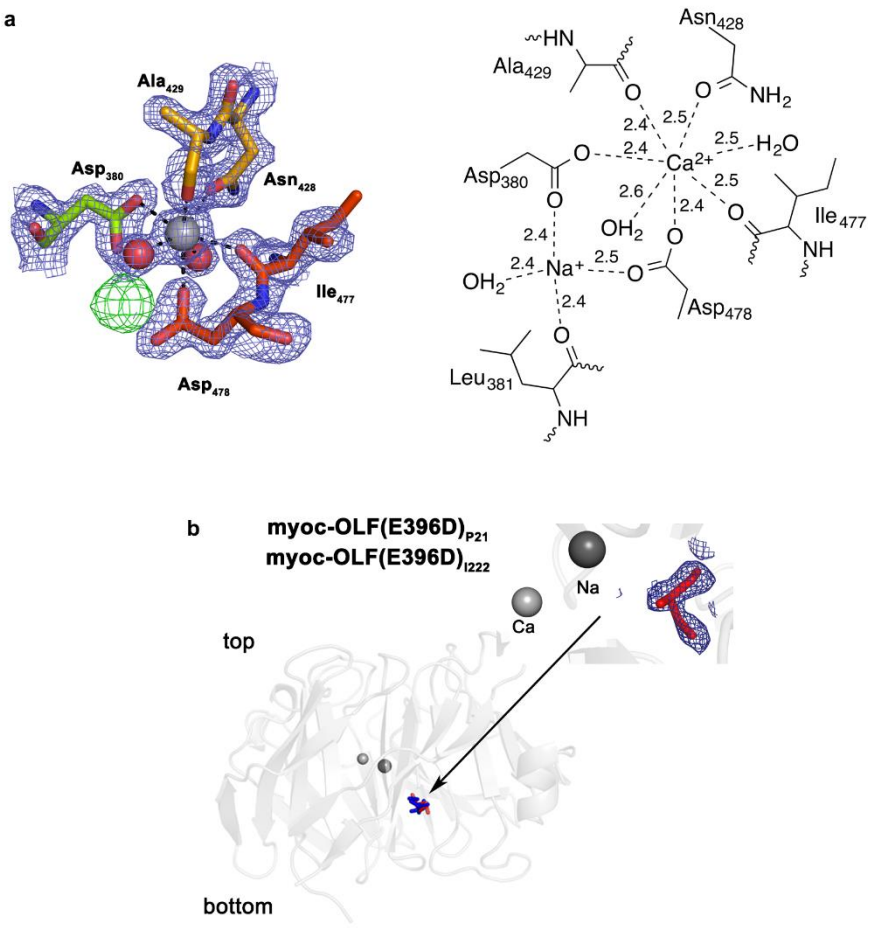

Figure 4.5 Details of the hydrophilic cavity. a. Ca2+ site and coordination details. Final 2Fo−Fc electron density (blue) is contoured at 1.5σ and difference Fo − Fc density (green) depicting crystallographic Na+ site is contoured at 3σ (see text). Distances are listed in Å. b. View of observed glycerol located in the internal hydrophilic cavity, with final 2Fo − Fc electron density for myoc-OLF(E396D)$_{I222}$ contoured at 1σ.

4.2.4 Comparison to Known Five-Bladed Beta-Propellers

Myoc-OLF is distinct from the four different proteins with known five-bladed propeller folds (Figure 4.6) with root mean squared deviations greater than 3 Å, consistent with sequence analyses that confirm OLF domains are not phylogenetically related to these propellers (less than 5-9% identity scattered throughout the sequence, not shown). Five-bladed propellers are primarily associated with glycosyl hydrolase or cyclotransferase activity; other five-bladed propellers include a human apyrase[148] and the highly symmetric founding member, tachylectin-2, which binds carbohydrates.[141] The five tachylectin-2 binding sites, located between connecting segments of one sheet and the outer two strands of a second adjacent sheet,[149] are absent in OLF (Figure 4.6a) Superposition of myoc-OLF with arabinase[150] or glutaminyl cyclase[151] reveals that the only potential catalytic residue is the unlikely myoc-OLF Ca^{2+} ligand Asp 380 (Figure 4.6 b,c). While glutaminyl cyclase harbors a Ca^{2+} binding site, this ion is not part of the glutaminyl cyclase active site;[151] arabinase has a His-ligated Cl^- ion ~3 Å away with no obvious relation to the myoc-OLF Ca^{2+} site. The surface substrate-binding cleft of arabinase is likewise not observed in OLF and clashes with Loop B-10/ C-11 (Figure 4.6b). Similar differences with apyrase are observed (Figure 4.6d). In sum, the OLF domain expands the diversity of sequentially unrelated β-propellers[141] and is a new representative template for five-bladed propellers. However, as such, the ligand binding and active sites of these five-bladed propellers do not directly shed light on the specific function for the OLF domain (see Discussion).

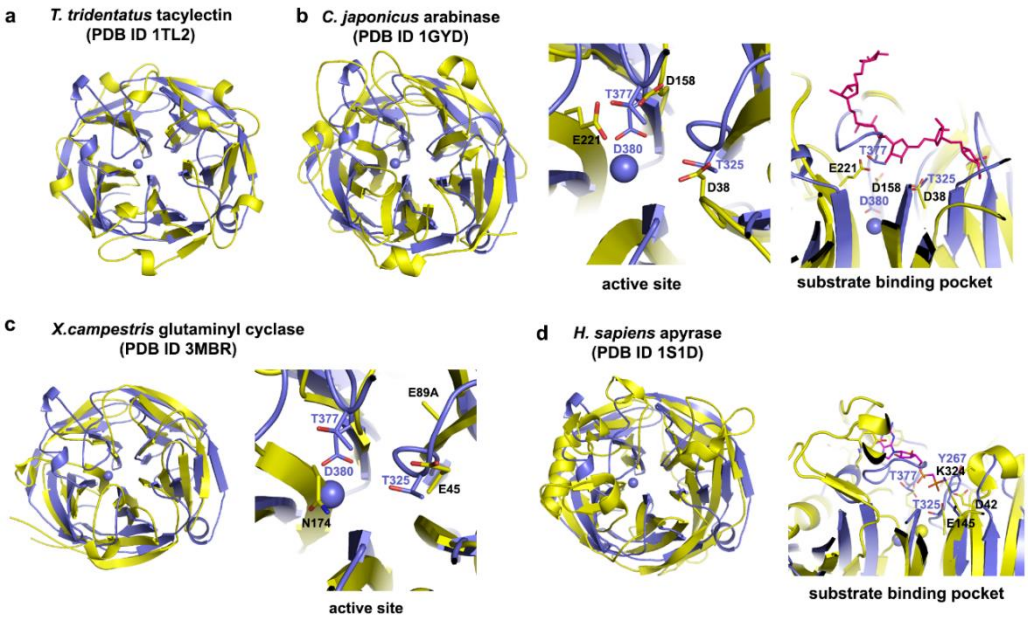

Figure 4.6 Comparison of myoc-OLF with known 5-bladed propellers. a. *T. tridentatus* tacylectin superposition with myoc-OLF. The ligand-binding motif is not present in myoc-OLF. b. *C. japonicus* arabinase; central cavity Cl^- ion, located 3 Å from the myoc-OLF Ca^{2+} ion (purple ball), is omitted for clarity. Left, cartoon representation of superposition. Middle, zoom into arabinase active site, with active site residues in stick representation, with closest myoc-OLF residues highlighted. Right, substrate (magenta) binding mode, based on the catalytically inactive mutant (PDB ID 1GYE). c. *X. campestris* glutaminyl cyclase; central cavity Ca^{2+} overlays with that of myoc-OLF, and its closest coordination residue is glutaminyl cyclase residue Glu 175. Left, cartoon representation of superposition. Right, zoom into glutaminyl cyclase active site, with closest myoc-OLF residues highlighted. d. *H. sapiens* apyrase; central cavity Ca^{2+} ion, location 4 Å from myoc-OLF Ca^{2+} ion, omitted for clarity. Left: cartoon representation for superposition. Right, substrate (magenta) binding mode of apyrase, with closest myoc-OLF residues to those stabilizing ligand in apyrase labeled and side chains presented as sticks. Purple, myoc-OLF; yellow, other 5-bladed propeller, as indicated.

4.2.5 Surface Electrostatics of Myocilin Olfactomedin

Inspection of the electrostatic surface potential (Figure 4.7a) correlates with the predicted pI ~5. The top surface of myoc-OLF contains several charged regions. There is a cluster of five positively charged surface Lys and Arg residues, in the loops connecting D-18/E-19 and E-20/E-21. A second positively charged surface on this face is in the loop that connects Strand C-14/D-15, which exposes two adjacent Lys/Arg residues at the helical turn. The main acidic patch on the top surface is formed by loops of Blade B, including those that connect to Blades A and C. At the bottom face is another acidic surface composed largely of loop residues from Blades C and D.

4.2.6 Evolutionarily Conserved and Divergent Features of Olfactomedin Domains

To gain better insight into the implications of the observed structural features of myoc-OLF on the OLF domain family as a whole, the evolutionary trace[152] of 1000 OLF domain sequences was mapped onto the OLF structure (Figure 4.7b), revealing regions of conserved and divergent features of OLF domains. Spatially clustered, highly conserved residues define regions with a high likelihood of functional significance.[152] Interestingly, the interior of OLF contains a high density of conserved residues, including Blade C and its loops, the interior strands of Blade D, the central cavity metal ion and ligand-binding sites, as well as near the site of a bound PEG at the bottom face (see Chapter 6). A major conserved feature revealed by this analysis is a cation–π interaction involving Tyr 371 within Loop B-10/C-11 and Lys 423 on Loop C-14/D-15 (Figure 4.7c). Cation–π interactions are important for molecular recognition and other biochemical processes[153] and thus may prove to be a common functional design feature of OLFs. On

the opposite end of the spectrum, the OLF surface clearly exhibits the highest degree of sequence divergence across the entire domain family (Figure 4.7b; see Discussion)

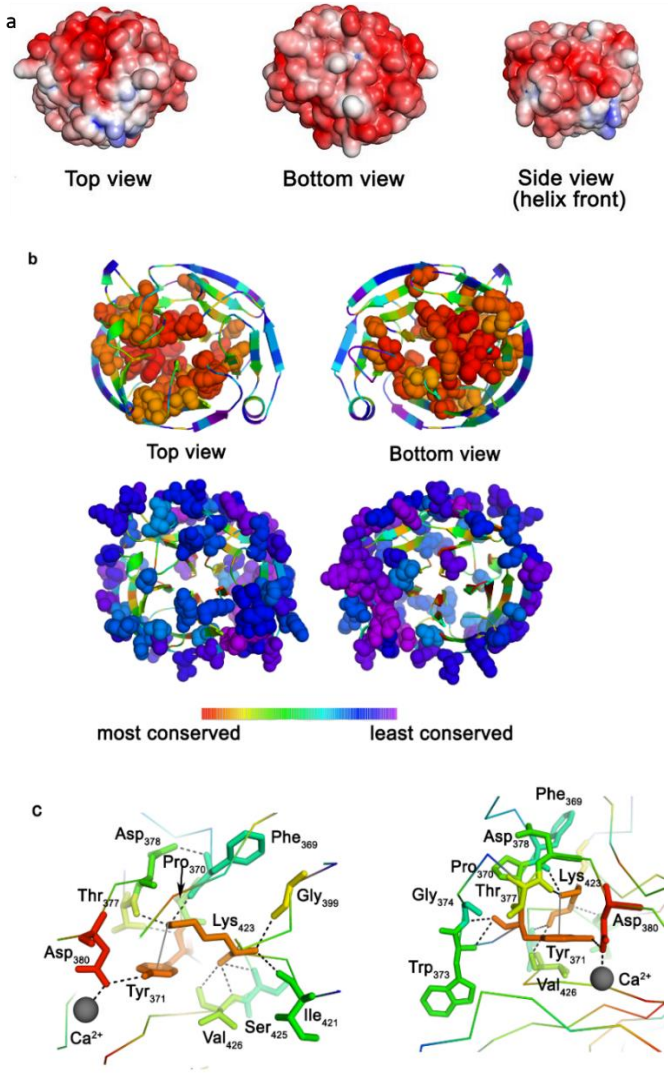

Figure 4.7 Surface electrostatics and evolutionary analysis. a. Electrostatic surfaces of myoc-OLF in three orientations. The surface potential is colored negative (red, −5 kT/e−) to positive (blue, +5 kT/e−). b. Results of evolutionary trace mapped onto myoc-OLF structure highlighting regions of highest and lowest conservation. Range of conservation depicted as rainbow.[154] c. Details of highly conserved cation–π interaction in two orientations. Dashed lines indicate stabilizing interactions spanning 2.4–3.5Å. Color range as in b.

4.3 Discussion

OLF domains are broadly involved in development and implicated in a host of human ailments, but molecular details of their biological activities and corresponding dysfunction in a variety of contexts remain active areas of investigation. Clarification of structure-(dys)function relationships continues to grow in importance as the biological reach of OLF domain-containing proteins expands in the context of the interactome.[155-158] The discovery that the OLF domain possesses a propeller fold falls in line with the existing and complex functional picture. Propellers are generally known for their ability to orchestrate multiple signaling events across diverse pathways and have a broad portfolio of interacting partners (see, for example RACK1[159]), both intracellularly and extracellularly.[160] Evolutionary trace reveals convergent and divergent features of OLFs that could not be inferred simply from sequence alignments and homology considerations. Available evidence from our structures suggests that the central cavity of the OLF domain possesses a common ligand-binding site. Access to the central cavity appears gated in myoc-OLF at the top face where exogenous small molecules appear in our structures. In support of the solvent accessibility of the internal hydrophilic core of myoc-OLF, glycerol, only introduced during cryoprotection of myoc-OLF(E396D) crystals, is seen within the central cavity even when the structure reveals the closed Loop B-10/C-11 conformation. Entrance to the internal cavity could come from the observed movement of Trp 373 or via other loop motions on the top or bottom face that have not yet been detected. Furthermore, though prior metal analysis of myoc-OLF clearly identified a single stable ion within a chelator-resistant site,[145] we cannot rule out the possibility that the crystallographic Na+ site is a labile site for Ca^{2+}. A secondary Ca^{2+} site could enable OLFs to be responsive to calcium release or other extracellular function,[161] or, in appropriate orthologues, neurological triggers. Internal sensing could propagate relevant changes to other regions

of the OLF domain to facilitate higher order protein–protein interactions or complex formation. Additional structures of OLF domains from different subfamilies will be valuable in expanding our appreciation of the structural and surface divergence of the OLF domain family. Analysis of the structures further indicates the possibility of enzymatic function for the OLF domain is remote. Known five-bladed β-propeller enzymes have their active sites at the top face of the propeller near the central cavity. While there is noted overlap of the highly conserved myoc-OLF Asp 380 residue with that of a catalytic aspartate of arabinase, it is an unlikely nucleophile. Asp 380 is bound to the Ca^{2+} and Na^{+} ions as well as provides stabilization to and proper positioning of Tyr 371 of the cation–π interaction. Removal of Asp 380 as a Ca^{2+} ligand by its replacement with disease-associated Ala yields a destabilized apo protein[48, 145] that readily aggregates in physiological buffers at 37°C.[125] The remaining active site residues associated with hydrolysis in other five-bladed propellers are Thr residues in myoc-OLF, which are not commonly associated with catalysis.[162] Major conformational changes in surface loops would be further required at the top face to create a binding pocket of sufficient size and depth to accommodate a small molecule substrate. Though it is possible to envision such motion, myoc-OLF variants that are expected to modulate the strength of the cation–π interaction are destabilized, suggesting that significant stabilization energy would need to be compensated upon such hypothetical substrate binding. The remaining loops other than B-10/C-11 are rather short and likewise may not be reconfigurable. Without candidate catalytic residues or a clear substrate-binding pocket, there is no obvious chemical reaction to propose and test.

In sum, the availability of OLF structures substantially advances our ability to interpret current data and design further experiments on function and dysfunction of the five-bladed β-propeller OLF domain. Functionally, the OLF domain appears poised for

interactions with other biological small molecules and/or binding partners. In the hydrophilic cavity, the binding entity is likely similar among OLFs. At the OLF surface, the lack of sequence conservation among subfamilies suggest dissimilar interactions and thus function. While the specific functions, ligands and binding partners for OLF domains will likely continue to be a challenging long-term experimental pursuit, atomic-detail structural knowledge will be a valuable guide to focus future studies of this family of biomedically important proteins.

4.4 Methods

4.4.1 Protein Expression and Purification

Wild-type myoc-OLF and myoc-OLF(E396D) were expressed and purified as described previously in Chapter 2. SeMet-substituted myoc-OLF(E396D) was produced by expression of the corresponding MBP-OLF(E396D) fusion protein[48] in the auxotrophic T7 Express Crystal E. coli cell line (New England Biolabs). Individual colonies were inoculated into 10 mL starter cultures, grown in Superior Broth (US Biological) overnight at 37°C, further diluted into 1 L of Superior Broth and shaken at 200 rpm at 37 °C until an OD600 = 2.0 was reached. Cells were then pelleted by centrifugation and resuspended in pre-warmed M9 minimal media supplemented with 0.4% glucose, 1 mM MgSO4, 0.1 mM CaCl2 and 0.0002% ferric ammonium citrate, but lacking methionine or SeMet. Cells were allowed to shake at 37°C for 2.5 h to deplete any remaining methionine. Fifty micrograms per milliliter of L-SeMet (Sigma) were added to the cell growth media, and the temperature was dropped to 18°C. After 1 h, protein expression was induced with 0.5 mM IPTG, and cells were allowed to grow overnight. Cells were pelleted, lysed and purified as described in Chapter 2. Overall, yield was ~0.6 mg purified SeMet-substituted myoc-OLF(E396D)/L

of Superior Broth cell culture. Incorporation of SeMet was confirmed by using a Bruker S2 Picofox instrument.

4.4.2 Crystallization, Data Collection and Structure Determination

Purified SeMet-substituted myoc-OLF(E339 6D)$_{P21}$ was concentrated to 10 mg/ml, and crystals grown by the hanging drop method by equilibration against a solution containing 19% PEG 3350, 0.1M Bis–Tris pH 6 and 0.1M magnesium formate. WT myoc-OLF (10 mg/ml, 50 mM HEPES, pH 7.5, supplemented with 0.36 mg/ml subtilisin A) grew crystals by equilibration against a reservoir solution containing 5% PEG 3000, 39% PEG 200, 100 mM MES, pH 6.0, and crystals of myoc-OLF(E396D)$_{I222}$ (10 mg/ml in 10 mM HEPES, pH 7.5) were grown from 32% PEG 400, 5% PEG 3000 and 50 mM CAPSO, pH 9.5. Crystals of myoc-OLF(E396D)$_{I222}$ and myoc-OLF(E396D)$_{P21}$ were cryo-cooled in a solution containing the respective reservoir solution supplemented with 5% glycerol and 20% PEG 200. The wild-type myoc-OLF crystals were cooled from mother liquor directly. Diffraction data were collected at the Advanced Photon Source, Argonne National Labs utilizing the The National Institute of General Medical Sciences and National Cancer Institute (GM/CA-CAT) 23-ID beamline (wild-type myoc-OLF) and Southeast Regional Collaborative Access Team (SER-CAT) 22-ID beamline (myoc-OLF(E396D)). Data were processed using XDS/XSCALE.[163] The initial structure was solved by single wavelength Se anomalous phasing using AutoSol[164] for the SeMet incorporated myoc-OLF(E396D)$_{P21}$, (mean anomalous difference in units of estimated standard deviation > 1 across all resolution bins in processed dataset, phasing figure of merit = 0.5) and the other two (wild-type myoc-OLF, high-resolution myoc-OLF(E396D)$_{I222}$) by molecular replacement using Phaser,[165] using a model generated from experimental phasing. The models were iteratively built and refined using Coot[166] and Phenix.refine.[165] PEG 200 was

modified from the PEG 400 entry from HicUP database.[167] For wild-type myoc-OLF and myoc-OLF(E396D)$_{I222}$, the pseudomerohedral twinning operator identified using Xtriage[168] was incorporated in the refinement algorithm. Structures have been deposited to the protein databank with PDB codes 4WXQ, 4WXS and 4WXU.

4.4.3 Structure Analysis

Comparison to known structures in the PDB was enabled using DALI[169], crystal contact analysis using PDBePISA,[170] metal coordination analysis conducted using FINDSITE[171] and MetalS(3),[172] and structural alignments using SSM.[173] Alignment in Figure 4.4 was prepared using PROMALS3D[174] and rendered in ESPript.[175] Electrostatic surface was calculated using PDB2PQR[176] and APBS,[177] and figures generated in PyMOL (www.pymol.org), using the default secondary structure assignment settings. Evolutionary trace was conducted using default parameters except for increasing the number of OLF sequences to 1000, results of which were mapped on to the structure for rendering in PyMOL.[154]

CHAPTER 5

STRUCTURAL IMPLICATIONS FOR GLAUCOMA PATHOGENESIS

5.1 Introduction

Evidence to date indicates that myocilin glaucoma is a protein folding disorder similar to Alzheimer's, Parkinson's and Huntington's diseases.[86] While wild-type myoc-OLF is a well-folded monomer, single glaucomatous point mutations, such as P370L, can be sufficient to impair folding to the extent that only insoluble aggregates are isolated.[48] More generally, thermal stabilities of folded, disease-associated variants, measured by the T_m, are statistically correlated with the age the associated patients were diagnosed with glaucoma.[48] Mutations in myocilin related to disease range from those of wild type like stability, such as A427T whose reported age of onset is 73 years of age, to the thermally destabilized Y437H whose earliest reported age of onset is 8 years of age.[48] At physiological temperatures, thermally destabilized myocilin mutants could accumulate a population of unfolded protein, however these unfolded proteins should be cleared by ERAD. Myocilin mutants instead induce the ER stress response, and lead to cell death.[81, 82] Likely in part due to aberrant interactions with glucose regulated protein (GRP) 94, which has been shown to interact irreversibly with mutant myocilin, to prevent ERAD clearance.[124]

The difficulty encountered by ERAD to clear mutated full-length myocilin from the ER may be due to amyloid aggregation of mutant myoc-OLF. Myoc-OLF aggregates exhibit hallmarks of amyloid,[49, 125] and appear either as long straight fibrils or an atypical

large-diameter circular species (see Chapter 3).[125] These morphologies are similar to aggregates formed by two well-conserved peptide stretches within myoc-OLF, P1 (G_{326}AVVYSGSLYFQ) and P3 (V_{426}ANAFIICGTLYTVSSY), respectively (see Chapter 3).[25] Mutant myoc-OLF more readily forms amyloid-like aggregates than wild type,[125] and mutant myocilin can also cause a decrease in wild type myocilin secretion as has been shown with other amyloidogenic proteins.[83] Consistent with a toxic gain of pathogenic function hypothesis for mutant myocilin, myocilin knockout mice, [84] and individuals with truncated myocilin, [85] do not get glaucoma. The myoc-OLF structure provides the first opportunity to understand the molecular basis of glaucoma-associated misfolding at the atomic level.

5.2 Results

5.2.1 Locations of Familial Glaucoma Variants and Identification of Misfolding Trigger Zones

Analysis of the locations of 21 myoc-OLF variants with Mendelian inheritance patterns in affected families or in selected groups of juvenile/early onset glaucoma patients, whose pathogenicity has been correlated quantitatively with thermal stability and aggregation propensity in cells and in vitro,[47, 48, 53-55] and three non-disease-associated SNPs, reveals three distinct destabilizing regions—(i) the core hydrophobic β-sheet belt including the molecular clasp, (ii) Loop B-10/C-11 and cation–π interaction, and (iii) Ca^{2+} environs (Table 5.1). The largest number of variants is found within the core β-sheet belt of the propeller (Table 5.1), particularly those variants with the lowest T_m, i.e. the most destabilized, such as W286R and I477N/S,[48, 55] where side chain alterations would disrupt hydrophobic packing and would not be well tolerated. Part of the core region, where

substitutions overall appear better tolerated, is the molecular clasp (see Chapter 4, Figure 4.1c). Such variants, namely moderate variants G246R, G252R, R272G, N480K, I499F and S502P, affect the tethering of the strands and/or alignment of the disulfide bond in this region. The C433R mutation abrogates disulfide bond formation. Interestingly, however, the effect of C433R on stability is not more drastic than that of Y437H,[48] the variant used in myocilin glaucoma mouse models,[80, 178] both are highly conserved residues within OLF domains (see Chapter 4, Figure 4.3). In the case of Tyr 437, a water-mediated side chain interaction stabilizes the region near the disulfide bond (Figure 5.1). Variants involving Loop B-10/C-11, and adjacent cation–π interaction (Table 5.1; also see Chapter 4, Figures 4.1d and 4.7c), include those that are both moderately stable and severely destabilized. The substitution K423E, which would abolish the highly conserved cation–π interaction, is one of the most thermally unstable mutations measured to date.[55] Similarly, although not assessed for stability in vitro due to the fact that it was reported just once, Y371D is associated with a teenage onset, severe glaucoma.[179] Variants of moderate stability V426F and T377M affect the cation–π interaction: Val 426 holds Lys 423 in position via main chain interactions, and the side chain of Lys 423 interacts with the main chain carbonyl of Thr 377 (see Chapter 4, Figure 4.7c). The side chain of Thr 377 also forms a hydrogen bonding interaction with the main chain of Tyr 371, which would be lost upon substitution to Met (see Chapter 4, Figure 4.7c). P370L, a severe mutant,[53, 180] is a site that appears to organize nearby residues on Loop B-10/C-11. Curiously, Pro 370 itself does not appear to participate directly in regional stabilization (see Chapter 4, Figure 4.1d and 4.7c), nor is it highly conserved among non-myocilin OLF domains (see Chapter 4, Figure 4.3). Other moderately stable variants include charge inversion mutant E323K, as well as G364V and G367R, which may be better tolerated, because these residues are surface exposed and form no native side chain interactions. Several additional

substitutions cluster near the Ca^{2+} coordination sphere (Table 5.1; also see Chapter 4, Figure 4.1b and 4.5a). These include I477N/S, whose main chain interaction with Ca^{2+} may be compromised somewhat by the disruption of the β-sheet core but not enough to abolish Ca^{2+} binding, and the moderately stable apo variant D380A,[145] which also serves to stabilize the side chain of cation–π residue Tyr 371 (see Chapter 4, Figure 4.7c). In this region is A427T, identified within a small group of family members of variable glaucoma diagnosis,[181] and a mild variant from a protein stability and aggregation standpoint.[48] The substitution likely weakens Ca^{2+} coordination to Asn 428 and Ala 429; thus, our structure supports the initial pathogenic assignment. Notably, neutral polymorphisms (http://www.ncbi.nlm.nih. gov/SNP), E352Q (rs61745146), K398R (rs56314834)[65, 182] and E396D (rs61730975), are located on surface loops, remote from the identified misfolding regions (Table 5.1). Similarly, A445V, identified in glaucoma patients,[65, 181-184] has a reported age of onset of 63 years, beyond the cutoff considered early onset.[65, 181] Like the SNPs, Ala 445 is located on a remote surface and exhibits wild-type-like stability[48] (Table 5.2). Thus, our analysis would predict that the charge neutral A445V mutation would not be prone to misfolding; additional work will be required to strengthen the argument for glaucoma causality in associated individuals, for example, via one of the alternative mechanisms proposed for myocilin-associated glaucoma including altered endocytosis,[185] mitochondrial membrane disruption[23] or apoptosis due to susceptibility toward reactive oxygen species.[186]

Table 5.1 Glaucoma associated lesions correlated with stability and myoc-OLF structure.[a]

Mutation	T_m (˚C)	Structural Location
I. Familial Mutations		
A. Hydrophobic β-sheet belt (40%)		
G246R	42.5 ± 0.2	
G252R	43.0 ± 0.2	
R272G	41.0 ± 0.3	
W286R	N/A[b]	
C433R	40.4 ± 0.4	
Y437H	40.3 ± 0.4	
I477N	37.7 ± 0.8	
I477S	39.7 ± 0.2	
N480K	42.4 ± 0.2	
I499F	42.8 ± 0.1	
S502P	41.0 ± 0.3	
B. Loop B-10/C-11 and cation-π (33%)		
E323K	44.0 ± 0.5	
G364V	45.0 ± 0.4	
G367R	42.7 ± 0.1	
P370L	N/A[c]	
T377M	44.3 ± 0.3	
K423E	34.2 ± 0.4	
V426F	41.5 ± 0.1	
C. Ca^{2+} site environs (17%)		
D380A[d]	46.6 ± 0.3	
A427T	48.3 ± 0.3	
P481L	45.5 ± 0.4	
II. Single Nucleotide Polymorphisms		
E352Q	54.8 ± 0.5[c]	Loop B-9/B-10
E396D	53.1 ± 0.1[c]	Loop C-12/C-13
K398R	53.8 ± 0.2[c]	Loop C-12/C-13

[a] Percentages in each category of (I) reflect those as listed in[44]. [b] I477N/S and N480K also belong to C. T_m values as reported in[145] except when denoted [c], which are reported in [48]. N/A indicates that no soluble recombinant protein could be isolated for T_m measurement. T_m value for wild-type myoc-OLF = 52.2 °C [48].[d] D380A also belongs to B.

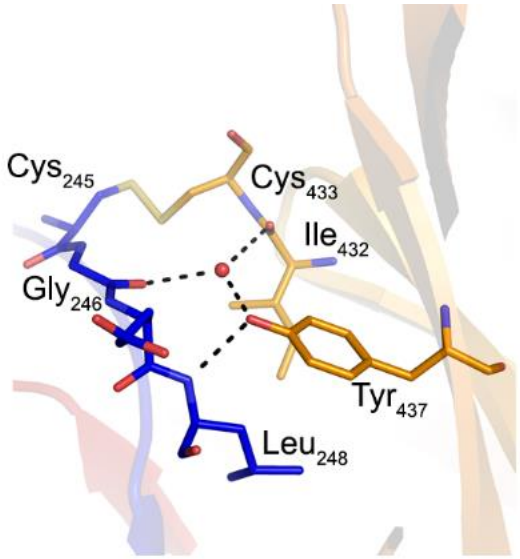

Figure 5.1 Interactions of conserved residue Tyr 437 in myoc-OLF. Y437H is the basis of the myocilin glaucoma mouse model; this substitution would weaken the hydrogen bonding network in this region.

Table 5.2 Reevaluated variants based on location in the myoc-OLF structure.

Mutation	T_m (°C)	Location	Original Assignment[1]	Proposed New Assignment
A445V	54.2 ± 0.2	Surface Loop	Disease	SNP
V329M	49.6 ± 0.4	β-sheet belt	SNP	Disease
S425P	40.8 ± 0.3	β-sheet belt	SNP	Disease
R422C	52.1 ± 0.1	Surface Loop	SNP	No Change
Y473C	54.2 ± 0.1	Surface Loop	SNP	No Change
R342K	50.4 ± 0.1	Surface Loop	Disease	SNP
T293K	52.9 ± 0.6	Surface Loop	Disease	SNP
T353I	53.1 ± 0.3	Surface Loop	Ambiguous	SNP

As listed in[44].

5.2.2 Structural Location of Peptide Stretches Responsible for Myocilin Olfactomedin Fibril Formation

The previously identified amyloidogenic peptides P1 and P3 (see Chapter 3) are found within the innermost two strands of opposing Blades B (Strands B-7 and B-8) and D (Strands D-15 and D-16) (Figure 5.2). P3 harbors structurally identified Ca^{2+}-binding residues Asn 428 and Ala 429.

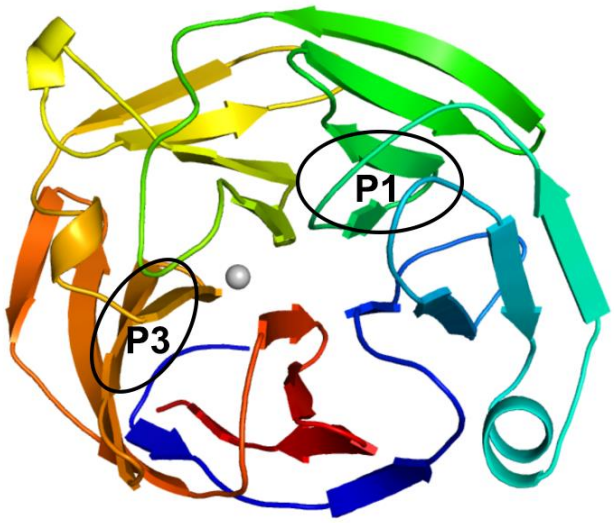

Figure 5.2 Locations of amyloid stretches as identified in myoc-OLF. P1 generates straight fibrils, and P3 generates a circular morphology (see Chapter 3).

5.2.3 Assessment of Population-Based Myocilin Olfactomedin Variants

For variants identified from large population-based genetic studies, designation as pathogenic or neutral polymorphism is complicated by the heterogeneous nature of glaucoma and age onset of disease, and is largely dependent on whether the variant is identified in control subjects or relatives of an affected person.[182] In addition, few of the many tens of variants identified through these studies have been biochemically characterized for stability and aggregation propensity. Similar to the treatment of A445V above, we applied the structural inferences from familial mutations and SNPs to discern the likelihood of pathogenicity of an additional ~60 disease-causing genetic lesions identified in such population studies but lacking confirmed protein behavior.[44] Approximately 90% of the annotated disease or SNP variants in myoc-OLF fall within the categories described above (Table 5.1). Six outliers were identified with possible alternative assignments, however. These proteins were recombinantly expressed and purified, and their T_ms measured (Table 5.2) as a direct experimental determinant of structural deformation, and thus aggregation propensity and disease liability. First, V329M has been identified several times in glaucoma patients,[65, 187, 188] but is labeled as a likely polymorphism, perhaps because Met is the residue found in the zebrafish myocilin homolog. Due to its location within a β-sheet, we predicted V329M to be a pathogenic variant. The V329M myoc-OLF variant is indeed somewhat thermally destabilized (Table 5.2), suggesting a mild pathogenic label, similar to the familial A427T variant described above, is likely more appropriate. S425P is also assigned as a neutral polymorphism variant,[182] but we posited S425P would be prone to misfolding and aggregation, and thus instead be better characterized as pathogenic. Specifically, the Pro would compromise the position of Lys 423, which is involved in the stabilizing cation–π interaction (see Chapter 4, Figure 4.7c). Indeed, the S425P myoc-OLF variant exhibits a low T_m (Table 5.2) and

mediocre yield of folded protein previously associated with the least stable familial variants, even lower than that of Y437H.[48] Variants harboring R422C and Y473C,[182, 63] both labeled as neutral polymorphisms, are further away from the aforementioned misfolding regions, but it was not clear whether a lone Cys would interfere with proper disulfide bond formation upon folding. Both the R422C and Y473C variants are thermally indistinguishable from wild type and are likely non-pathogenic, as originally suggested. Finally, labeled pathogenic mutation T293K[65, 182-184] and T353I[65, 187, 189, 190] whose pathogenicity is labeled as uncertain[44] are remote surface exposed residues unlikely to promote misfolding. In agreement with our structure based prediction, these myoc-OLF variants are well folded, have wild-type-like stability and are more likely SNPs than causative via a misfolding phenotype in glaucoma.

5.3 Discussion

We identified three structural trigger zones for misfolding—the hydrophobic inner blades, Loop B-10/C-11, and the cavity region with Ca^{2+}—where substitutions correlate directly with destabilizing variants. Mutations within the categorized regions yield a folded, but non-native structure that enhances myoc-OLF fibrillization propensity.[125] In addition, we were able to shed new light onto a variant of ambiguous pathogenicity, suggest that selected mutations thought previously to be neutral polymorphisms are likely pathogenic, and identify probable neutral polymorphisms on the surface of myoc-OLF for further interrogation. As continued genetic testing of glaucoma patients throughout the world reveals new myocilin variants, it will now be possible to integrate such structural knowledge to help evaluate whether a patient is diagnosed with glaucoma because of, or unrelated to, the myoc-OLF amino acid substitution. Moreover, the structure affords the opportunity to identify myocilin-directed molecules to stabilize pathogenic mutants against

aggregation using rational drug discovery as a new therapeutic direction. No such targeted treatment for any glaucoma subtype is currently available; indeed, a new glaucoma drug has not been approved in over a decade.[191] Knowledge gleaned through continued structure-(dys)function studies of myocilin-associated glaucoma can serve as a model to understand the molecular significance of identified mutations in other OLF-associated disorders[138, 139, 192] and adds to our comprehension of propeller protein folding more generally. For myocilin and its relation to glaucoma, our results demonstrate how the myoc-OLF structure can be used to strengthen or dispute disease causality in identified mutants, and understand physicochemical features associated with a variant prone to pathogenic misfolding. Propellers do not fall into the traditional paradigm for globular proteins, namely propellers do not possess a hydrophobic core. Thus, they are both more difficult than others to accurately predict by sequence,[193] and folding pathways are not well understood. Finally, the location of P1 and P3 (see Chapter 3) within the innermost two strands of opposing Blades B and D (Figure 5.2) explains why fibrillization does not proceed except upon accessing a partially folded state, facilitated by non-native amino acid substitutions.

5.4 Methods

5.4.1 Protein Expression, Purification and Characterization

Myoc-OLF variants T353I, R422C, S425P, Y473C, V329M and T293K were generated by site-directed mutagenesis (QuikChange Lightening kit, Stratagene), verified by DNA sequencing (MWG Operon), expressed, purified and T_ms calculated as the midpoint of unfolding using differential scanning fluorimetry, as described previously in Chapter 2. Primers used in this study not previously reported are in Table 5.3.

Table 5.3 Primers used in this study.

Myoc-OLF (T353I)	5'- CTCAGCCTTCACTATCTCGGTATTCAGCTCATATCTTAT
Myoc-OLF (R422C)	5'- GCGACTGACTGCTTACAGATGTTTGTCTCCCAG
Myoc-OLF (S425P)	5'-GAAGGCATTGGCGACTGGCTGCTTACGGATGTTTG
Myoc-OLF (Y473C)	5'- GTAGTCAATCATGCTGCTGCACTTATAGCGGTTCTTGAAT
Myoc-OLF (V329M)	5'- CTCCCCGAGTACATCACAGCACCCGTG
Myoc-OLF (T293K)	5'- CTGGCGGACATCCTTGCCAACTGTGTCGAT

CHAPTER 6

IDENTIFICATION OF LIGAND BINDING SITES IN THE MYOCILIN OLFACTOMEDIN DOMAIN

6.1 Introduction

Despite the obvious importance of OLF domains in biology and disease, their functions remain unknown. OLF domain containing proteins are expressed throughout the body, particularly in neuronal tissues, where they have roles in various processes such as neurogenesis and neural crest formation;[98] and they are implicated in a range of diseases including cancer, attention deficit disorder and glaucoma.[98] OLF domains likely have additional functions apart from their full-length counterparts, as myocilin and other OLF proteins, such as gliomedin, a protein involved in formation of the Nodes of Ranvier, and the photoreceptor protein, photomedin-1, are secreted as the OLF domain alone.[134, 194] Functional studies of OLF domains, however, have proven difficult, as most identified protein-protein interactions of OLF proteins are independent of the OLF domain, and knockout studies do not yield obvious phenotypes.[98] Indeed, myocilin is one of the few disease modifiable drug targets for glaucoma, but its native function remains unknown.[45] The myoc-OLF domain structure opens new avenues for functional studies and drug discovery for glaucoma by providing the first opportunity to identify ligands and sites for protein-protein interactions in OLF domains using rational design and *in silico* methods.

The available myoc-OLF structures, in three conformations ranging from open to closed (see Chapter 4 Figure 4.4), were analyzed for ligand binding by experimental and computational methods. We compared serendipitously-bound surface ligands from our experimental structures with predicted binding regions from two different computational

methods, solvent mapping[195] and ligand binding.[196] We further hypothesized that the identified glycerol within the well conserved hydrophilic cavity[59] (see Chapter 4) could instead bind biologically relevant metabolites common to OLF domains, such as those that regulate or signal ECM remodeling, development, or other changes in activity in neurons or AH. Specifically, we explored the possibility that the glycerol site in myoc-OLF could be a biological site for lactate and ascorbate, which have both been identified in AH.[197] More generally, lactate is thought to be an energy source for neurons,[198, 199]and ascorbate is needed for collagen[200] and elastin[201] synthesis, and may play a role in ECM remodeling by matrix metalloproteases.[202] The presented results set the stage for more detailed studies to identify common and distinct ligand binding and other interacting sites in OLF domains.

6.2 Results

6.2.1 Evaluation of Surface Ligand Binding

Surface bound PEG and glycerol molecules found fortuitously along the top and bottom face of our structures reflect sites likely to promote ligand or protein-protein interactions.[203] First, the aforementioned PEG and glycerol molecules that correlate with top surface states termed open and semi-open (see Chapter 4) bind within an area termed the “hole” in the two structures where the hole is present (Figure 6.1, labeled #1). In addition, all three OLF structures have a bound PEG molecule along the bottom surface near the conserved loop connecting strands C-11/C-12 (Figure 6.1, labeled #4). Experimental solvent mapping with acetonitrile, where glutaraldehyde cross-linked crystals were soaked in acetonitrile before being cryo-cooled for data collection, also showed consensus binding in these two regions (Figure 6.2, Table 6.1)

To expand the identification of so-called hot spots that contribute disproportionately to the binding free energy of the OLF surface,[204] we first conducted computational solvent mapping using FTMAP.[195] FTMAP uses 16 small organic molecules, similar to those often used for experimental solvent mapping (see Methods), to probe the surface of the protein for binding consensus sites. Briefly, FTMAP uses a fast Fourier transform scoring technique, based on protein surface shape and patterns of hydrophobic and polar residues, to find energetically favorable binding regions on the protein.[204-206] FTMAP predicted binding in the hole region for the semi-open myoc-OLF(E396D) structure, overlaying with an experimentally modeled glycerol (Figure 6.1, labeled #1) In all three structures, FTMAP also identified hot spots in the nearby groove region along the top surface of the protein and at the bottom surface where the PEG molecule was found (Figure 6.1, labeled #3 and #4 respectively). Next, we compared FTMAP results with those of Alignment of Pockets (APoc),[196] and the more rigorous, but unpublished, APocSim, computational algorithms by the Skolnick lab (School of Biology) that compare a query structure to the numerous structures of ligand bound proteins within the protein data bank to determine potential ligand binding pockets within the structure.[196] APoc also predicted a binding site near the top surface hole and groove region of the protein (Figure 6.3 a), while APocSim showed high consensus binding within the hole and near the top surface groove (Figure 6.3 b).

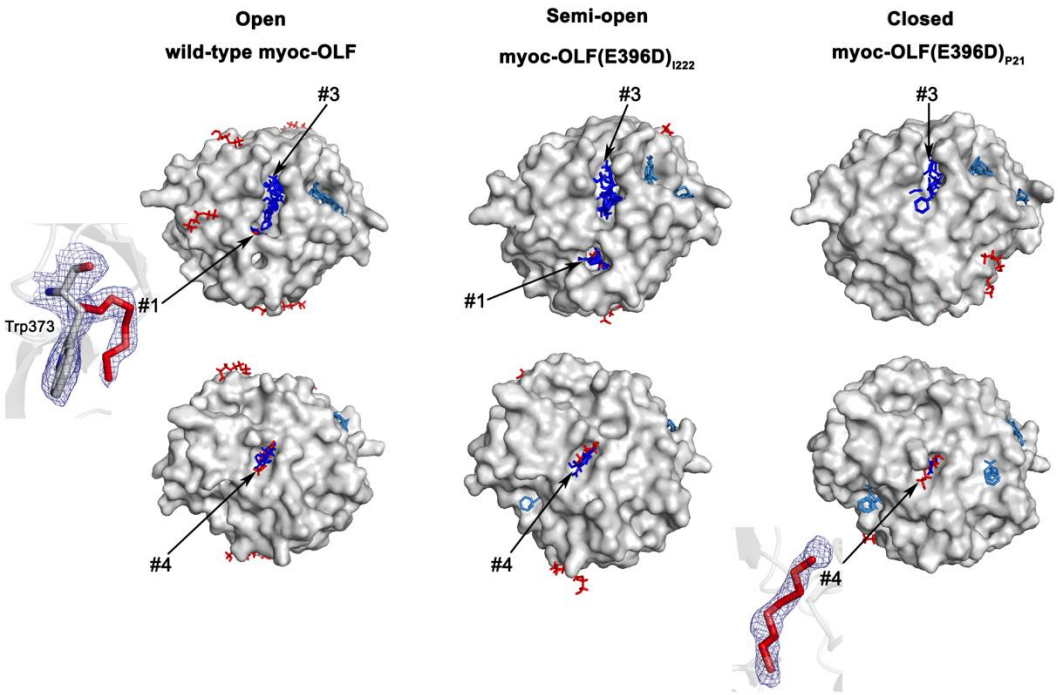

Figure 6.1 Experimental ligands and *in silico* hot spot clusters. Surface representations of three structures from the top or bottom face view highlighting experimental ligands (PEG or glycerol, red) and clusters identified by FTMAP in dark blue (labeled) and light blue (unlabeled).

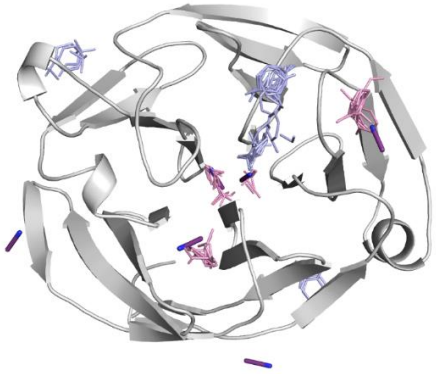

Figure 6.2 Myoc-OLF E396D structure with solvent mapped acetonitrile. Acetonitrile is shown as purple sticks, pink lines represent aligning FTMAP predicted hot spots and lavender lines represent other FTMAP predicted hot spots.

Table 6.1 Crystallographic statistics.

	Myoc-OLF with Acetonitrile
Data collection	
Wavelength	1.000000
Space group	I222
Cell dimensions	
a, *b*, *c* (Å)	68.806, 86.164, 86.985
α,β,γ (°)	90, 90, 90
Resolution (Å)	34.4 - 2.112 (2.187 - 2.112)
R_{merge}	0.1121 (0.2653)
I/σI	19.18 (4.59)
Completeness (%)	92.02 (66.04)
Redundancy	13.2 (8.1)
Refinement	
Resolution (Å)	34.4 - 2.112
No. reflections	13990 (1006)
R_{work}/ R_{free}	0.1719/0.2154
No. atoms	
Protein	2064
Ligand/ion	20
Water	132
B-factors	
Protein	11.10
Ligand/ion	20.10
Water	28.50
R.m.s deviations	
Bond lengths (Å)	0.004
Bond angles (°)	0.86
Ramachandran favored and additional allowed (%)	99.61

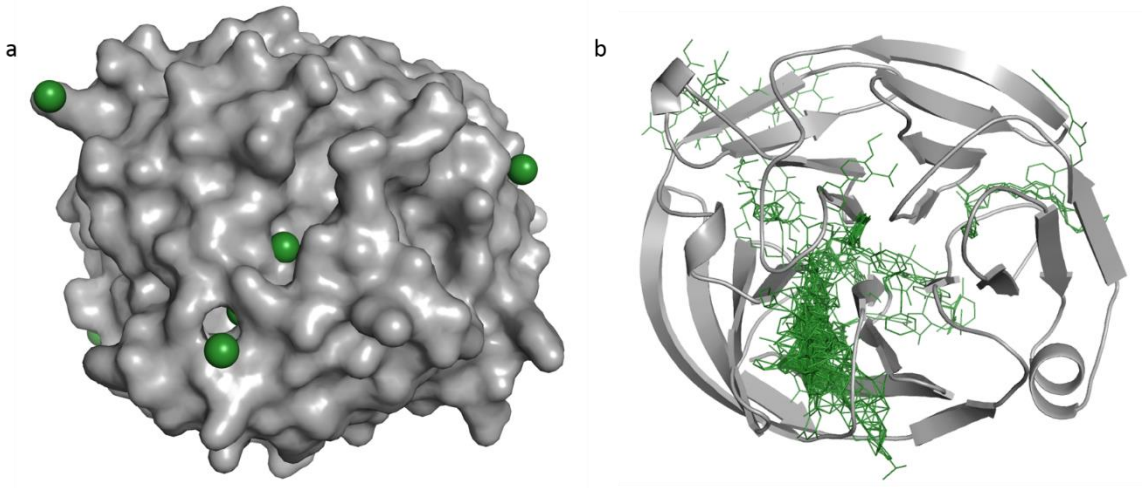

Figure 6.3 Computational ligand binging of myoc-OLF by APoc and APocSim. a. APoc predicted binding with binding spots shown as green spheres on myoc-OLF top surface representation. b. APocSim predicted binding with molecules shown as green sticks on myoc-OLF top down cartoon representation. APoc and APocSim evaluation completed by Ambrish Roy of the Skolnick Lab.

6.2.2 Evaluation of Ligand Binding within Hydrophilic Cavity

Within the hydrophilic cavity of myoc-OLF a glycerol was found in both structures where glycerol was added during cryoprotection of the crystals (see Chapter 4).[59] The relevance of this site is supported by *in silico* predictions from both FTMAP[195] and APoc[196], which identify this to be a consensus binding hot spot (Figure 6.4, Table 6.2, Figure 6.5). APoc analysis initially predicted 15 ligand locations with 9 distinct ligands. Since ligands that occupy the most similar pockets to those found within myoc-OLF by APoc may offer insight into potential ligands for the myoc-OLF domain, we evaluated three highly scored and readily available molecules fucose, mannose, and γ-butyrolactone (GBL) (Figure 6.5)

by DSF. Of these, mannose is the most stabilizing (Table 6.3). While these compounds are not likely biologically relevant, mannose and fucose are both sugars and other sugars such as glucose are found within the AH.[207] However mannose and fucose are also both osmolytes. Thus their stabilizing effects may not be due to direct binding but by the more general destabilizing of the unfolded state of the protein by manipulating properties of the buffer.[208]

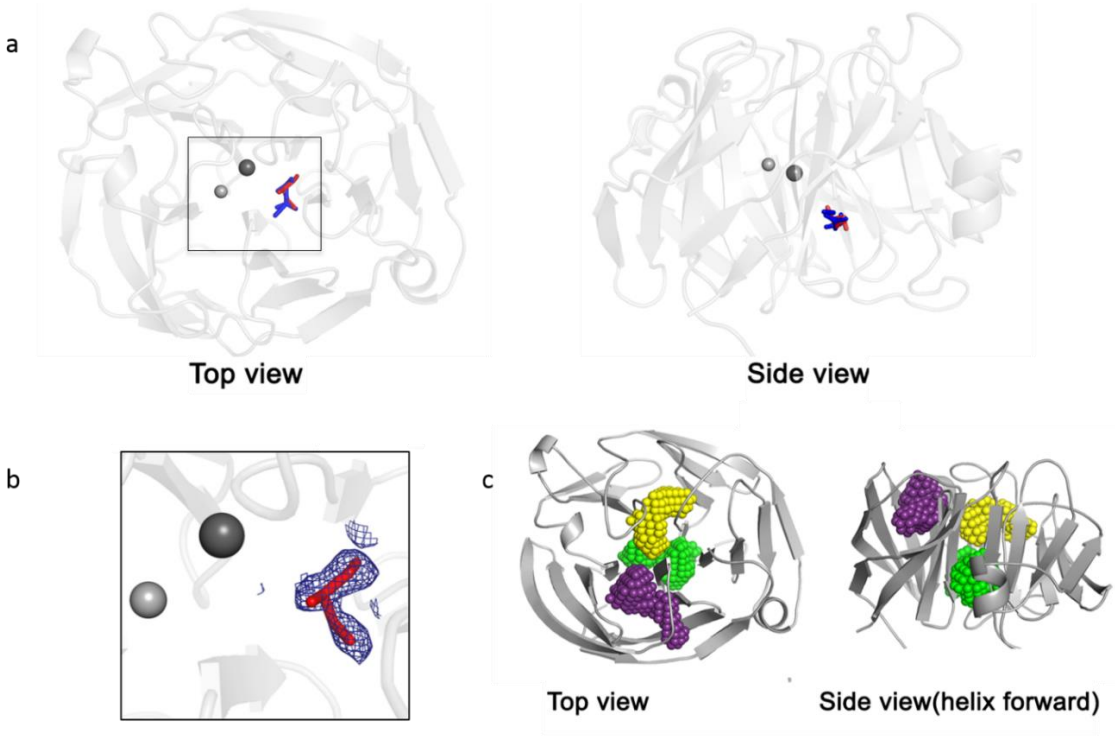

Figure 6.4 Internal ligands, *in silico* hot spot clusters, and computational pocket analysis. a. View of internal binding site identified. Glycerol is shown in red and clusters identified by FTMAP in dark blue b. Electron density of internal glycerol ($2F_o$-F_C) is contoured at 1σ. c. Comparison of pockets for myoc-OLF. Pockets are colored individually. APoc pocket analysis performed by Skolnick lab.

Table 6.2 Summary of computational analysis and observed ligand binding sites.

Cluster	FTMAP Cluster Location	Wild-type Myoc-OLF	Myoc-OLF (E396D)$_{I222}$	Myoc-OLF (E396D)$_{P2_1}$	Npoh-OLF	APoc Pocket
1	Top face, surface cavity near loops B-10/C-11 and loop D-16/D-17	X PEG	X Glycerol	--	--	Purple
2	Hydrophilic cavity	X	X Glycerol	X Glycerol	--	Green
3	Top face, surface groove near loops B-10/C-11 and loop A-4/A-5	X	X	X	X	--
4	Bottom face, loop C-11/C-12	X PEG	X PEG	X PEG	X	--

FTMAP cluster is indicated by X. Overlapping experimental ligand, if observed, is listed below. APoc color as depicted in Figure 6.4.

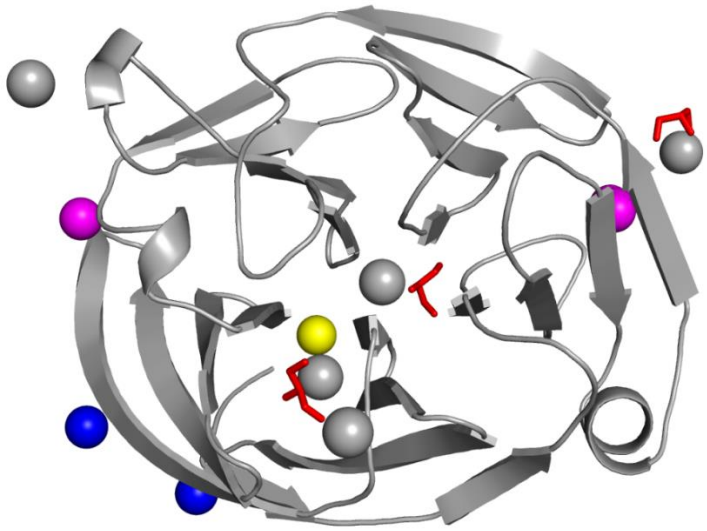

Figure 6.5 APoc hits. Myoc-OLF structure with location of APoc hits as spheres. Glycerols from OLF structure as red sticks, fucose in magenta, mannose in blue and GBL in yellow.

Table 6.3 ΔTm of myoc-OLF with APoc ligands.

Additive	100mM	500mM
Fucose	0.0 °C	1.3 °C
Mannose	0.6 °C	3.5 °C
GBL	1.1 °C	-18.8 °C

6.2.3 Evaluation of Predicted Biological Ligands

Next, the ability of select biologically relevant identified molecules to bind myoc-OLF was evaluated computationally using AutoDock Vina.[209] The best docked location for citrate and glutamate coincide with the previously identified surface glycerol binding site (Figure 6.1, Figure 6.6, Table 6.4) and acetate, lactate and glycerol were within the internal glycerol site (Figure 6.2, Figure 6.6, Table 6.4). When binding was localized to the internal cavity, ascorbate, glutamate and lactate all exhibited more favorable calculated binding energies than glycerol (Table 6.5). In support of the possibility that this internal site is biological, lactate, acetate and glutamate thermally stabilize myoc-OLF (Figure 6.7, Table 6.6).

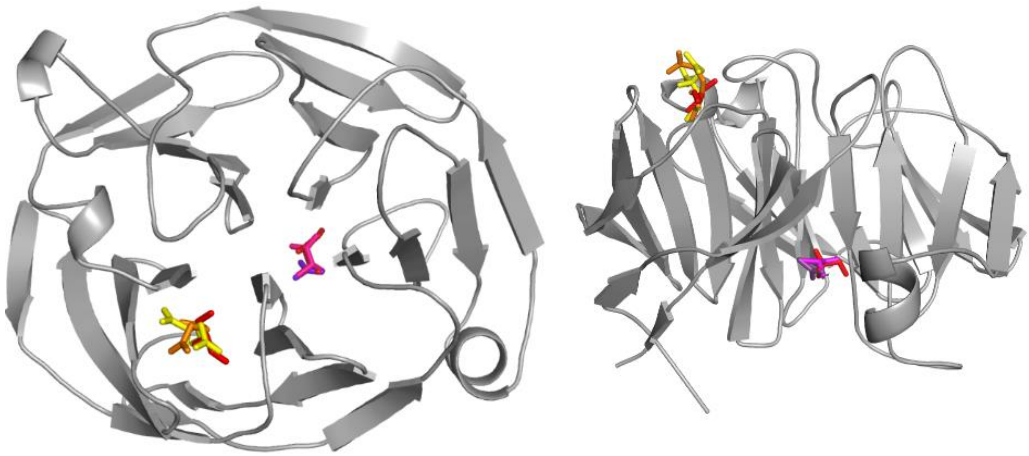

Figure 6.6 AutoDock Vina docking of biological molecules to myoc-OLF. Top down and side views. Glycerols are depicted in red, acetate in purple, glutamate in orange, lactate in pink and citrate in yellow.

Table 6.4 Calculated binding energies of ligands from AutoDock Vina

Ligand	Predicted Binding Energy (kcal/mol)
Internal Glycerol Site	
Acetate	-3.4
Glycerol	-4.4
Lactate	-4.6
Surface Glycerol Site	
Citrate	-5.3
Glutamate	-4.6
Other	
Ascorbate	-5.4
Bicarbonate	-3.6
Retanoic Acid	-6.7

Table 6.5 Calculated binding energies of ligands constrained to internal glycerol site

Ligand	Predicted Binding Energy (kcal/mol)
Ascorbate	-5.5
Glutamate	-4.9
Lactate	-4.6
Glycerol	-4.4
Citrate	-4.2
Acetate	-3.4
Bicarbonate	-3.3
Retanoic Acid	52.5

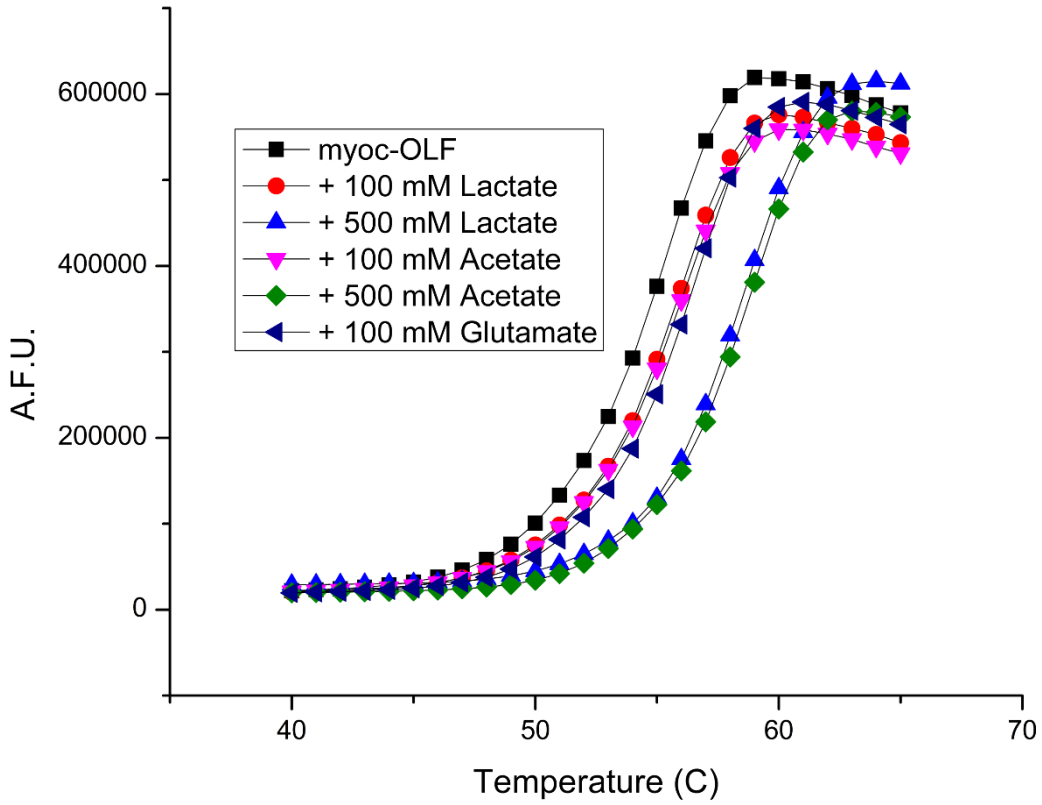

Figure 6.7 Thermal stability of myoc-OLF with ligands. DSF of myoc-OLF with ligands from docking experiments.

Table 6.6 ΔTm of myoc-OLF with predicted biological ligands.

Additive	100mM	500mM
Lactate	0.78 °C	4.00 °C
Acetate	0.84 °C	3.99 °C
Glutamate	1.43 °C	not tested

6.3 Discussion

The crystal structures of myoc-OLF reveal possible ligand binding and protein interaction regions of the OLF domain. The combination of computational algorithms FTMAP and APoc and corresponding experimental validation indicate both common and unique binding hot spots for each of the crystallized myoc-OLF states. Regions of particular interest include the top surface groove of the protein and the nearby hole found in the open and semi-open conformations and the internal glycerol binding site. These experimentally and computationally identified regions may represent regions for functional ligand binding or protein-protein interactions. Here we showed that glutatmate, lactate, and ascorbate are predicted to exhibit favorable binding energies within the experimentally-identified internal site. Two of these ligands, along with other computationally predicted sugar-based ligands from APoc analysis, thermally stabilize myoc-OLF. The ligands found or predicted to occupy these binding spots may shed light on the functional role of myocilin, and OLF domains in general. They may also provide scaffolds for molecules with potential to protect myoc-OLF from aggregation and thus mitigate the pathogenic outcome of myocilin glaucoma. Further investigations utilizing ligands such as glutamate and lactate, which are present in both AH and in neuronal tissue ECM,[210-213] may offer insight into the biological function of myoc-OLF or OLF domains in general.

6.4 Methods

6.4.1 Computational Ligand Binding

ApoC[196] calculations were completed on the myoc-OLF crystal structure by Ambrish Roy in the Skolnick lab at Georgia Tech. The myoc-OLF, myoc-OLF(E396D) and SeMet myoc-OLF(E396D) structures were submitted to the FTMAP[205] server for evaluation of ligand binding for each structure. For docking with AutoDock Vina, the molecules listed in Table 6.4, which were chosen based on their similarity to glycerol and their occurrence in the AH or the ECM in general, were allowed to bind either the entire myoc-OLF structure or a region comprising of only the internal binding site. Input files were generated via AutoDock tools, and along with AutoDock calculations, were completed using default screening parameters in PyRx.[214]

6.4.2 Protein Expression, Purification and Thermal Stability Assay

Myoc-OLF and variants used for crystallization and thermal stability were expressed and purified as discussed previously in Chapters 2 and 4. Changes in thermal stability were assessed by DSF,[105] as modified by us previously for MBP-OLF[55, 64] (also see Chapter 2).

6.4.3 Crystal Soaks, Data Collection and Refinement

For solvent mapped crystals, crystals of myoc-OLF(E396D) (10 mg/ml in 10 mM HEPES, pH 7.5) were grown from 32% PEG 400, 5% PEG 3000 and 50 mM CAPSO, pH 9.5. Crystals were cross-linked by addition of 2 µLs of 25% glutaraldehyde into the crystal drop 30 minutes prior to soaking in solvent as per an established protocol.[215] Crystals were harvested and soaked in a solution of 40% acetonitrile and cryoprotectant solution, which is reservoir solution supplemented with 20% glycerol and 5% Peg 200. Crystals were then

cryo-cooled for data collection without additional cryo-protectant. Data were collected at the SER-CAT ID-22 Beamline as reported in Chapter 4. Data were integrated, scaled and merged using HKL2000.[216] The structure was solved by molecular replacement using Phenix Phaser[165] and the model was refined using Phenix Refine[168] and Coot,[166] as reported in Chapter 4. Data collection and refinement statistics were calculated in Phenix and are listed in Table 6.1.

APPENDIX A

UNSUCCESSFUL TECHNIQUES FOR SOLVING EXPERIMENTAL PHASES AND UNSUCCESSFUL EXPERIEMENTAL LIGAND BINDING OF THE MYOCILIN OLFACTOMEDIN DOMAIN

A.1 Introduction

This appendix outlines many of the techniques employed over the two year attempt to solve the phases of myoc-OLF experimentally after the initial crystallization and data collection of wild type myoc-OLF by Dr. Susan Orwig. The crystallization of several variants of myoc-OLF were attempted in order to optimize the diffraction quality of the crystals along with various techniques for solving experimental phases for myoc-OLF and variants. Also outlined here are the unsuccessful attempts for experimental ligand binding via crystal soaks and cocrystallization that were not highlighted in the previous chapters.

A.2 Methods, Results and Conclusions

A.2.1 Crystallization of Myocilin Olfactomedin Variants

After the initial success of wild type myoc-OLF crystallization and data collection, attempts were made to repeat the crystals. However these attempts did not prove successful even with varying parameters such as temperature, PEG size and concentration, buffer pH and components, and drop size, among other things. Other variants of myoc-OLF were attempted in the hopes of finding a better crystal form and/or

repeatable crystals. These variants are summed in Table A.1. All proteins were expressed and purified as previously reported in Chapter 2. Crystallization of purified protein began with the original myoc-OLF condition along with sparse matrix screens such as the Hampton HT Index screen and the Wizard Cryo I/II screens. Glycerol improved K398R crystal size, possibly by slowing their formation. Seeding was attempted with both K398R and E396D crystals but only decreased crystal size and increased the number of crystals in the well. Other attempts to slow crystallization and improve crystal form included E396D crystallization under oil and increasing reservoir to drop ratio, with no obvious improvement in crystal form when monitored under the visual microscope.

Table A.1 Myoc-OLF variants for crystallization

Variant	Reasoning	Outcome
Myoc-OLF wild type	Repeat original crystal	No crystals
K398R SNP	Improve crystal form	Stacked plates with smeary diffraction
E396D SNP	Improve crystal form	Singular stacked plated (see Chapter 4)
E396D / K398R double mutant	Improve crystal form	Stacked plates
D380A/E396D	Apo form due to D380A mutation	Unreproducible Micro-crystals
E323K/E396D	E323K mutation should affect long loop stability	Not enough monomer purified for crystallization
MBP-OLF wild type	MBP should aid in crystallization	No crystals
MBP-OLF D380A mutant	MBP should aid in crystallization	No crystals

A.2.2 Unsuccessful Techniques for Solving Experimental Phases

After the successful crystallization of the K398R and E396D myoc-OLF SNP variants, several attempts at heavy metal incorporation of crystals, or of the protein before crystallization, were attempted. These experiments are summed below.

A.2.2.1 Heavy Metal Soaks for Isomorphous Replacement or Anomalous Phasing

For heavy metal soaks, times attempted varied from 10 minutes to approximately 72 hours. Hydrated salts of heavy metals were dissolved in water at concentrations from 0.2 - 1 mM and 0.2 µLs of stock solution was added directly to the crystal drop. Some E396D crystals had β-mercaptoethanol (BME) added before the heavy metal in an attempt to improve incorporation of heavy metals into the protein crystal, soaks were done on these with and without addition of BME. Crystal soaks are summed in Table A.2. Both zinc and mercury metal ions were successfully incorporated and data sets were collected at their respective anomalous wavelength, however, the solving of phases with these metals was unsuccessful due to low anomalous signal and crystal pathologies including multiple lattices and pseudomerohedral twinning.

Table A.2 Heavy metal crystal soaks.

Metal (Salt)	Myoc-OLF Variant	Attempted with BME
Pt ($PtCl_4K_2$)	E396D and K398R	yes
Hg ($HgCl_2$)	K398R and E396D	yes
Zn ($ZnCl_2$)	K398R and E396D	yes
Tb ($TbCl_3$)	K398R and E396D	no
Sm ($Sm(CH_3CO_2)_3$)	K398R and E396D	no
U ($UO_2(CH_3CO_2)_2$)	E396D	no
Pb ($Pb(CH_3CO_2)_2$)	E396D	no
Mn ($MnCl_2$)	E396D	no
Cu ($CuCl_2$)	E396D	no
I (KI)	K398R	no

A.2.2.2 Iodophenylalanine Incorporation

In collaboration with the Mehl lab at Oregon State University, we attempted to incorporate, via molecular biology, the non-natural amino acid iodo-phenylalanine (Iodo-Phe). Very briefly the Mehl lab has developed a method of using engineered tRNAs evolved to recognize a TAG stop codon to incorporate the Iodo-Phe into chosen former Tyr sites within the protein sequence. This procedure requires the use of cell lines that do not express rare codons and the incorporation of our gene into a plasmid without MBP fusion, which has been proven necessary for folding and solubility of myoc-OLF.[64] A TAG site was successfully incorporated into K398R via site directed mutagenesis, however the changes to vector and cell type severely inhibited the expression of the myoc-OLF before the attempted Iodo-Phe incorporation. Since Iodo-Phe incorporation typically significantly reduced expression with other proteins tested in the Mehl lab, the likelihood of producing crystallizable quantities of the protein was determined to be unlikely and the project was abandoned.

A.2.2.3 Incorporating Terbium into Calcium Binding Site

Since myoc-OLF was determined to have an internal calcium binding site (see Chapter 2), the potential for heavy metal incorporation into this site could be exploited for solving the experimental phases of myoc-OLF. Terbium has long been used as a probe for calcium binding,[217] and its incorporation could be useful for both solving phases via isomorphous replacement or anomalous scattering with an accessible L-III edge of 1.65 Å. Additionally Tb^{3+} incorporation could be monitored due to the fluorescent properties of Tb^{3+}. Incorporation of Tb^{3+} was attempted at both the growth stage, similar to SeMet, and after purification. During growth $TbCl_3$ was added 30 minutes before induction with IPTG to cells that had reached the desired optical density in superior broth. Other than $TbCl_3$ addition, cell growth was as previously reported in Chapter 2. The addition of $TbCl_3$ was potentially toxic to the cells or prevented induction as no purified myoc-OLF monomer was able to be isolated.

Another method for incorporating Tb^{3+} into myoc-OLF was through partial thermal unfolding of myoc-OLF in the presence of high $TbCl_3$ concentration to compete for Ca^{2+} binding. Ca^{2+} could not be successfully removed by chelation with EDTA during purification conditions, or by high concentrations of EDTA at the slightly destabilizing pH of 4.6, a condition with similar secondary and tertiary spectra to apo myoc-OLF(D380A) (see Chapter 2).[145] Partial thermal unfolding could expose the Ca^{2+} binding site enough that Tb^{3+} could be exchanged. 25 µM myoc-OLF(K398R) was incubated for one hour at various temperatures from 40 - 60 °C in the presence of 1 mM and 10 mM $TbCl_3$ in 10 mM Hepes pH 7.5 buffer with no salt. After incubation, samples were dialyzed using a dialysis cassette overnight in 2 L Hepes pH 7.5 buffer with no salt at 4 °C with slow mixing. Samples were then tested for Tb^{3+} incorporation by unfolding protein with 2 M guanidinium hydrochloride in the presence of dipicolinic acid, which fluoresces in the presence of

Tb^{3+}.[218] The sample at 47.7 °C showed an increase in Tb^{3+} upon unfolding (Figure A.1). While this was repeatable at 25 µM protein, scaling up to levels of protein necessary for crystallization yielded mostly aggregated protein after dialysis. Therefore this method is only useful for small scale incorporation and not feasible for Tb^{3+} incorporation for crystallization. Co-crystal trays of K398R and Tb^{3+} were also attempted, but did not yield viable crystals.

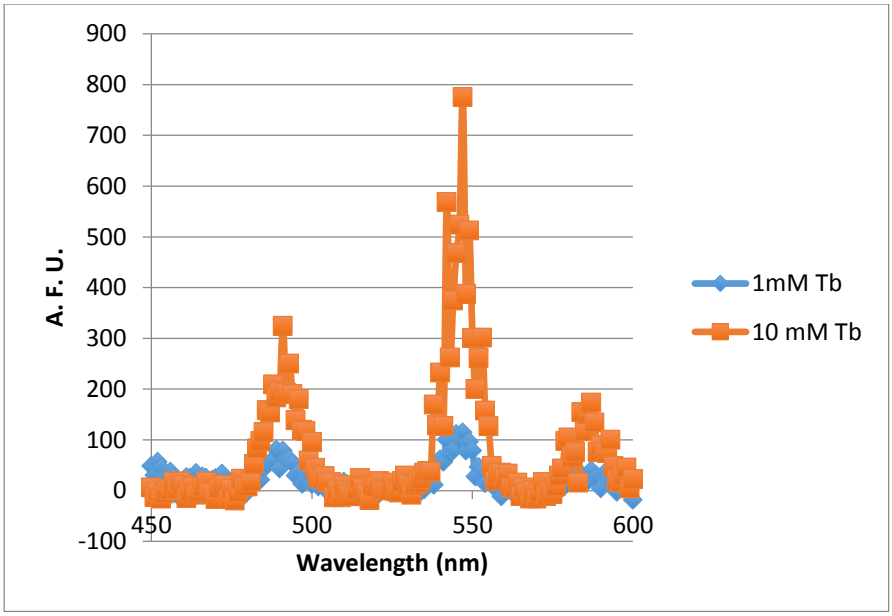

Figure A.1 Difference emission spectra of Terbium incorporated myoc-OLF. The difference fluorescence emission spectra of unfolded minus folded myoc-OLF(K398R) incubated with 1 mM (blue) or 10 mM (orange) $TbCl_3$ in the presence of dipicolinic acid with excitation at 270 nm.

A.2.3 Crystal Soaks of Stabilizing Compounds

In order to further evaluate potential ligands for myocilin OLF from this study and previous studies,[117] co-crystal trays and soaks with ligands and myoc-OLF(E396D) were attempted. Ligand soaks are summarized in Table A.3. Co-crystallization attempts are summarized in Table A.4. All soaks were sent for data collection at the APS ID-22 Beamline as discussed in Chapter 4, however none of the soaked ligands were evident in the electon density of the solved sturctures.

Table A.3 Crystal soaks of potential ligands.

Potential Ligand	Data Collected	Structure Solved
Ascorbate	yes	No
Acetate	yes	No
Glutamate	yes	Yes- No Ligand
Lactate	yes	Yes- No Ligand
Mannose	yes	Yes- No Ligand
Fucose	yes	Yes- No Ligand
Uridine	yes	Yes- No Ligand
Uracil	yes	Yes- No Ligand
UTP	yes	Yes- No Ligand
Drug A1[117]	yes	No
Drug G5[117]	yes	Yes- No Ligand

Table A.4 Cocrystallization attempts.

Co-Crystal Ligand	Crystals Grown	Data Collected	Structure Solved
Mannose	Yes	Yes	Yes - No ligand
Naringenin	No	NA	NA
Lactate	No	NA	NA
Acetate	No	NA	NA
Glutamate	No	NA	NA

A.2.4 Structure of the Reduced Olfactomedin Domain of Myocilin

The structure of reduced myoc-OLF was captured crystallographically by soaking myoc-OLF(E396D) crystals, grown in the SeMet myoc-OLF(E396D) crystal condition, in BME. Purified myoc-OLF(E396D) was concentrated to 10 mg/ml, and crystals grown by the hanging drop method by equilibration against a solution containing 19% PEG 3350, 0.1M Bis–Tris pH 6 and 0.1M magnesium formate. Two µLs of BME was added directly to the drop with crystals. Crystals were harvested into a cryoprotectant of reservoir solution supplemented with 15% glycerol and 5% Peg 200 before being cryo-cooled for data collection. There were no structural changes of the surface or internal binding regions compared to the SeMet myoc-OLF(E396D) structure (Figure 6.7a). However, two N-terminal residues Gly 244 and Cys 245, which under non-reducing conditions is involved in a disulfide bond with Cys 433, could no longer be seen in the electron density. (Figure 6.7b).

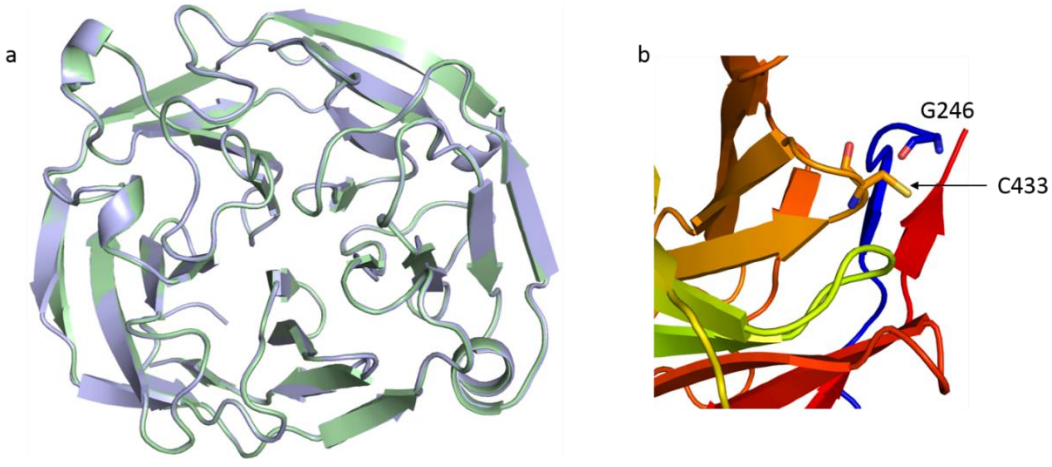

Figure A.2 Structure of reduced myoc-OLF. a. Overlay of reduced (green) and non-reduced (blue) structures. b. Zoom in to reduced disulfide bond.

REFERENCES

1. Alward, W. L. (1998) Medical management of glaucoma, *New England Journal of Medicine 339*, 1298-1307.

2. Casson, R. J., Chidlow, G., Wood, J. P. M., Crowston, J. G., and Goldberg, I. (2012) Definition of glaucoma: clinical and experimental concepts, *Clinical & Experimental Ophthalmology 40*, 341-349.

3. Quigley, H. A., and Broman, A. T. (2006) The number of people with glaucoma worldwide in 2010 and 2020, *The British Journal of Ophthalmology 90*, 262-267.

4. Vrabec, J. P., and Levin, L. A. (2007) The neurobiology of cell death in glaucoma, *Eye 21*, S11-S14.

5. Burgoyne, C. F., Crawford Downs, J., Bellezza, A. J., Francis Suh, J. K., and Hart, R. T. (2005) The optic nerve head as a biomechanical structure: a new paradigm for understanding the role of IOP-related stress and strain in the pathophysiology of glaucomatous optic nerve head damage, *Progress in Retinal and Eye Research 24*, 39-73.

6. Group, C. N.-T. G. S. (1998) Comparison of glaucomatous progression between untreated patients with normal-tension glaucoma and patients with therapeutically reduced intraocular pressures, *American Journal of Ophthalmology 126*, 487-497.

7. Investigators, A. (2000) The Advanced Glaucoma Intervention Study (AGIS): 7. The relationship between control of intraocular pressure and visual field deterioration, *American Journal of Ophthalmology 130*, 429-440.

8. Kwon, Y. H., Fingert, J. H., Kuehn, M. H., and Alward, W. L. (2009) Primary open-angle glaucoma, *New England Journal of Medicine 360*, 1113-1124.

9. Schlötzer-Schrehardt, U. (2011) Genetics and Genomics of Pseudoexfoliation Syndrome/Glaucoma, *Middle East African Journal of Ophthalmology 18*, 30-36.

10. Kersey, J. P., and Broadway, D. C. (2005) Corticosteroid-induced glaucoma: a review of the literature, *Eye 20*, 407-416.

11. Fan, B. J., Wang, D. Y., Lam, D. S. C., and Pang, C. P. (2006) Gene mapping for primary open angle glaucoma, *Clinical Biochemistry 39*, 249-258.

12. Allingham, R., Liu, Y., and Rhee, D. J. (2009) The genetics of primary open-angle glaucoma: a review, *Experimental Eye Research 88*, 837-844.

13. Vasiliou, V., and Gonzalez, F. J. (2008) Role of CYP1B1 in Glaucoma, *Annual Review of Pharmacology and Toxicology 48*, 333-358.

14. Aung, T., Rezaie, T., Okada, K., Viswanathan, A. C., Child, A. H., Brice, G., Bhattacharya, S. S., Lehmann, O. J., Sarfarazi, M., and Hitchings, R. A. (2005) Clinical features and course of patients with glaucoma with the E50K mutation in the optineurin gene, *Investigative Ophthalmology & Visual Science 46*, 2816-2822.

15. Rezaie, T., Child, A., Hitchings, R., Brice, G., Miller, L., Coca-Prados, M., Héon, E., Krupin, T., Ritch, R., and Kreutzer, D. (2002) Adult-onset primary open-angle glaucoma caused by mutations in optineurin, *Science 295*, 1077-1079.

16. Wolfs, R. C., Klaver, C. C., Ramrattan, R. S., van Duijn, C. M., Hofman, A., and de Jong, P. T. (1998) Genetic risk of primary open-angle glaucoma: population-based familial aggregation study, *Archives of Ophthalmology 116*, 1640-1645.

17. Thorleifsson, G., Walters, G. B., Hewitt, A. W., Masson, G., Helgason, A., DeWan, A., Sigurdsson, A., Jonasdottir, A., Gudjonsson, S. A., and Magnusson, K. P. (2010) Common variants near CAV1 and CAV2 are associated with primary open-angle glaucoma, *Nature Genetics 42*, 906-909.

18. Wiggs, J. L., Kang, J. H., Yaspan, B. L., Mirel, D. B., Laurie, C., Crenshaw, A., Brodeur, W., Gogarten, S., Olson, L. M., and Abdrabou, W. (2011) Common Variants Near CAV1 and CAV2 are Associated with Primary Open-Angle Glaucoma in Caucasians from the United States, *Human Molecular Genetics*, 20 (23) 4707-4713.

19. Bach-Holm, D., Kessing, S. V., Mogensen, U., Forman, J. L., Andersen, P. K., and Kessing, L. V. (2012) Normal tension glaucoma and Alzheimer disease: comorbidity, *Acta Ophthalmologica 90*, 683-685.

20. Wong, V. H. Y., Bui, B. V., and Vingrys, A. J. (2011) Clinical and experimental links between diabetes and glaucoma, *Clinical and Experimental Optometry 94*, 4-23.

21. Cheung, W., Guo, L., and Cordeiro, M. F. (2008) Neuroprotection in glaucoma: drug-based approaches, *Optometry and Vision Science 85*, 406-416.

22. Tsolaki, F., Gogaki, E., Tiganita, S., Skatharoudi, C., Lopatatzidi, C., Topouzis, F., and Tsolaki, M. (2011) Alzheimer's disease and primary open-angle glaucoma: is there a connection, *Clinical Ophthalmology (Auckland, NZ) 5*, 887-890.

23. Goel, M., Picciani, R. G., Lee, R. K., and Bhattacharya, S. K. (2010) Aqueous humor dynamics: a review, *The Open Ophthalmology Journal 4*, 52-59.

24. Alm, A., and Nilsson, S. F. E. (2009) Uveoscleral outflow – A review, *Experimental Eye Research 88*, 760-768.

25. Gabelt, B. A. T., and Kaufman, P. L. (2005) Changes in aqueous humor dynamics with age and glaucoma, *Progress in Retinal and Eye Research 24*, 612-637.

26. Toris, C. B., Yablonski, M. E., Wang, Y.-L., and Camras, C. B. (1999) Aqueous humor dynamics in the aging human eye, *American Journal of Ophthalmology 127*, 407-412.

27. van Koolwijk, L. M., Ramdas, W. D., Ikram, M. K., Jansonius, N. M., Pasutto, F., Hysi, P. G., Macgregor, S., Janssen, S. F., Hewitt, A. W., and Viswanathan, A. C. (2012) Common genetic determinants of intraocular pressure and primary open-angle glaucoma, *PLoS Genetics 8*, e1002611.

28. Crawford Downs, J., Roberts, M. D., and Sigal, I. A. (2011) Glaucomatous cupping of the lamina cribrosa: A review of the evidence for active progressive remodeling as a mechanism, *Experimental Eye Research 93*, 133-140.

29. Last, J. A., Pan, T., Ding, Y., Reilly, C. M., Keller, K., Acott, T. S., Fautsch, M. P., Murphy, C. J., and Russell, P. (2011) Elastic modulus determination of normal and glaucomatous human trabecular meshwork, *Investigative Ophthalmology & Visual Science 52*, 2147-2152.

30. Stamer, W. D., Braakman, S. T., Zhou, E. H., Ethier, C. R., Fredberg, J. J., Overby, D. R., and Johnson, M. (2015) Biomechanics of Schlemm's canal endothelium and intraocular pressure reduction, *Progress in Retinal and Eye Research*. 44, 86-98

31. Grossniklaus, H. E., Nickerson, J. M., Edelhauser, H. F., Bergman, L. A., and Berglin, L. (2013) Anatomic Alterations in Aging and Age-Related Diseases of the Eye, *Investigative Ophthalmology & Visual Science 54*, ORSF23-ORSF27.

32. Polansky, J., Fauss, D., Chen, P., Chen, H., Lütjen-Drecoll, E., Johnson, D., Kurtz, R., Ma, Z.-D., Bloom, E., and Nguyen, T. (1997) Cellular pharmacology and molecular biology of the trabecular meshwork inducible glucocorticoid response gene product, *Ophthalmologica 211*, 126-139.

33. Nguyen, T. D., Chen, P., Huang, W. D., Chen, H., Johnson, D., and Polansky, J. R. (1998) Gene Structure and Properties of TIGR, an Olfactomedin-related Glycoprotein Cloned from Glucocorticoid-induced Trabecular Meshwork Cells, *Journal of Biological Chemistry 273*, 6341-6350.

34. Shepard, A. R., Jacobson, N., Fingert, J. H., Stone, E. M., Sheffield, V. C., and Clark, A. F. (2001) Delayed Secondary Glucocorticoid Responsiveness of MYOC in Human Trabecular Meshwork Cells, *Investigative Ophthalmology & Visual Science 42*, 3173-3181.

35. Sheffield, V. C., Stone, E. M., Alward, W. L., Drack, A. V., Johnson, A. T., Streb, L. M., and Nichols, B. E. (1993) Genetic linkage of familial open angle glaucoma to chromosome 1q21-q31, *Nature Genetics 4*, 47-50.

36. Stone, E. M., Fingert, J. H., Alward, W. L., Nguyen, T. D., Polansky, J. R., Sunden, S. L., Nishimura, D., Clark, A. F., Nystuen, A., Nichols, B. E., Mackey, D. A., Ritch, R., Kalenak, J. W., Craven, E. R., and Sheffield, V. C. (1997)

Identification of a gene that causes primary open angle glaucoma, *Science 275*, 668-670.

37. Kubota, R., Noda, S., Wang, Y., Minoshima, S., Asakawa, S., Kudoh, J., Mashima, Y., Oguchi, Y., and Shimizu, N. (1997) A Novel Myosin-like Protein (Myocilin) Expressed in the Connecting Cilium of the Photoreceptor: Molecular Cloning, Tissue Expression, and Chromosomal Mapping, *Genomics 41*, 360-369.

38. Wordinger, R. J., and Clarka, A. F. (1999) Effects of glucocorticoids on the trabecular meshwork: towards a better understanding of glaucoma, *Progress in Retinal and Eye Research 18*, 629-667.

39. Clark, A. F., Steely, H. T., Dickerson, J. E., English-Wright, S., Stropki, K., McCartney, M. D., Jacobson, N., Shepard, A. R., Clark, J. I., and Matsushima, H. (2001) Glucocorticoid induction of the glaucoma gene MYOC in human and monkey trabecular meshwork cells and tissues, *Investigative Ophthalmology & Visual Science 42*, 1769-1780.

40. Fautsch, M. P., Bahler, C. K., Jewison, D. J., and Johnson, D. H. (2000) Recombinant TIGR/MYOC increases outflow resistance in the human anterior segment, *Investigative Ophthalmology & Visual Science 41*, 4163-4168.

41. Fautsch, M. P., Bahler, C. K., Vrabel, A. M., Howell, K. G., Loewen, N., Teo, W. L., Poeschla, E. M., and Johnson, D. H. (2006) Perfusion of his-tagged eukaryotic myocilin increases outflow resistance in human anterior segments in the presence of aqueous humor, *Investigative Ophthalmology & Visual Science 47*, 213-221.

42. Borrás, T., Rowlette, L. L. S., Tamm, E. R., Gottanka, J., and Epstein, D. L. (2002) Effects of elevated intraocular pressure on outflow facility and TIGR/MYOC expression in perfused human anterior segments, *Investigative Ophthalmology & Visual Science 43*, 33-40.

43. Tamm, E. R., Russell, P., Epstein, D. L., Johnson, D. H., and Piatigorsky, J. (1999) Modulation of myocilin/TIGR expression in human trabecular meshwork, *Investigative Ophthalmology & Visual Science 40*, 2577-2582.

44. Hewitt, A., Mackey, D., and Craig, J. (2008) Myocilin allele-specific glaucoma phenotype database, *Human Mutation* 29 (2) 207-211.

45. Resch, Z., and Fautsch, M. (2009) Glaucoma-associated myocilin: A better understanding but much more to learn, *Experimental Eye Research 88*, 704-712.

46. Fingert, J. H., Stone, E. M., Sheffield, V. C., and Alward, W. L. (2002) Myocilin glaucoma, *Survey of Ophthalmology 47*, 547-561.

47. Liu, Y., and Vollrath, D. (2004) Reversal of mutant myocilin non-secretion and cell killing: implications for glaucoma, *Human Molecular Genetics 13*, 1193-1204.

48. Burns, J. N., Turnage, K. C., Walker, C. A., and Lieberman, R. L. (2011) The stability of myocilin olfactomedin domain variants provides new insight into glaucoma as a protein misfolding disorder, *Biochemistry 50*, 5824-5833.

49. Orwig, S. D., Perry, C. W., Kim, L. Y., Turnage, K. C., Zhang, R., Vollrath, D., Schmidt-Krey, I., and Lieberman, R. L. (2012) Amyloid fibril formation by the glaucoma-associated olfactomedin domain of myocilin, *Journal of Molecular Biology 421*, 242-255.

50. Ueda, J., and Yue, B. Y. (2003) Distribution of myocilin and extracellular matrix components in the corneoscleral meshwork of human eyes, *Investigative Ophthalmology & Visual Science 44*, 4772-4779.

51. Ueda, J., Wentz-Hunter, K., and Yue, B. Y. (2002) Distribution of myocilin and extracellular matrix components in the juxtacanalicular tissue of human eyes, *Investigative Ophthalmology & Visual Science 43*, 1068-1076.

52. Sena, D. F., and Lindsley, K. (2013) Neuroprotection for treatment of glaucoma in adults, *Cochrane Database of Systemic Reviews 2* CD006539.

53. Vollrath, D., and Liu, Y. (2006) Temperature sensitive secretion of mutant myocilins, *Experimental Eye Research 82*, 1030-1036.

54. Gobeil, S., Letartre, L., and Raymond, V. (2006) Functional analysis of the glaucoma-causing TIGR/myocilin protein: integrity of amino-terminal coiled-coil regions and olfactomedin homology domain is essential for extracellular adhesion and secretion, *Experimental Eye Reserach 82*, 1017-1029.

55. Burns, J. N., Orwig, S. D., Harris, J. L., Watkins, J. D., Vollrath, D., and Lieberman, R. L. (2010) Rescue of glaucoma-causing mutant myocilin thermal stability by chemical chaperones, *ACS Chemical Biology 5*, 477-487.

56. Jia, L.-Y., Gong, B., Pang, C.-P., Huang, Y., Lam, D. S.-C., Wang, N., and Yam, G. H.-F. (2009) Correction of the disease phenotype of myocilin-causing glaucoma by a natural osmolyte, *Investigative Ophthalmology & Visual Science 50*, 3743-3749.

57. Yam, G. H.-F., Gaplovska-Kysela, K., Zuber, C., and Roth, J. (2007) Sodium 4-phenylbutyrate acts as a chemical chaperone on misfolded myocilin to rescue cells from endoplasmic reticulum stress and apoptosis, *Investigative Ophthalmology & Visual Science 48*, 1683-1690.

58. Orwig, S. D., Chi, P. V., Du, Y., Hill, S. E., Cavitt, M. A., Suntharalingam, A., Turnage, K. C., Dickey, C. A., France, S., Fu, H., and Lieberman, R. L. (2013) Ligands for Glaucoma-Associated Myocilin Discovered by a Generic Binding Assay, *ACS Chemical Biology 9*, 517-525.

59. Donegan, R. K., Hill, S. E., Freeman, D. M., Nguyen, E., Orwig, S. D., Turnage, K. C., and Lieberman, R. L. (2015) Structural basis for misfolding in myocilin-associated glaucoma, *Human Molecular Genetics*, 24 (8) 2111-2124.

60. Karali, A., Russell, P., Stefani, F. H., and Tamm, E. R. (2000) Localization of myocilin/trabecular meshwork--inducible glucocorticoid response protein in the human eye, *Investigative Ophthalmology & Visual Science 41*, 729-740.

61. Ohlmann, A., Goldwich, A., Flügel-Koch, C., Fuchs, A. V., Schwager, K., and Tamm, E. R. (2003) Secreted glycoprotein myocilin is a component of the myelin sheath in peripheral nerves, *Glia 43*, 128-140.

62. Sanchez-Sanchez, F., Martinez-Redondo, F., Aroca-Aguilar, J. D., Coca-Prados, M., and Escribano, J. (2007) Characterization of the intracellular proteolytic cleavage of myocilin and identification of calpain II as a myocilin-processing protease, *Journal of Biological Chemistry 282*, 27810-27824.

63. Wentz–Hunter, K., Ueda, J., and Yue, B. Y. J. T. (2002) Protein Interactions with Myocilin, *Investigative Ophthalmology & Visual Science 43*, 176-182.

64. Orwig, S. D., and Lieberman, R. L. (2011) Biophysical characterization of the olfactomedin domain of myocilin, an extracellular matrix protein implicated in inherited forms of glaucoma *PLoS ONE 6*, e16347.

65. Fingert, J. H., Heon, E., Liebmann, J. M., Yamamoto, T., Craig, J. E., Rait, J., Kawase, K., Hoh, S. T., Buys, Y. M., Dickinson, J., Hockey, R. R., Williams-Lyn, D., Trope, G., Kitazawa, Y., Ritch, R., Mackey, D. A., Alward, W. L., Sheffield, V. C., and Stone, E. M. (1999) Analysis of myocilin mutations in 1703 glaucoma patients from five different populations, *Human Molecular Genetics 8*, 899-905.

66. Filla, M. S., Liu, X., Nguyen, T. D., Polansky, J. R., Brandt, C. R., Kaufman, P. L., and Peters, D. M. (2002) In vitro localization of TIGR/MYOC in trabecular meshwork extracellular matrix and binding to fibronectin, *Investigative Ophthalmology & Visual Science. 43*, 151-161.

67. Peters, D. M., Herbert, K., Biddick, B., and Peterson, J. A. (2005) Myocilin binding to Hep II domain of fibronectin inhibits cell spreading and incorporation of paxillin into focal adhesions, *Experimental Cell Research 303*, 218-228.

68. Kwon, H.-S., Lee, H.-S., Ji, Y., Rubin, J. S., and Tomarev, S. I. (2009) Myocilin Is a Modulator of Wnt Signaling, *Molecular and Cellular Biology 29*, 2139-2154.

69. Joe, M. K., Kwon, H. S., Cojocaru, R., and Tomarev, S. I. (2014) Myocilin regulates cell proliferation and survival, *Journal of Biological Chemistry 289*, 10155-10167.

70. Sakai, H., Shen, X., Koga, T., Park, B.-C., Noskina, Y., Tibudan, M., and Yue, B. Y. J. T. (2007) Mitochondrial association of myocilin, product of a glaucoma gene, in human trabecular meshwork cells, *Journal of Cellular Physiology 213*, 775-784.

71. Mertts, M., Garfield, S., Tanemoto, K., and Tomarev, S. I. (1999) Identification of the region in the N-terminal domain responsible for the cytoplasmic localization of

Myoc/Tigr and its association with microtubules, *Laboratory Investigations 79*, 1237-1245.

72. Koch, M. A., Rosenhammer, B., Koschade, S. E., Braunger, B. M., Volz, C., Jägle, H., and Tamm, E. R. (2014) Myocilin modulates programmed cell death during retinal development, *Experimental Eye Research 125*, 41-52.

73. Joe, M. K., Sohn, S., Choi, Y. R., Park, H., and Kee, C. (2005) Identification of flotillin-1 as a protein interacting with myocilin: implications for the pathogenesis of primary open-angle glaucoma, *Biochemical and Biophysical Research Communications 336*, 1201-1206.

74. Torrado, M., Trivedi, R., Zinovieva, R., Karavanova, I., and Tomarev, S. I. (2002) Optimedin: a novel olfactomedin-related protein that interacts with myocilin, *Human Molecular Genetics 11*, 1291-1301.

75. Fautsch, M. P., Vrabel, A. M., and Johnson, D. H. (2006) The identification of myocilin-associated proteins in the human trabecular meshwork, *Experimental Eye Reserach 82*, 1046-1052.

76. Maurer, P., Hohenester, E., and Engel, J. (1996) Extracellular calcium-binding proteins, *Current Opinion in Cell Biology 8*, 609-617.

77. Cruciani, F., Moramarco, A., Antonelli, B., Mollo, R., Balacco-Gabrieli, C., Costantini, S., Ciaralli, L., Giordano, R., Sepe, A., Damore, E., and Valeri, M. (2004) Evaluation of five elements in lenses and aqueous humour of experimental rabbits after induced opacity, *Journal of Trace Elements in Medicine and Biology 18*, 141-147.

78. Ringvold, A., Sagen, E., Bjerve, K. S., and Folling, I. (1988) The calcium and magnesium content of the human lens and aqueous humour. A study in patients with hypocalcemic and senile cataract, *Acta Ophthalmologica (Copenh) 66*, 153-156.

79. Peters, D. M., Herbert, K., Biddick, B., and Peterson, J. A. (2005) Myocilin binding to Hep II domain of fibronectin inhibits cell spreading and incorporation of paxillin into focal adhesions, *Experimental Cell Research 303*, 218-228.

80. Zhou, Y., Grinchuk, O., and Tomarev, S. I. (2008) Transgenic mice expressing the Tyr437His mutant of human myocilin protein develop glaucoma, *Investigative Ophthalmology & Visual Science. 49*, 1932-1939.

81. Wang, L., Zhuo, Y., Liu, B., Huang, S., Hou, F., and Ge, J. (2007) Pro370Leu mutant myocilin disturbs the endoplasm reticulum stress response and mitochondrial membrane potential in human trabecular meshwork cells, *Molecular Vision 13*, 618-625.

82. Joe, M. K., Sohn, S., Hur, W., Moon, Y., Choi, Y. R., and Kee, C. (2003) Accumulation of mutant myocilins in ER leads to ER stress and potential

cytotoxicity in human trabecular meshwork cells, *Biochemical and Biophysical Research Communications 312*, 592-600.

83. Gobeil, S., Rodrigue, M.-A., Moisan, S., Nguyen, T. D., Polansky, J. R., Morissette, J., and Raymond, V. (2004) Intracellular sequestration of hetero-oligomers formed by wild-type and glaucoma-causing myocilin mutants, *Investigative Ophthalmology & Visual Science 45*, 3560-3567.

84. Kim, B. S., Savinova, O. V., Reedy, M. V., Martin, J., Lun, Y., Gan, L., Smith, R. S., Tomarev, S. I., John, S. W., and Johnson, R. L. (2001) Targeted disruption of the myocilin gene (myoc) suggests that human glaucoma-causing mutations are gain of function, *Molecular and Cellular Biology 21*, 7707-7713.

85. Lam, D. S., Leung, Y. F., Chua, J. K., Baum, L., Fan, D. S., Choy, K. W., and Pang, C. P. (2000) Truncations in the TIGR gene in individuals with and without primary open-angle glaucoma, *Investigative Ophthalmology & Visual Science. 41*, 1386-1391.

86. Herczenik, E., and Gebbink, M. (2008) Molecular and cellular aspects of protein misfolding and disease, *FASEB Journal 22*, 2115-2133.

87. Evenas, J., Malmendal, A., and Forsen, S. (1998) Calcium, *Current Opinion in Chemical Biology 2*, 293-302.

88. Maurer, P., and Hohenester, E. (1997) Structural and functional aspects of calcium binding in extracellular matrix proteins, *Matrix Biology 15*, 569-580.

89. Zhang, K., Zhang, L., and Weinreb, R. N. (2012) Ophthalmic drug discovery: novel targets and mechanisms for retinal diseases and glaucoma, *Nature Reviews Drug Discovery 11*, 541-559.

90. McLaughlin, C. W., Karl, M. O., Zellhuber-McMillan, S., Wang, Z., Do, C. W., Leung, C. T., Li, A., Stone, R. A., Macknight, A. D., and Civan, M. M. (2008) Electron probe X-ray microanalysis of intact pathway for human aqueous humor outflow, *American Journal of Physiology Cell Physiology 295*, C1083-1091.

91. Polansky, J. R., Fauss, D. J., Chen, P., Chen, H., Lutjen-Drecoll, E., Johnson, D., Kurtz, R. M., Ma, Z. D., Bloom, E., and Nguyen, T. D. (1997) Cellular pharmacology and molecular biology of the trabecular meshwork inducible glucocorticoid response gene product, *Ophthalmologica 211*, 126-139.

92. Carbone, M. A., Ayroles, J. F., Yamamoto, A., Morozova, T. V., West, S. A., Magwire, M. M., Mackay, T. F. C., and Anholt, R. R. H. (2009) Overexpression of myocilin in the Drosophila eye activates the unfolded protein response: implications for glaucoma, *PLoS ONE 4*, e4216.

93. Clark, A. F., and Wordinger, R. J. (2009) The role of steroids in outflow resistance, *Experimental Eye Research 88*, 752-759.

94. Orwig, S. D., Perry, C. W., Kim, L. Y., Turnage, K. C., Zhang, R., Vollrath, D., Schmidt-Krey, I., and Lieberman, R. L. (2012) Amyloid fibril formation by the glaucoma-associated olfactomedin domain of myocilin, *Journal of Molecular Biology 421*, 242-255.

95. Fautsch, M. P., and Johnson, D. H. (2001) Characterization of myocilin-myocilin interactions, *Investigative Ophthalmology & Visual Science 42*, 2324-2331.

96. Goldwich, A., Scholz, M., and Tamm, E. R. (2009) Myocilin promotes substrate adhesion, spreading and formation of focal contacts in podocytes and mesangial cells, *Histochemistry and Cell Biology 131*, 167-180.

97. Wentz-Hunter, K., Ueda, J., and Yue, B. Y. (2002) Protein interactions with myocilin, *Investigative Ophthalmology & Visual Science 43*, 176-182.

98. Tomarev, S. I., and Nakaya, N. (2009) Olfactomedin domain-containing proteins: possible mechanisms of action and functions in normal development and pathology, *Molecular Neurobiology 40*, 122-138.

99. Hillier, B. J., and Vacquier, V. D. (2007) Structural features and functional domains of amassin-1, a cell-binding olfactomedin protein, *Biochemistry and Cell Biology 85*, 552-562.

100. Labasque, M., Devaux, J. J., Leveque, C., and Faivre-Sarrailh, C. (2011) Fibronectin type III-like domains of neurofascin-186 protein mediate gliomedin binding and its clustering at the developing nodes of Ranvier, *Journal of Biological Chemistry 286*, 42426-42434.

101. Yu, L., Wang, L., and Chen, S. (2011) Olfactomedin 4, a novel marker for the differentiation and progression of gastrointestinal cancers, *Neoplasma 58*, 9-13.

102. Kobayashi, D., Koshida, S., Moriai, R., Tsuji, N., and Watanabe, N. (2007) Olfactomedin 4 promotes S-phase transition in proliferation of pancreatic cancer cells, *Cancer Science 98*, 334-340.

103. Liu, R. H., Yang, M. H., Xiang, H., Bao, L. M., Yang, H. A., Yue, L. W., Jiang, X., Ang, N., Wu, L. Y., and Huang, Y. (2012) Depletion of OLFM4 gene inhibits cell growth and increases sensitization to hydrogen peroxide and tumor necrosis factor-alpha induced-apoptosis in gastric cancer cells, *Journal of Biomedical Science 19*, 38.

104. Gersemann, M., Becker, S., Nuding, S., Antoni, L., Ott, G., Fritz, P., Oue, N., Yasui, W., Wehkamp, J., and Stange, E. F. (2012) Olfactomedin-4 is a glycoprotein secreted into mucus in active IBD, *Journal of Crohns and Colitis 6*, 425-434.

105. Niesen, F. H., Berglund, H., and Vedadi, M. (2007) The use of differential scanning fluorimetry to detect ligand interactions that promote protein stability, *Nature Protocols 2*, 2212-2221.

106. Sanchez-Ruiz, J. M. (2007) Ligand effects on protein thermodynamic stability, *Biophysical Chemistry 126*, 43-49.

107. Smith, P. D., Liesegang, G. W., Berger, R. L., Czerlinski, G., and Podolsky, R. J. (1984) A stopped-flow investigation of calcium ion binding by ethylene glycol bis(beta-aminoethyl ether)-N,N'-tetraacetic acid, *Analytical Biochemistry 143*, 188-195.

108. Bryant, D. T. (1985) Quin 2: the dissociation constants of its Ca2+ and Mg2+ complexes and its use in a fluorimetric method for determining the dissociation of Ca2+-protein complexes, *Biochemistry Journal 226*, 613-616.

109. Pidcock, E., and Moore, G. R. (2001) Structural characteristics of protein binding sites for calcium and lanthanide ions, *Journal of Biological Inorganic Chemistry 6*, 479-489.

110. Pei, J., and Grishin, N. V. (2007) PROMALS: towards accurate multiple sequence alignments of distantly related proteins, *Bioinformatics 23*, 802-808.

111. Brahms, S., and Brahms, J. (1980) Determination of protein secondary structure in solution by vacuum ultraviolet circular dichroism, *Journal of Molecular Biology 138*, 149-178.

112. Morrisett, J. D., and Broomfield, C. A. (1971) Active site spin-labeled alpha-chymotrypsin. Guanidine hydrochloride denaturation studies using electron paramagnetic resonance and circular dichroism, J*ournal of the American Chemical Society 93*, 7297-7304.

113. Sigrist, C. J., Cerutti, L., de Castro, E., Langendijk-Genevaux, P. S., Bulliard, V., Bairoch, A., and Hulo, N. (2010) PROSITE, a protein domain database for functional characterization and annotation, *Nucleic Acids Research 38*, D161-166.

114. Innis, C. A., Shi, J., and Blundell, T. L. (2000) Evolutionary trace analysis of TGF-beta and related growth factors: implications for site-directed mutagenesis, *Protein Engineering 13*, 839-847.

115. Dudev, T., and Lim, C. (2003) Principles governing Mg, Ca, and Zn binding and selectivity in proteins, *Chemical Reviews 103*, 773-788.

116. Maurer, P., Hohenadl, C., Hohenester, E., Gohring, W., Timpl, R., and Engel, J. (1995) The C-terminal portion of BM-40 (SPARC/osteonectin) is an autonomously folding and crystallisable domain that binds calcium and collagen IV, *Journal of Molecular Biology 253*, 347-357.

117. Meldolesi, J., and Pozzan, T. (1998) The endoplasmic reticulum Ca2+ store: a view from the lumen, *Trends in Biochemical Sciences 23*, 10-14.

118. Hillier, B. J., and Vacquier, V. D. (2003) Amassin, an olfactomedin protein, mediates the massive intercellular adhesion of sea urchin coelomocytes, *Journal of Cell Biology 160*, 597-604.

119. Clark, A. F. (2012) The cell and molecular biology of glaucoma: biomechanical factors in glaucoma, *Investigative Ophthalmology & Visual Science 53*, 2473-2475.

120. Tumminia, S. J., Mitton, K. P., Arora, J., Zelenka, P., Epstein, D. L., and Russell, P. (1998) Mechanical stretch alters the actin cytoskeletal network and signal transduction in human trabecular meshwork cells, *Investigative Ophthalmology & Visual Science 39*, 1361-1371.

121. Borras, T., and Comes, N. (2009) Evidence for a calcification process in the trabecular meshwork, *Experimental Eye Research 88*, 738-746.

122. Kennedy, K. D., AnithaChristy, S. A., Buie, L. K., and Borras, T. (2012) Cystatin a, a potential common link for mutant myocilin causative glaucoma, *PLoS One 7*, e36301.

123. Orwig, S. D., Chi, P. V., Du, Y., Hill, S.E., Cavitt, M.A., Suntharalingam, A. Turnage, K.C., Dickey, C.A., France, S. Fu, H., and Lieberman, R. L. (2014) Ligands for glaucoma-associated myocilin discovered by a generic binding assay. *ACS Chemical Biology 9(2) 517-525.*

124. Suntharalingam, A., Abisambra, J. F., O'Leary, J. C., Koren, J., Zhang, B., Joe, M. K., Blair, L. J., Hill, S. E., Jinwal, U. K., and Cockman, M. (2012) Glucose-regulated protein 94 triage of mutant myocilin through endoplasmic reticulum-associated degradation subverts a more efficient autophagic clearance mechanism, *Journal of Biological Chemistry 287*, 40661-40669.

125. Hill, S. E., Donegan, R. K., and Lieberman, R. L. (2014) The glaucoma-associated olfactomedin domain of myocilin forms polymorphic fibrils that are constrained by partial unfolding and peptide sequence, *Journal of Molecular Biology 426*, 921-935.

126. Oliveberg, M. (2010) Waltz, an exciting new move in amyloid prediction, *Nature Methods 7*, 187-188.

127. Trovato, A., Seno, F., and Tosatto, S. C. (2007) The PASTA server for protein aggregation prediction, *Protein Engineering Design and Selection 20*, 521-523.

128. Tsolis, A. C., Papandreou, N. C., Iconomidou, V. A., and Hamodrakas, S. J. (2013) A consensus method for the prediction of ‘aggregation-prone’peptides in globular proteins, *PloS One 8*, e54175.

129. Ahmed, A. B., and Kajava, A. V. (2013) Breaking the amyloidogenicity code: Methods to predict amyloids from amino acid sequence, *FEBS Letters 587*, 1089-1095.

130. Snyder, D. A., Rivers, A. M., Yokoe, H., Menco, B. P., and Anholt, R. R. (1991) Olfactomedin: purification, characterization, and localization of a novel olfactory glycoprotein, *Biochemistry 30*, 9143-9153.

131. Yokoe, H., and Anholt, R. R. (1993) Molecular cloning of olfactomedin, an extracellular matrix protein specific to olfactory neuroepithelium, *Proceedings of the National Acadamies of Science U S A 90*, 4655-4659.

132. Zeng, L.-C., Han, Z.-G., and Ma, W.-J. (2005) Elucidation of subfamily segregation and intramolecular coevolution of the olfactomedin-like proteins by comprehensive phylogenetic analysis and gene expression pattern assessment, *FEBS Letters 579*, 5443-5453.

133. Ando, K., Nagano, T., Nakamura, A., Konno, D., Yagi, H., and Sato, M. (2005) Expression and characterization of disulfide bond use of oligomerized A2-Pancortins: extracellular matrix constituents in the developing brain, *Neuroscience 133*, 947-957.

134. Furutani, Y., Manabe, R., Tsutsui, K., Yamada, T., Sugimoto, N., Fukuda, S., Kawai, J., Sugiura, N., Kimata, K., Hayashizaki, Y., and Sekiguchi, K. (2005) Identification and characterization of photomedins: novel olfactomedin-domain-containing proteins with chondroitin sulphate-E-binding activity, *Biochemistry Journal 389*, 675-684.

135. Zeng, L.-C., Liu, F., Zhang, X., Zhu, Z.-D., Wang, Z.-Q., Han, Z.-G., and Ma, W.-J. (2004) hOLF44, a secreted glycoprotein with distinct expression pattern, belongs to an uncharacterized olfactomedin-like subfamily newly identified by phylogenetic analysis, *FEBS Letters 571*, 74-80.

136. Gersemann, M., Becker, S., Nuding, S., Antoni, L., Ott, G., Fritz, P., Oue, N., Yasui, W., Wehkamp, J., and Stange, E. F. (2012) Olfactomedin-4 is a glycoprotein secreted into mucus in active IBD, *Journal of Crohn's and Colitis 6*, 425-434.

137. Liu, W., Yan, M., Liu, Y., McLeish, K. R., Coleman, W. G., and Rodgers, G. P. (2012) Olfactomedin 4 inhibits cathepsin C-mediated protease activities, thereby modulating neutrophil killing of Staphylococcus aureus and Escherichia coli in mice, *The Journal of Immunology 189*, 2460-2467.

138. Arcos-Burgos, M., Jain, M., Acosta, M., Shively, S., Stanescu, H., Wallis, D., Domene, S., Velez, J., Karkera, J., and Balog, J. (2010) A common variant of the latrophilin 3 gene, LPHN3, confers susceptibility to ADHD and predicts effectiveness of stimulant medication, *Molecular Psychiatry 15*, 1053-1066.

139. Consortium, E. G. G. (2012) A genome-wide association meta-analysis identifies new childhood obesity loci, *Nature Genetics 44*, 526-531.

140. Quigley, H. A. (1996) Number of people with glaucoma worldwide, *British Journal of Ophthalmology 80*, 389-393.

141. Chen, C. K.-M., Chan, N.-L., and Wang, A. H.-J. (2011) The many blades of the β-propeller proteins: conserved but versatile, *Trends in Biochemical Sciences 36*, 553-561.

142. Jawad, Z., and Paoli, M. (2002) Novel sequences propel familiar folds, *Structure 10*, 447-454.

143. Paoli, M., Anderson, B. F., Baker, H. M., Morgan, W. T., Smith, A., and Baker, E. N. (1999) Crystal structure of hemopexin reveals a novel high-affinity heme site formed between two β-propeller domains, *Nature Structural & Molecular Biology 6*, 926-931.

144. DeLano, W. L. (2002) Unraveling hot spots in binding interfaces: progress and challenges, *Current Opinion in Structural Biology 12*, 14-20.

145. Donegan, R. K., Hill, S. E., Turnage, K. C., Orwig, S. D., and Lieberman, R. L. (2012) The glaucoma-associated olfactomedin domain of myocilin is a novel calcium binding protein, *Journal of Biological Chemistry 287*, 43370-43377.

146. Pidcock, E., and Moore, G. R. (2001) Structural characteristics of protein binding sites for calcium and lanthanide ions, *Journal of Biological Inorganic Chemistry 6*, 479-489.

147. Harding, M. M. (2006) Small revisions to predicted distances around metal sites in proteins, *Acta Crystallographica Section D: Biological Crystallography 62*, 678-682.

148. Dai, J., Liu, J., Deng, Y., Smith, T. M., and Lu, M. (2004) Structure and protein design of a human platelet function inhibitor, *Cell 116*, 649-659.

149. Beisel, H. G., Kawabata, S. i., Iwanaga, S., Huber, R., and Bode, W. (1999) Tachylectin-2: crystal structure of a specific GlcNAc/GalNAc-binding lectin involved in the innate immunity host defense of the Japanese horseshoe crab Tachypleus tridentatus, *The EMBO Journal 18*, 2313-2322.

150. Nurizzo, D., Turkenburg, J. P., Charnock, S. J., Roberts, S. M., Dodson, E. J., McKie, V. A., Taylor, E. J., Gilbert, H. J., and Davies, G. J. (2002) Cellvibrio japonicus α-L-arabinanase 43A has a novel five-blade β-propeller fold, *Nature Structural & Molecular Biology 9*, 665-668.

151. Huang, W.-L., Wang, Y.-R., Ko, T.-P., Chia, C.-Y., Huang, K.-F., and Wang, A. H.-J. (2010) Crystal structure and functional analysis of the glutaminyl cyclase from Xanthomonas campestris, *Journal of Molecular Biology 401*, 374-388.

152. Wilkins, A., Erdin, S., Lua, R., and Lichtarge, O. (2012) Evolutionary trace for prediction and redesign of protein functional sites, In *Computational Drug Discovery and Design*, pp 29-42, Springer.

153. Ma, J. C., and Dougherty, D. A. (1997) The Cation−π Interaction, *Chemical Reviews 97*, 1303-1324.

154. Lua, R. C., and Lichtarge, O. (2010) PyETV: a PyMOL evolutionary trace viewer to analyze functional site predictions in protein complexes, *Bioinformatics 26*, 2981-2982.

155. Stelzl, U., Worm, U., Lalowski, M., Haenig, C., Brembeck, F. H., Goehler, H., Stroedicke, M., Zenkner, M., Schoenherr, A., and Koeppen, S. (2005) A human protein-protein interaction network: a resource for annotating the proteome, *Cell 122*, 957-968.

156. Giot, L., Bader, J. S., Brouwer, C., Chaudhuri, A., Kuang, B., Li, Y., Hao, Y., Ooi, C., Godwin, B., and Vitols, E. (2003) A protein interaction map of Drosophila melanogaster, *Science 302*, 1727-1736.

157. Dyer, M., Neff, C., Dufford, M., Rivera, C., Shattuck, D., and Laurent Rénia, B.-A. (2010) The Human-Bacterial Pathogen Protein Interaction Networks of Bacillus anthracis, Francisella tularensis and Yersinis Pestis. *PLoS One* 5 (8) e12089.

158. Camargo, L., Collura, V., Rain, J., Mizuguchi, K., Hermjakob, H., Kerrien, S., Bonnert, T., Whiting, P., and Brandon, N. (2007) Disrupted in Schizophrenia 1 Interactome: evidence for the close connectivity of risk genes and a potential synaptic basis for schizophrenia, *Molecular Psychiatry 12*, 74-86.

159. Adams, D. R., Ron, D., and Kiely, P. A. (2011) RACK1, A multifaceted scaffolding protein: Structure and function, *Cell Commuication and Signalling 9* (22).

160. Pons, T., Gmez, R., Chinea, G., and Valencia, A. (2003) Beta-propellers: associated functions and their role in human diseases, *Current medicinal chemistry 10*, 505-524.

161. Maurer, P., and Hohenester, E. (1997) Structural and functional aspects of calcium binding in extracellular matrix proteins, *Matrix Biology 15*, 569-580

162. Dodson, G., and Wlodawer, A. (1998) Catalytic triads and their relatives, *Trends in Biochemical Sciences 23*, 347-352.

163. Kabsch, W. (2010) Xds, *Acta Crystallographica Section D: Biological Crystallography 66*, 125-132.

164. Terwilliger, T. C., Adams, P. D., Read, R. J., McCoy, A. J., Moriarty, N. W., Grosse-Kunstleve, R. W., Afonine, P. V., Zwart, P. H., and Hung, L.-W. (2009) Decision-making in structure solution using Bayesian estimates of map quality: the PHENIX AutoSol wizard, *Acta Crystallographica Section D: Biological Crystallography 65*, 582-601.

165. McCoy, A. J., Grosse-Kunstleve, R. W., Adams, P. D., Winn, M. D., Storoni, L. C., and Read, R. J. (2007) Phaser crystallographic software, *Journal of Applied Crystallography 40*, 658-674.

166. Emsley, P., Lohkamp, B., Scott, W. G., and Cowtan, K. (2010) Features and development of Coot, *Acta Crystallographica Section D: Biological Crystallography 66*, 486-501.

167. Kleywegt, G. J. (2007) Crystallographic refinement of ligand complexes, *Acta Crystallographica Section D: Biological Crystallography 63*, 94-100.

168. Adams, P. D., Afonine, P. V., Bunkóczi, G., Chen, V. B., Davis, I. W., Echols, N., Headd, J. J., Hung, L.-W., Kapral, G. J., and Grosse-Kunstleve, R. W. (2010) PHENIX: a comprehensive Python-based system for macromolecular structure solution, *Acta Crystallographica Section D: Biological Crystallography 66*, 213-221.

169. Holm, L., and Rosenström, P. (2010) Dali server: conservation mapping in 3D, *Nucleic Acids Research 38*, W545-W549.

170. Krissinel, E., and Henrick, K. (2007) Inference of macromolecular assemblies from crystalline state, *Journal of Molecular Biology 372*, 774-797.

171. Brylinski, M., and Skolnick, J. (2011) FINDSITE-metal: Integrating evolutionary information and machine learning for structure-based metal-binding site prediction at the proteome level, *Proteins: Structure, Function, and Bioinformatics 79*, 735-751.

172. Valasatava, Y., Rosato, A., Cavallaro, G., and Andreini, C. (2014) MetalS3, a database-mining tool for the identification of structurally similar metal sites, *Journal of Biological Inorganic Chemistry 19*, 937-945.

173. Krissinel, E., and Henrick, K. (2004) Secondary-structure matching (SSM), a new tool for fast protein structure alignment in three dimensions, *Acta Crystallographica Section D: Biological Crystallography 60*, 2256-2268.

174. Pei, J., Kim, B.-H., and Grishin, N. V. (2008) PROMALS3D: a tool for multiple protein sequence and structure alignments, *Nucleic Acids Research 36*, 2295-2300.

175. Gouet, P., Robert, X., and Courcelle, E. (2003) ESPript/ENDscript: extracting and rendering sequence and 3D information from atomic structures of proteins, *Nucleic Acids Research 31*, 3320-3323.

176. Dolinsky, T. J., Czodrowski, P., Li, H., Nielsen, J. E., Jensen, J. H., Klebe, G., and Baker, N. A. (2007) PDB2PQR: expanding and upgrading automated preparation of biomolecular structures for molecular simulations, *Nucleic Acids Research 35*, W522-W525.

177. Baker, N. A., Sept, D., Joseph, S., Holst, M. J., and McCammon, J. A. (2001) Electrostatics of nanosystems: application to microtubules and the ribosome, *Proceedings of the National Academy of Sciences 98*, 10037-10041.

178. Zode, G. S., Kuehn, M. H., Nishimura, D. Y., Searby, C. C., Mohan, K., Grozdanic, S. D., Bugge, K., Anderson, M. G., Clark, A. F., Stone, E. M., and Sheffield, V. C. (2011) Reduction of ER stress via a chemical chaperone prevents disease phenotypes in a mouse model of primary open angle glaucoma, *Journal of Clinical Investigation 121*, 3542-3553.

179. Avisar, I., Lusky, M., Robinson, A., Shohat, M., Dubois, S., Raymond, V., and Gaton, D. D. (2009) The novel Y371D myocilin mutation causes an aggressive form of juvenile open-angle glaucoma in a Caucasian family from the Middle-East, *Molecular Vision 15*, 1945-1950.

180. Gong, G., Kosoko-Lasaki, O., Haynatzki, G. R., and Wilson, M. R. (2004) Genetic dissection of myocilin glaucoma, *Human Molecular Genetics 13*, R91-102.

181. Faucher, M., Anctil, J. L., Rodrigue, M. A., Duchesne, A., Bergeron, D., Blondeau, P., Cote, G., Dubois, S., Bergeron, J., Arseneault, R., Morissette, J., and Raymond, V. (2002) Founder TIGR/myocilin mutations for glaucoma in the Quebec population, *Human Molecular Genetics 11*, 2077-2090.

182. Alward, W. L., Fingert, J. H., Coote, M. A., Johnson, A. T., Lerner, S. F., Junqua, D., Durcan, F. J., McCartney, P. J., Mackey, D. A., Sheffield, V. C., and Stone, E. M. (1998) Clinical features associated with mutations in the chromosome 1 open-angle glaucoma gene (GLC1A), *New England Journal of Medicine 338*, 1022-1027.

183. Vincent, A. L., Billingsley, G., Buys, Y., Levin, A. V., Priston, M., Trope, G., Williams-Lyn, D., and Héon, E. (2002) Digenic inheritance of early-onset glaucoma: CYP1B1, a potential modifier gene, *The American Journal of Human Genetics 70*, 448-460.

184. Weisschuh, N., Neumann, D., Wolf, C., Wissinger, B., and Gramer, E. (2005) Prevalence of myocilin and optineurin sequence variants in German normal tension glaucoma patients, *Molecular Vision 11*, 284-287.

185. McKay, B. S., Congrove, N. R., Johnson, A. A., Dismuke, W. M., Bowen, T. J., and Stamer, W. D. (2013) A Role for Myocilin in Receptor-Mediated Endocytosis, *PloS One 8*, e82301.

186. Joe, M. K., and Tomarev, S. I. (2010) Expression of myocilin mutants sensitizes cells to oxidative stress-induced apoptosis: implication for glaucoma pathogenesis, *The American Journal of Pathology 176*, 2880-2890.

187. Liu, W., Liu, Y., Challa, P., Herndon, L. W., Wiggs, J. L., Girkin, C. A., Allingham, R. R., and Hauser, M. A. (2012) Low prevalence of myocilin mutations in an African American population with primary open-angle glaucoma, *Molecular Vision 18*, 2241-2246.

188. Shimizu, S., Lichter, P. R., Johnson, A. T., Zhou, Z., Higashi, M., Gottfredsdottir, M., Othman, M., Moroi, S. E., Rozsa, F. W., Schertzer, R. M., Clarke, M. S., Schwartz, A. L., Downs, C. A., Vollrath, D., and Richards, J. E. (2000) Age-

dependent prevalence of mutations at the GLC1A locus in primary open-angle glaucoma, *American Journal of Ophthalmology 130*, 165-177.

189. Pang, C. P., Leung, Y. F., Fan, B., Baum, L., Tong, W. C., Lee, W. S., Chua, J. K., Fan, D. S., Liu, Y., and Lam, D. S. (2002) TIGR/MYOC gene sequence alterations in individuals with and without primary open-angle glaucoma, *Investigative Ophthalmology & Visual Science 43*, 3231-3235.

190. Yoon, S., Kim, H.-S., Moon, J.-I., Lim, J. M., and Joo, C.-K. (1999) Mutations of the TIGR/MYOC gene in primary open-angle glaucoma in Korea, *American Journal of Human Genetics 64*, 1775-1778.

191. Zhang, K., Zhang, L., and Weinreb, R. N. (2012) Ophthalmic drug discovery: novel targets and mechanisms for retinal diseases and glaucoma, *Nature Reviews Drug Discovery 11*, 541-559.

192. Domené, S., Stanescu, H., Wallis, D., Tinloy, B., Pineda, D. E., Kleta, R., Arcos-Burgos, M., Roessler, E., and Muenke, M. (2011) Screening of human LPHN3 for variants with a potential impact on ADHD susceptibility, *American Journal of Medical Genetics Part B: Neuropsychiatric Genetics 156*, 11-18.

193. Fülöp, V., and Jones, D. T. (1999) β Propellers: structural rigidity and functional diversity, *Current Opinion in Structural Biology 9*, 715-721.

194. Maertens, B., Hopkins, D., Franzke, C.-W., Keene, D. R., Bruckner-Tuderman, L., Greenspan, D. S., and Koch, M. (2007) Cleavage and oligomerization of gliomedin, a transmembrane collagen required for node of ranvier formation, *Journal of Biological Chemistry 282*, 10647-10659.

195. Brenke, R., Kozakov, D., Chuang, G. Y., Beglov, D., Hall, D., Landon, M. R., Mattos, C., and Vajda, S. (2009) Fragment-based identification of druggable 'hot spots' of proteins using Fourier domain correlation techniques, *Bioinformatics 25*, 621-627.

196. Gao, M., and Skolnick, J. (2013) APoc: Large scale identification of similar protein pockets, *Bioinformatics*, 29 (5) 597-604.

197. Wang, S. Y., Hasty, C. E., Watson, P. A., Wicksted, J. P., Stith, R. D., and March, W. F. (1993) Analysis of metabolites in aqueous solutions by using laser Raman spectroscopy, *Applied Optics 32*, 925-929.

198. Genc, S., Kurnaz, I. A., and Ozilgen, M. (2011) Astrocyte-neuron lactate shuttle may boost more ATP supply to the neuron under hypoxic conditions-in silico study supported by in vitro expression data, *BMC Systems Biology 5*, 162.

199. Tarczyluk, M. A., Nagel, D. A., D O'Neil, J., Parri, H. R., Erin, H., Coleman, M. D., and Hill, E. J. (2013) Functional astrocyte–neuron lactate shuttle in a human stem cell-derived neuronal network, *Journal of Cerebral Blood Flow & Metabolism 33*, 1386-1393.

200. Chan, D., Lamande, S. R., Cole, W., and Bateman, J. F. (1990) Regulation of procollagen synthesis and processing during ascorbate-induced extracellular matrix accumulation in vitro, *Biochemistry Journal 269*, 175-181.

201. Davidson, J. M., LuValle, P. A., Zoia, O., Quaglino, D., and Giro, M. (1997) Ascorbate Differentially Regulates Elastin and Collagen Biosynthesis in Vascular Smooth Muscle Cells and Skin Fibroblasts by Pretranslational Mechanisms, *Journal of Biological Chemistry 272*, 345-352.

202. Philips, N., Keller, T., and Holmes, C. (2007) Reciprocal effects of ascorbate on cancer cell growth and the expression of matrix metalloproteinases and transforming growth factor-β, *Cancer Letters 256*, 49-55.

203. DeLano, W. L. (2002) Unraveling hot spots in binding interfaces: progress and challenges, *Current Opinion in Structural Biology 12*, 14-20.

204. Landon, M. R., Lieberman, R. L., Hoang, Q. Q., Ju, S., Caaveiro, J. M., Orwig, S. D., Kozakov, D., Brenke, R., Chuang, G. Y., Beglov, D., Vajda, S., Petsko, G. A., and Ringe, D. (2009) Detection of ligand binding hot spots on protein surfaces via fragment-based methods: application to DJ-1 and glucocerebrosidase, *Journal of Computer Aided Moleculatr Des*ign 23.8, 491-500.

205. Brenke, R., Kozakov, D., Chuang, G.-Y., Beglov, D., Hall, D., Landon, M. R., Mattos, C., and Vajda, S. (2009) Fragment-based identification of druggable 'hot spots' of proteins using Fourier domain correlation techniques, *Bioinformatics 25*, 621-627.

206. Ho Ngan, C., Bohnuud, T., Mottarella, S. E., Beglov, D., Villar, E. A., Hall, D. R., Kozakov, D., and Vajda, S. (2012) FTMAP: extended protein mapping with user-selected probe molecules, *Nucleic Acids Research*. 40 (W1): W271-W275

207. Pelletier, C. C., Lambert, J. L., and Borchert, M. (2005) Determination of glucose in human aqueous humor using Raman spectroscopy and designed-solution calibration, *Applied Spectroscopy 59*, 1024-1031.

208. Arakawa, T., and Timasheff, S. (1985) The stabilization of proteins by osmolytes, *Biophysical Journal 47*, 411-414.

209. Trott, O., and Olson, A. J. (2010) AutoDock Vina: improving the speed and accuracy of docking with a new scoring function, efficient optimization, and multithreading, *Journal of Computational Chemistry 31*, 455-461.

210. Genc, S., Kurnaz, I. A., and Ozilgen, M. (2011) Astrocyte-neuron lactate shuttle may boost more ATP supply to the neuron under hypoxic conditions--in silico study supported by in vitro expression data, *BMC systems biology 5*, 162.

211. Tarczyluk, M. A., Nagel, D. A., O'Neil, J. D., Parri, H. R., Tse, E. H., Coleman, M. D., and Hill, E. J. (2013) Functional astrocyte-neuron lactate shuttle in a human stem cell-derived neuronal network, *Journal of Cerebral Blood Flow and Metabolism 33*, 1386-1393.

212. Wang, S. Y., Hasty, C. E., Watson, P. A., Wicksted, J. P., Stith, R. D., and March, W. F. (1993) Analysis of metabolites in aqueous solutions by using laser Raman spectroscopy, *Applied Optics 32*, 925-929.

213. Dreyer, E. B., Zurakowski, D., Schumer, R. A., Podos, S. M., and Lipton, S. A. (1996) Elevated glutamate levels in the vitreous body of humans and monkeys with glaucoma, *Archives of Ophthalmology 114*, 299-305.

214. Dallakyan, S., and Olson, A. J. (2015) Small-Molecule Library Screening by Docking with PyRx, *Chemical Biology: Methods and Protocols*, 243-250.

215. Lusty, C. J. (1999) A gentle vapor-diffusion technique for cross-linking of protein crystals for cryocrystallography, *Journal of Applied Crystallography 32*, 106-112.

216. Otwinowski, Z., and Minor, W. (1997) Processing of diffraction data collected in oscillation mode, *Methods in Enzymology 276*, 307-326.

217. Brittain, H. G., Richardson, F. S., and Martin, R. B. (1976) Terbium (III) emission as a probe of calcium (II) binding sites in proteins, *Journal of the American Chemical Society 98*, 8255-8260.

218. Ross, J. A., Contino, P. B., Lulka, M. F., and Petra, P. H. (1985) Observation and quantitation of metal-binding sites in the sex steroid-binding protein of human and rabbit sera using the luminescent probe terbium, *Journal of Protein Chemistry 4*, 299-304.